Study on Lithiation and Delithiation Processes of Amorphous Silicon-Based Thin-Film Anodes for All-Solid-State Lithium-Ion Batteries

（全固体リチウムイオン電池に向けた

非晶質 Si 系薄膜負極の Li 挿入・脱離過程に関する研究）

Raimu Endo

Graduate School of Chemical Sciences and Engineering

Hokkaido University

2021

Contents

Contents

Contents

Contents

Chapter 1. Introduction

1.1 General Introduction

Lithium-ion batteries (LIBs)[1-6] are among the most indispensable devices for powering modern life and society. The commercialization of movable and rechargeable LIBs by the SONY Corporation in 1991 has drastically promoted the widespread application of portable devices such as mobile phones and laptop computers and has led to major advances in IT. In October 2019, the Nobel Prize in Chemistry[7] was awarded to Drs. Whittingham, Goodenough, and Yoshino for the development of LIBs.[1, 8-12] However, further improvement of LIB energy density and durability are strongly desirable toward achieving Society 5.0,[13] wherein electric vehicles (EVs) are daily driven, the utilization of renewable energy sources is expanded, and numerous sensors are connected to the internet and interact with each other, leading to a safe, comfortable society. LIBs are required for various functions and applications including safe, high-energy- and -power-density EVs; low-cost higher-capacity energy leveling and storage for renewable-energy sources; and small, lightweight LIBs for sensors and actuators.

Carbon materials including various graphites are the most commonly used for LIB anodes because of their very negative redox potential (0.1 V *vs*. Li^+/Li) and stable cycle performance owing to Li intercalation.[14] The theoretical capacity of a graphite anode is estimated to be approximately 372 mAh g^{-1} according to the following equation:[14-16]

$$6C + xLi^+ + xe^- \rightarrow Li_xC_6 \qquad \sim 0.1\ V\ vs.\ Li^+/Li. \qquad (1\text{ - }1)$$

Therefore, the development of cathode and anode materials should improve LIB energy density.[17-18] Representative anode material candidates are the Group IV elements including Si, which can store up to 4.4 atoms of Li per Si atom by the following

reaction:[19-21]

$$Si + 4.4Li^+ + 4.4e^- \rightarrow Li_{4.4}Si \qquad 0.35\ V\ vs.\ Li^+/Li. \quad (1-2)$$

The theoretical capacity densities of Si in $Li_{4.4}Si$, (4200 mAh g^{-1}), carbon, and Group IV materials are shown in Figure 1 - 1.

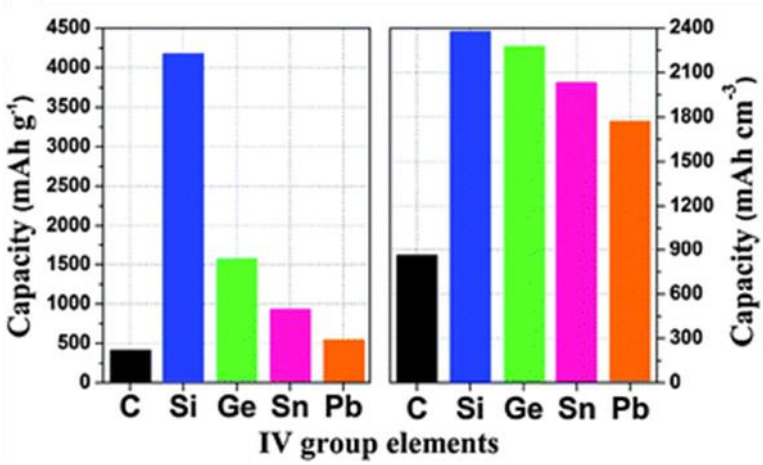

Figure 1 - 1. Gravimetric and volumetric capacities of C (LiC_6), Si ($Li_{4.4}Si$), Ge ($Li_{4.25}Ge$), Sn ($Li_{4.25}Sn$), and Pb ($Li_{4.25}Pb$). Reprinted from Reference[19] with permission from the Royal Society of Chemistry.

Although the reaction potential of Si anodes is slightly more positive than that of graphite ones, it is still sufficiently negative (0.35 V *vs*. Li^+/Li). In addition, Si is the second most abundant element after oxygen in Earth's crust. Because of the high theoretical capacity of Si, a tremendous amount of research has been conducted toward the practical application of Si anodes to LIBs.[22-23] However, the widespread application of Si LIB anodes is severely hampered by various lithiation/delithiation-associated phenomena.

Therefore, in the present study, lithiation/delithiation reactions of Si were investigated by analyzing the chemical state and structural evolution of Si anodes with a special focus on thin-film all-solid-state LIBs.

1.2 Si anodes for application to LIBs

1.2.1 Si–Li alloying

Reaction overview

Although Li–Si-phase-diagram-based thermodynamic calculations suggest the possible formation of crystalline $Li_{12}Si_7$, Li_7Si_3, $Li_{13}Si_4$, and $Li_{22}Si_5$;[24] some studies have suggested that these crystalline phases are not formed in the electrochemical reactions of Si with Li at approximately room temperature and that highly lithiated amorphous phases are formed instead, as evidenced by x-ray diffraction (XRD) and electron microscopy (EM) measurements.[25-26]

Figure 1 - 2 (a) shows the first lithiation/delithiation potential profiles plotted as a function of the gravimetric capacity density for a Si electrode.[27] The *y*-axis represents the cell potential, i.e., the Si electrode potential measured against a metallic Li counter electrode. When a bias voltage is applied to the Si to obtain a constant current, lithiation proceeds from A to C forming lithium silicide (Li_xSi), as shown in Figure 1 - 2 (a). When the potential reaches a certain cutoff voltage (C), lithiation is terminated, and the opposite positive voltage is applied for the subsequent delithiation (C to D). The cycle performance is evaluated by repeating these processes and then plotting the specific capacities as a function of the number of cycles. Clearly, the cycle performance shows rapid capacity fading, as shown Figure 1 - 2 (b), is the major bottleneck for the practical application of Si electrodes.

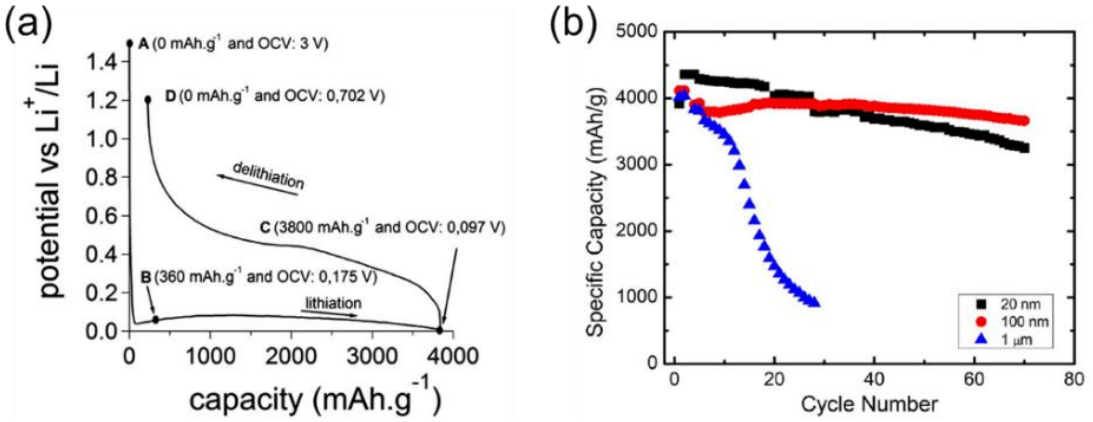

Figure 1 - 2. (a) Galvanostatic potential profiles obtained for the first lithiation/delithiation of Si electrode *vs.* metallic Li. (The electrolyte is a solution of 1 M $LiPF_6$ in ethylene carbonate (EC)-diethyl carbonate (DEC; 1:1 by weight).) Capacity and open circuit voltage (OCV) are indicated at each electrochemical state A-D. Reprinted from Reference[27] with permission from the Royal Society of Chemistry. (b) Cycle performance of cells comprising Si thin films prepared with various thicknesses. (The electrolyte is a solution of 1.2 M $LiPF_6$ in EC-ethyl methyl carbonate (EMC; 3:7 by weight) mixed with 10 wt.% fluoroethylene carbonate (FEC).) Reprinted from Reference[28] with permission from the American Chemical Society.

During electrochemical cycling, Si anodes show considerable (~300%) volumetric change accompanied by various phenomena that affect the cell performance and durability, as shown in Figure 1 - 3.[22, 29] In addition, an electrolyte-decomposition-induced solid electrolyte interphase (SEI) is formed in the first lithiation (Figure 1 - 3 (b)). In subsequent lithiation/delithiation cycles, the (c) continuous SEI formation/decomposition, (d) increasing crystallization/amorphization-induced internal stress, (e) Si particle pulverization, and (f) changes in the Si electrode morphology occur accompanied by the loss of electrical contact, resulting in rapid capacity fading.

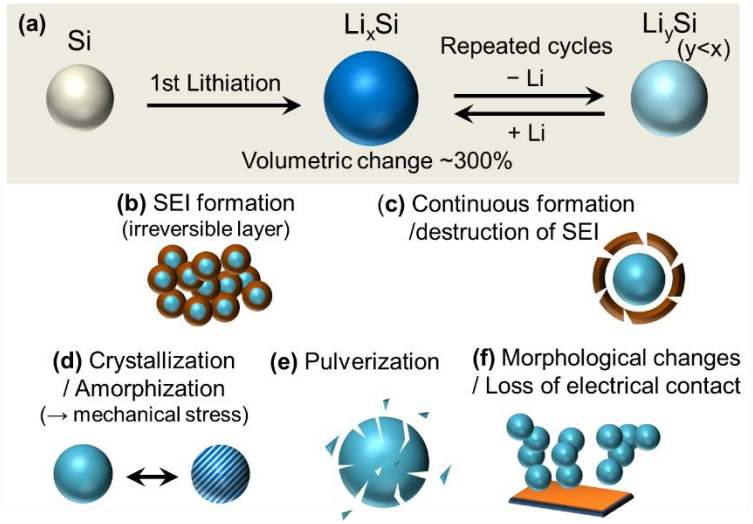

Figure 1 - 3. Schematic diagram of lithiation/delithiation and related phenomena in Si anodes: (a) first lithiation and repeated cycles showing volumetric changes (~300%); (b) formation of solid electrolyte interphase (SEI); (c) continuous SEI formation/decomposition; (d) crystallization/amorphization; (e) pulverization; (f) morphological changes and loss of electrical contact. Although these phenomena are common in both liquid- and solid-based batteries, (b) and (c) (related to SEI formation) are more likely to occur in liquid organic electrolytes showing narrow electrochemical potential windows.

Initial stage of lithiation/delithiation cycles

The plateaus in galvanostatic potential profiles indicate the reactions that proceed at each potential. Differential capacity (dQ/dV) analysis enables the reactions to be analyzed at the plateau regions. Figures 1 - 4 (a) and (b) show representative examples of galvanostatic lithiation potential profiles and the corresponding dQ/dV curves obtained for crystalline Si, respectively.[30]

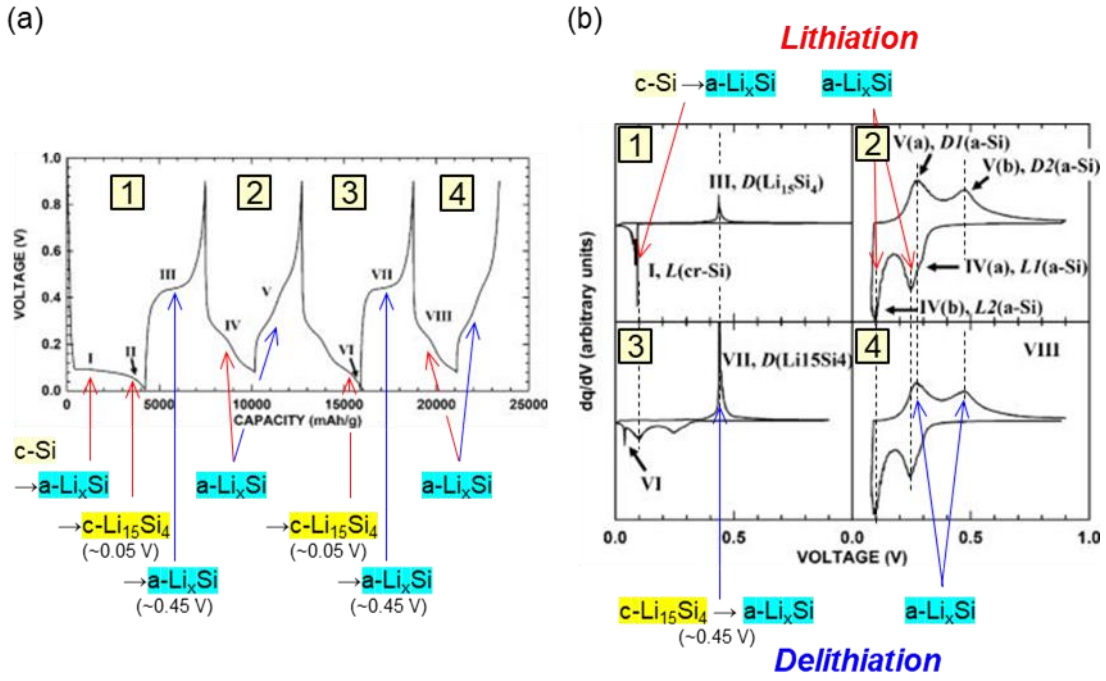

Figure 1 - 4. (a) Potential profiles of crystalline Si anode cycled to illustrate electrochemical phase transitions among crystalline Si (c-Si), $Li_{15}Si_4$, and amorphous Li_xSi (a-Li_xSi). (b) Corresponding differential capacity (dQ/dV) curves. (The electrolyte is a solution of 1 M $LiPF_6$ dissolved in EC/ DEC 1:2 (by weight).) Redrawn based on figure published in Reference[30] with permission from the Electrochemical Society.

In the beginning of the first lithiation (region I, Figure 1 - 4 (a)), the crystalline Si amorphized, and a dQ/dV peak appeared at approximately 0.1 V (Figure 1 - 4 (b)). At the end of the amorphous-Li_xSi lithiation at approximately 0.05 V *vs*. Li^+/Li (region II), crystalline $Li_{15}Si_4$ was formed in the Si powder, thin film, and nanostructured electrodes—which was not predicted by the thermodynamic phase diagram[24] but was detected using various analytical techniques such as XRD, EM,[31-33] and nuclear magnetic resonance (NMR).[34-35] In the successive delithiation plateau (region III), the crystalline $Li_{15}Si_4$ formed in region II eventually amorphized. The delithiation dQ/dV peak at 0.45 V was assignable to the amorphization of the crystalline $Li_{15}Si_4$ on the basis of XRD

measurements (region III, Figure 1 - 4 (b)).[30, 36-38] If lithiation stops above 0.05 V, the Si anode remains amorphous during lithiation/delithiation. In the second lithiation (region IV) when the cutoff potential was above 0.05 V, only the amorphous Li_xSi was formed. In the subsequent second delithiation (region V), the two plateaus and dQ/dV peaks corresponding to the amorphous-Li_xSi delithiation appeared at approximately 0.3 and 0.5 V, as shown in Figures 1 - 4 (a) and (b), respectively. Although the potentials at which these phase transitions occur have been determined using dQ/dV analysis, the relationship between the actual Li–Si composition and structure remains unclear.

In the initial lithiation, an SEI layer was deposited owing to electrolyte decomposition on the Si surface at the Si/electrolyte interfaces at a potential below approximately 1 V *vs*. Li^+/Li.[39-43] The Li consumption by the formation of SEIs is the main cause of the decreased initial coulombic efficiency.[27, 39, 44-47] However, it is known that the SEI can effectively inhibits the subsequent electrolyte decomposition.

Si undergoes significant volumetric expansion/contraction during lithiation/delithiation, respectively. The ratio of the volumetric change when $Li_{4.4}Si$ is formed is approximately 400% based on the lattice volumetric ratio. Various *in-situ* techniques such as atomic force microscopy (AFM),[42, 48-50] transmission electron microscopy (TEM),[31, 51-52] x-ray reflectometry (XRR),[53] neutron reflectometry (NR),[54-56] and optical microscopy[57-59] have all been used to observe the lithiation/delithiation-induced volumetric changes of Si anodes. It has been found that the volumetric expansion of crystalline Si proceeds anisotropically[60] while that of amorphous Si proceeds isotropically.[51] In addition, the volumetric expansion of amorphous Si reportedly varies linearly with Li insertion under galvanostatic lithiation conditions[48, 50, 54-55] and nonlinearly under potentiostatic ones.[56] However, further investigation of the

volumetric/compositional changes of Si anodes is needed to design battery cells accommodating volumetric changes and showing improved performance.

Cycle performance

The severe volumetric changes and the electrical contact loss due to the morphological changes and pulverization are the major reasons for the poor cycle performance of Si anodes.[18, 22, 29] During lithiation/delithiation, the volumetric expansion/contraction occurs owing to changes in the Li content and crystal structure (Figure 1 - 3 (d)).[38, 61-63] Because various substances such as active electrode materials, binders, conductive additives, and separators are usually densely packed in a battery cell to maximize the energy density, the volumetric changes cause a local mechanical stress, resulting in pulverization (Figure 1 - 3 (e)) and the loss of electrical contact (Figure 1 - 3 (f)).

Furthermore, the continuous SEI formation/decomposition deteriorates the Si-anode cycle performance (Figure 1 - 3 (c)). Reportedly, the SEI on the Si surface is easily decomposed by volumetric changes, and a new SEI layer is re-formed because of the contact between the newly exposed Si surface and the electrolyte.[45, 64-67] Such successive Li-ion consumption in the SEI and electrolyte components leads to capacity loss.

1.2.2 Si-based anodes for improving battery performance

A variety of Si-based anodes have been developed to improve the initial battery coulombic efficiency and cycle performance. The material design can be divided into nanostructured Si, Si suboxide (SiO_x), and Si-composite anodes.

Nanostructured Si anodes such as nanowires,[68-69] nanotubes,[47] and nanoporous thin films[70] have been developed to accommodate the volumetric changes in void spaces by stacking shape-controlled materials. However, the introduction of electrochemically inactive void spaces reduces the specific capacity density.

Silicon suboxides (SiO_x) are composed of Si and SiO_2 domains and interfacial suboxides.[71-72] SiO_x-based anodes exhibit higher cyclability than bulk Si. However, SiO_x-based anodes show a relatively large capacity loss in the first lithiation/delithiation.[73-79] The irreversible phases such as Li_2O and Li silicates formed by side reactions of SiO_x and inserted Li contribute to the improved cycle performance by acting as buffer of the volumetric changes.[74, 76]

Those Si-composite anodes are used in combination with carbon-based materials to incorporate the severe volumetric changes of Si.[80-88]

1.3 Si anodes for application to all-solid-state batteries

All-solid-state LIBs

All-solid-state LIBs (ASSBs)[89-91] are promising candidates for application to next-generation lithium batteries. Because ASSBs use nonflammable inorganic solid electrolytes—mainly oxides [$Li_{14}Zn(GeO_4)_4$ (LISICON), $Li_{2.9}PO_{3.3}N_{0.46}$ (LiPON), $Li_7La_3Zr_2O_{12}$, etc.] and sulfides [Li_3PS_4, $Li_{10}GeP_2Si_{12}$, $Li_{9.54}Si_{1.74}P_{1.44}S_{11.7}Cl_{0.3}$, etc.][90, 92] instead of the flammable organic liquid electrolytes used in conventional LIBs—they show improved battery safety and potential power density. In contrast to the relatively few (i.e., <0.5 at most) Li ions transported in liquid electrolytes, more (i.e., reaching 1) Li ions are transported on solid electrolytes, thereby enabling single Li-ion conduction to be exhibited.[93-94]

The utilization of Si anodes in ASSBs has certain advantages. First, side reactions (including SEI formation) are suppressed because of the wide electrochemical potential window of solid electrolytes, resulting in higher cycle performance and initial coulombic efficiency and potentially high power density.[95] However, the Si anodes in ASSBs still

show capacity loss, especially in the first lithiation/delithiation cycles.[96-98] Furthermore, ASSBs needed to be operated under compressive pressure conditions to maintain the ionic and electronic conduction network among the Si particles, solid electrolyte, and current collector. The effect of the compressive pressure on the cycle performance was systematically demonstrated by Yamamoto et al.[99] The specific capacity and cycle performance both improved with increasing compressive pressure, as shown in Figure 1 - 5.

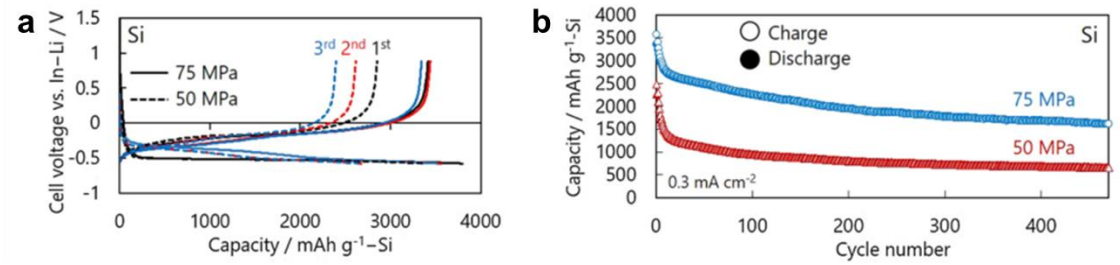

Figure 1 - 5. (a) Potential profiles obtained for three cycles and (b) long-term cycle performances of Si/Li_3PS_4/Li-In cells operated under compressive pressures. (a) Solid and dotted lines and (b) blue and red circles represent 75- and 50-MPa compressive pressures, respectively. Reprinted from Reference[99] with permission from Elsevier.

The advantages of applying Si anodes to ASSBs were previously demonstrated by Cervera et al.[100] Figure 1 - 6 compares the cycle performances of FeS-doped Si-film anodes in liquid ($LiPF_6$ in EC-DEC) and on solid ($70Li_2S$-$30P_2S_5$ glass ceramic) electrolytes.[100] In particular, the solid electrolyte improved the cycle performance of the 400-nm-thick anode, and the capacity retention reached more than 80% after 120 cycles.

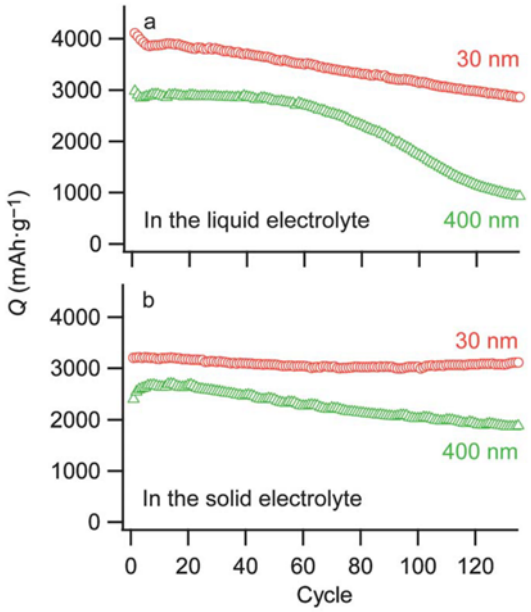

Figure 1 - 6. Cycle performances of 30- and 400-nm-thick Si–FeS-film anodes in (a) liquid electrolyte consisting of 1 M $LiPF_6$/EC–DEC and on (b) solid electrolyte consisting of $70Li_2S–30P_2S_5$. Reprinted from Reference[100] with permission from the Royal Society of Chemistry.

Si thin-film anodes in all-solid-state batteries

The simple structure of thin-film batteries fabricated with a modified interface between the anode and solid electrolyte is attractive for fundamental characterization. In addition, the anode-material loading can be precisely quantified by controlling deposition conditions such as rate and area. Therefore, the integration of electrical current can be appropriately converted into the amount of Li inserted into Si anodes, which is advantageous for quantitatively analyzing the intrinsic properties of Si anodes.

The introduction of porous-structured Si anodes to ASSBs reportedly improves the ASSB cycle performance and rate capability.[98, 101] For example, Sakabe et al. prepared porous Si thin-film anodes by radio-frequency sputtering under He gas and used the anodes on sulfide-based solid electrolytes.[98] The thin-film batteries showed a high

reversible capacity of approximately 3,000 mAh g^{-1} in addition to high capacity retention and rate capability.

Furthermore, various methods to prepare Si anodes without using expensive vacuum systems have been developed. Ohta et al. prepared Si-nanoparticle anodes by spray deposition.[102] In the first lithiation, the constituent particles appreciably coalesced and compacted owing to volumetric expansion in the confined space between the solid electrolyte and current collector, as shown in Figure 1 - 7. Even in sprayed Si-nanoparticle anodes, the nanoparticles firmly adhered to each other owing to lithiation, resulting in high cycle performance and rate capability comparable to those of evaporated continuous-Si-film anodes.

Clearly, the application of Si thin-film anodes to ASSBs is advantageous for both analyzing and improving the cycle performance, initial coulombic efficiency, and rate capability.

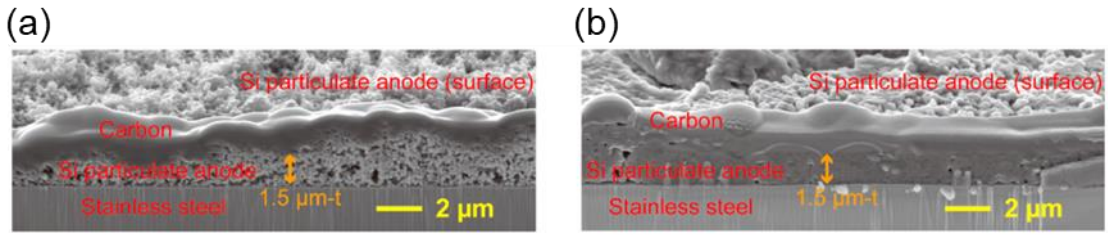

Figure 1 - 7. Cross-sectional SEM images of (a) as-prepared Si particulate and (b) fully charged (lithiated) anodes. Reprinted from Reference[102] with permission from the American Chemical Society.

1.4 *In-situ* observation for electrochemical reactions in batteries

Various battery materials including high-capacity electrodes and high-ionic-conductivity solid electrolytes have been developed for application to ASSBs to improve

battery performance and fabricate next-generation practical batteries.[90, 103] Owing to the remarkable progress to date, the battery-material fundamental properties and their relationship to electrochemical performance must be determined.

Battery materials have been commonly characterized using *ex-situ* and/or postprocessing techniques, i.e., the battery properties are characterized after either electrochemical cycling or cell disassembly. However, considerable information is lost using such approaches because samples are only investigated at certain states of charge.[104] In addition, battery materials themselves are often air sensitive and may undergo undesirable side reactions when transferred from the battery test environment to the measurement apparatus, which may further complicate interpreting the test results.[105] It is therefore essential to establish a method of transferring samples to the measurement apparatus without exposing them to air in addition to developing *in-situ* electrochemical approaches to obtain chemical and/or electronic information under applied bias conditions.

To date, various *in-situ* techniques have been developed based on electron microscopy,[31, 33, 51, 106] x-ray diffraction and scattering,[107-108] and spectroscopy[109-112] to investigate the electrochemical processes of energy-conversion devices including ASSBs. To conduct such advanced *in-situ* measurements, the implementation of various functional components such as bias application system and transfer vessel are essential. Furthermore, it is necessary to tune the measurement conditions on a time scale suitable for observing the phenomena of interest.

1.5 Objective and outline

The objective of this thesis is to elucidate the electrochemical lithiation/delithiation

mechanism of Si-based anodes for application to ASSBs. The relationships among Li concentration, chemical oxidation states and composition, crystalline structure, volumetric expansion, and reaction byproducts formed during lithiation/delithiation of amorphous-Si and SiO_x thin-film anodes were systematically investigated to discuss their effects on electrode performance. The amorphous Si anodes typically exhibit higher cycle performances than crystalline Si ones.[113-115] Therefore, the amorphous-Si thin-film anodes were prepared using radio-frequency sputtering and used for the measurements.

A series of *in-situ* electrochemical X-ray photoelectron spectroscopy (XPS) techniques was developed to analyze the fundamental properties during lithiation/delithiation and enabled chemical information to be obtained without disassembling the batteries and exposing them to air. In addition to analyzing the first lithiation/delithiation cycles, lithiation and delithiation were both monitored during long-term cycling to elucidate the causes of rapid capacity fading, which is the bottleneck for the practical application of Si anodes.

As mentioned in Section 1.2.2, it is proposed that reaction byproducts such as Li_2O and Li silicates in SiO_x anodes act as buffers of volumetric changes to improve the cycle performance. However, the fundamental electrochemical properties and formation mechanism of such byproducts remain unclear. Therefore, lithiation and delithiation processes of SiO_x thin-film anodes prepared by introducing a small amount of oxygen during sputtering were also observed *in situ*.

Based on the foregoing characterization of the amorphous-Si and SiO_x thin-film anodes, guidelines were proposed for designing Si-based anodes and improving their cycle performance.

This thesis is divided to seven chapters as follows.

Chapter 1

Chapter 2. Experimental

The experimental details such as preparation of thin-film cells consisting of either amorphous Si or SiO_x and $Li_{6.6}La_3Zr_{1.6}Ta_{0.4}O_{12}$ (LLZT)/metallic Li and the characterization techniques used in the present study are described.

Chapter 3. Solution species quantitatively observed using environmental cells and X-ray photoelectron spectroscopy

Liquid samples enclosed in environmental cells with a 5-nm-thick silicon-nitride photoelectron window was measured by our *in-situ* XPS apparatus. Operation of the *in-situ* system and quantitative analysis were demonstrated.

Chapter 4. **Static and dynamic analyses of initial lithiation/delithiation of amorphous-Si thin-film electrodes**

The first lithiation/delithiation cycles of a Si/LLZT/Li-configured amorphous-Si thin-film electrode were investigated using *in-situ* XPS. Reversible Li_xSi and irreversible species such as Li_2O, Li_2CO_3, and Li silicates were observed after the first lithiation. In addition, the Li_xSi crystal structural evolution was dynamically analyzed during lithiation/delithiation. Furthermore, the volumetric expansion and nanomechanical properties of the Si thin-film electrode were monitored using *in-situ* electrochemical atomic force microscopy (AFM) in the first lithiation.

Chapter 5. Long-term cycle performance and capacity fading of Si-thin-film electrodes

The successive lithiation/delithiation of the amorphous-Si thin-film electrodes up to 100 cycles were investigated using *in-situ* XPS and differential capacity (dQ/dV) curves to clarify the effect of long-term cycling on capacity fading. The growth of irreversible phases such as Li silicates and Li_2CO_3 and phase transition were correlated with the cell

overvoltage and decreased Li insertion.

Chapter 6. Static analysis of lithiation/delithiation of amorphous-SiO_x thin-film electrodes

The successive lithiation/delithiation of the amorphous-SiO_x thin-film electrode on the LLZT solid electrolyte were investigated using *in-situ* XPS and compared with those of the amorphous Si thin-film electrodes discussed in the previous chapters. The role of irreversible byproducts such as Li_2O, Li silicates, and Li_2CO_3 formed as a result of side reactions of inserted Li with SiO_x were discussed.

Finally, **Chapter 7** summarizes the present results and the overall thesis, together with future research prospects.

References

1. Sekai, K.; Azuma, H.; Omaru, A.; Fujita, S.; Imoto, H.; Endo, T.; Yamaura, K.; Nishi, Y.; Mashiko, S.; Yokogawa, M., Lithium-ion rechargeable cells with $LiCoO_2$ and carbon electrodes. *J. Power Sources* **1993,** *43* (1), 241-244.
2. Tarascon, J. M.; Armand, M., Issues and challenges facing rechargeable lithium batteries. *Nature* **2001,** *414* (6861), 359-367.
3. Scrosati, B.; Garche, J., Lithium batteries: Status, prospects and future. *J. Power Sources* **2010,** *195* (9), 2419-2430.
4. Hausbrand, R.; Cherkashinin, G.; Ehrenberg, H.; Gröting, M.; Albe, K.; Hess, C.; Jaegermann, W., Fundamental degradation mechanisms of layered oxide Li-ion battery cathode materials: Methodology, insights and novel approaches. *Mater. Sci. Eng., B* **2015,** *192*, 3-25.
5. Nitta, N.; Wu, F.; Lee, J. T.; Yushin, G., Li-ion battery materials: present and future. *Mater. Today* **2015,** *18* (5), 252-264.
6. Ozawa, K., Lithium-ion rechargeable batteries with $LiCoO_2$ and carbon electrodes: the $LiCoO_2$/C system. *Solid State Ion.* **1994,** *69* (3), 212-221.
7. The Nobel Prize in Chemistry 2019. NobelPrize.org. Nobel Media AB 2020. https://www.nobelprize.org/prizes/chemistry/2019/summary/ (accessed Sun. 11 Oct 2020.).
8. Whittingham, M. S., Electrical Energy Storage and Intercalation Chemistry. *Science* **1976,** *192* (4244), 1126.

9. Whittingham, M. S., Lithium Batteries and Cathode Materials. *Chem. Rev.* **2004,** *104* (10), 4271-4302.
10. Mizushima, K.; Jones, P. C.; Wiseman, P. J.; Goodenough, J. B., Li_xCoO_2 (0<x<-1): A new cathode material for batteries of high energy density. *Mater. Res. Bull.* **1980,** *15* (6), 783-789.
11. Goodenough, J. B.; Mizuchima, K. Electrochemical cell with new fast ion conductors. U.S. Patent 4302518, Nov. 24, 1981.
12. Yoshino, A., The Birth of the Lithium-Ion Battery. *Angew. Chem. Int. Ed.* **2012,** *51* (24), 5798-5800.
13. Society 5.0. https://www8.cao.go.jp/cstp/english/society5_0/index.html (accessed Sun. 15 Nov 2020.).
14. Yazami, R.; Touzain, P., A reversible graphite-lithium negative electrode for electrochemical generators. *J. Power Sources* **1983,** *9* (3), 365-371.
15. Billaud, D.; Henry, F. X.; Willmann, P., Electrochemical synthesis of binary graphite-lithium intercalation compounds. *Mater. Res. Bull.* **1993,** *28* (5), 477-483.
16. Qi, Y.; Guo, H.; Hector, L. G.; Timmons, A., Threefold Increase in the Young's Modulus of Graphite Negative Electrode during Lithium Intercalation. *J. Electrochem. Soc.* **2010,** *157* (5), A558.
17. Li, W. D.; Song, B. H.; Manthiram, A., High-voltage positive electrode materials for lithium-ion batteries. *Chem. Soc. Rev.* **2017,** *46* (10), 3006-3059.
18. Zhu, B.; Wang, X.; Yao, P.; Li, J.; Zhu, J., Towards high energy density lithium battery anodes: silicon and lithium. *Chem. Sci.* **2019,** *10* (30), 7132-7148.
19. Park, C.-M.; Kim, J.-H.; Kim, H.; Sohn, H.-J., Li-alloy based anode materials for Li secondary batteries. *Chem. Soc. Rev.* **2010,** *39* (8), 3115-3141.
20. Obrovac, M. N.; Chevrier, V. L., Alloy Negative Electrodes for Li-Ion Batteries. *Chem. Rev.* **2014,** *114* (23), 11444-11502.
21. Liu, D.; Liu, Z. j.; Li, X.; Xie, W.; Wang, Q.; Liu, Q.; Fu, Y.; He, D., Group IVA Element (Si, Ge, Sn)-Based Alloying/Dealloying Anodes as Negative Electrodes for Full-Cell Lithium-Ion Batteries. *Small* **2017,** *13* (45), 1702000.
22. Feng, K.; Li, M.; Liu, W.; Kashkooli, A. G.; Xiao, X.; Cai, M.; Chen, Z., Silicon-Based Anodes for Lithium-Ion Batteries: From Fundamentals to Practical Applications. *Small* **2018,** *14* (8), 1702737.
23. Salah, M.; Murphy, P.; Hall, C.; Francis, C.; Kerr, R.; Fabretto, M., Pure silicon thin-film anodes for lithium-ion batteries: A review. *J. Power Sources* **2019,** *414*, 48-67.
24. Okamoto, H., The Li-Si (Lithium-Silicon) system. *Bulletin of Alloy Phase Diagrams* **1990,** *11* (3), 306-312.
25. Limthongkul, P.; Jang, Y.-I.; Dudney, N. J.; Chiang, Y.-M., Electrochemically-driven solid-state amorphization in lithium-silicon alloys and implications for lithium storage. *Acta Mater.* **2003,** *51* (4), 1103-1113.
26. Limthongkul, P.; Jang, Y.-I.; Dudney, N. J.; Chiang, Y.-M., Electrochemically-driven solid-state amorphization in lithium–metal anodes. *J. Power Sources* **2003,** *119-121*, 604-609.
27. Radvanyi, E.; De Vito, E.; Porcher, W.; Larbi, S. J. S., An XPS/AES comparative study of the surface

behaviour of nano-silicon anodes for Li-ion batteries. *J. Anal. At. Spectrom.* **2014,** *29* (6), 1120-1131.

28. Wu, Q.; Shi, B.; Bareño, J.; Liu, Y.; Maroni, V. A.; Zhai, D.; Dees, D. W.; Lu, W., Investigations of Si Thin Films as Anode of Lithium-Ion Batteries. *ACS Appl. Mater. Inter.* **2018,** *10* (4), 3487-3494.
29. Jin, Y.; Zhu, B.; Lu, Z.; Liu, N.; Zhu, J., Challenges and Recent Progress in the Development of Si Anodes for Lithium-Ion Battery. *Adv. Energy Mater.* **2017,** *7* (23), 1700715.
30. Obrovac, M. N.; Krause, L. J., Reversible Cycling of Crystalline Silicon Powder. *J. Electrochem. Soc.* **2007,** *154* (2), A103-A108.
31. Wang, J. W.; He, Y.; Fan, F.; Liu, X. H.; Xia, S.; Liu, Y.; Harris, C. T.; Li, H.; Huang, J. Y.; Mao, S. X.; Zhu, T., Two-Phase Electrochemical Lithiation in Amorphous Silicon. *Nano Lett.* **2013,** *13* (2), 709-715.
32. Liu, X. H.; Wang, J. W.; Huang, S.; Fan, F.; Huang, X.; Liu, Y.; Krylyuk, S.; Yoo, J.; Dayeh, S. A.; Davydov, A. V.; Mao, S. X.; Picraux, S. T.; Zhang, S.; Li, J.; Zhu, T.; Huang, J. Y., In situ atomic-scale imaging of electrochemical lithiation in silicon. *Nat. Nanotechnol.* **2012,** *7*, 749.
33. Gu, M.; Wang, Z. G.; Connell, J. G.; Perea, D. E.; Lauhon, L. J.; Gao, F.; Wang, C. M., Electronic Origin for the Phase Transition from Amorphous Li_xSi to Crystalline $Li_{15}Si_4$. *ACS Nano* **2013,** *7* (7), 6303-6309.
34. Key, B.; Bhattacharyya, R.; Morcrette, M.; Seznéc, V.; Tarascon, J.-M.; Grey, C. P., Real-Time NMR Investigations of Structural Changes in Silicon Electrodes for Lithium-Ion Batteries. *J. Am. Chem. Soc.* **2009,** *131* (26), 9239-9249.
35. Ogata, K.; Salager, E.; Kerr, C. J.; Fraser, A. E.; Ducati, C.; Morris, A. J.; Hofmann, S.; Grey, C. P., Revealing lithium–silicide phase transformations in nano-structured silicon-based lithium ion batteries via in situ NMR spectroscopy. *Nat Commun* **2014,** *5* (1), 3217.
36. Obrovac, M. N.; Christensen, L., Structural Changes in Silicon Anodes during Lithium Insertion/Extraction. *Electrochem. Solid-State Lett.* **2004,** *7* (5), A93-A96.
37. Hatchard, T. D.; Dahn, J. R., In Situ XRD and Electrochemical Study of the Reaction of Lithium with Amorphous Silicon. *J. Electrochem. Soc.* **2004,** *151* (6), A838.
38. Iaboni, D. S. M.; Obrovac, M. N., $Li_{15}Si_4$ Formation in Silicon Thin Film Negative Electrodes. *J. Electrochem. Soc.* **2016,** *163* (2), A255-A261.
39. Cao, C. T.; Steinruck, H. G.; Shyam, B.; Stone, K. H.; Toney, M. F., In Situ Study of Silicon Electrode Lithiation with X-ray Reflectivity. *Nano Lett.* **2016,** *16* (12), 7394-7401.
40. Cao, C.; Abate, I. I.; Sivonxay, E.; Shyam, B.; Jia, C.; Moritz, B.; Devereaux, T. P.; Persson, K. A.; Steinrück, H.-G.; Toney, M. F., Solid Electrolyte Interphase on Native Oxide-Terminated Silicon Anodes for Li-Ion Batteries. *Joule* **2019,** *3* (3), 762-781.
41. Cao, C.; Shyam, B.; Wang, J.; Toney, M. F.; Steinrück, H.-G., Shedding X-ray Light on the Interfacial Electrochemistry of Silicon Anodes for Li-Ion Batteries. *Acc. Chem. Res.* **2019,** *52* (9), 2673-2683.
42. Breitung, B.; Baumann, P.; Sommer, H.; Janek, J.; Brezesinski, T., In situ and operando atomic force

microscopy of high-capacity nano-silicon based electrodes for lithium-ion batteries. *Nanoscale* **2016,** *8* (29), 14048-14056.

43. Benning, S.; Chen, C.; Eichel, R.-A.; Notten, P. H. L.; Hausen, F., Direct Observation of SEI Formation and Lithiation in Thin-Film Silicon Electrodes via in Situ Electrochemical Atomic Force Microscopy. *ACS Applied Energy Materials* **2019,** *2* (9), 6761-6767.
44. Liu, N.; Lu, Z.; Zhao, J.; McDowell, M. T.; Lee, H.-W.; Zhao, W.; Cui, Y., A pomegranate-inspired nanoscale design for large-volume-change lithium battery anodes. *Nat. Nanotechnol.* **2014,** *9* (3), 187-192.
45. Jerliu, B.; Hüger, E.; Horisberger, M.; Stahn, J.; Schmidt, H., Irreversible lithium storage during lithiation of amorphous silicon thin film electrodes studied by in-situ neutron reflectometry. *J. Power Sources* **2017,** *359*, 415-421.
46. Michan, A. L.; Divitini, G.; Pell, A. J.; Leskes, M.; Ducati, C.; Grey, C. P., Solid Electrolyte Interphase Growth and Capacity Loss in Silicon Electrodes. *J. Am. Chem. Soc.* **2016,** *138* (25), 7918-7931.
47. Wu, H.; Chan, G.; Choi, J. W.; Ryu, I.; Yao, Y.; McDowell, M. T.; Lee, S. W.; Jackson, A.; Yang, Y.; Hu, L.; Cui, Y., Stable cycling of double-walled silicon nanotube battery anodes through solid–electrolyte interphase control. *Nat. Nanotechnol.* **2012,** *7* (5), 310-315.
48. He, Y.; Yu, X.; Li, G.; Wang, R.; Li, H.; Wang, Y.; Gao, H.; Huang, X., Shape evolution of patterned amorphous and polycrystalline silicon microarray thin film electrodes caused by lithium insertion and extraction. *J. Power Sources* **2012,** *216*, 131-138.
49. Becker, C. R.; Strawhecker, K. E.; McAllister, Q. P.; Lundgren, C. A., In Situ Atomic Force Microscopy of Lithiation and Delithiation of Silicon Nanostructures for Lithium Ion Batteries. *ACS Nano* **2013,** *7* (10), 9173-9182.
50. Beaulieu, L. Y.; Hatchard, T. D.; Bonakdarpour, A.; Fleischauer, M. D.; Dahn, J. R., Reaction of Li with Alloy Thin Films Studied by In Situ AFM. *J. Electrochem. Soc.* **2003,** *150* (11), A1457.
51. McDowell, M. T.; Lee, S. W.; Harris, J. T.; Korgel, B. A.; Wang, C.; Nix, W. D.; Cui, Y., In Situ TEM of Two-Phase Lithiation of Amorphous Silicon Nanospheres. *Nano Lett.* **2013,** *13* (2), 758-764.
52. McDowell, M. T.; Ryu, I.; Lee, S. W.; Wang, C.; Nix, W. D.; Cui, Y., Studying the Kinetics of Crystalline Silicon Nanoparticle Lithiation with In Situ Transmission Electron Microscopy. *Adv. Mater.* **2012,** *24* (45), 6034-6041.
53. Steinrück, H.-G.; Cao, C.; Veith, G. M.; Toney, M. F., Toward quantifying capacity losses due to solid electrolyte interphase evolution in silicon thin film batteries. *J. Chem. Phys.* **2020,** *152* (8), 084702.
54. Uxa, D.; Jerliu, B.; Hüger, E.; Dörrer, L.; Horisberger, M.; Stahn, J.; Schmidt, H., On the Lithiation Mechanism of Amorphous Silicon Electrodes in Li-Ion Batteries. *J. Phys. Chem. C* **2019,** *123* (36), 22027-22039.
55. Jerliu, B.; Hüger, E.; Dörrer, L.; Seidlhofer, B. K.; Steitz, R.; Oberst, V.; Geckle, U.; Bruns, M.; Schmidt, H., Volume Expansion during Lithiation of Amorphous Silicon Thin Film Electrodes Studied

by In-Operando Neutron Reflectometry. *The Journal of Physical Chemistry C* **2014,** *118* (18), 9395-9399.

56. Schmidt, H.; Jerliu, B.; Hüger, E.; Stahn, J., Volume expansion of amorphous silicon electrodes during potentiostatic lithiation of Li-ion batteries. *Electrochem. Commun.* **2020,** *115*, 106738.
57. Duay, J.; Schroder, K. W.; Murugesan, S.; Stevenson, K. J., Monitoring Volumetric Changes in Silicon Thin-Film Anodes through In Situ Optical Diffraction Microscopy. *ACS Appl. Mater. Inter.* **2016,** *8* (27), 17642-17650.
58. Nishikawa, K.; Munakata, H.; Kanamura, K., In-situ observation of one silicon particle during the first charging. *J. Power Sources* **2013,** *243*, 630-634.
59. Nishikawa, K.; Moon, J.; Kanamura, K., In-situ observation of volume expansion behavior of a silicon particle in various electrolytes. *J. Power Sources* **2016,** *302*, 46-52.
60. Lee, S. W.; McDowell, M. T.; Choi, J. W.; Cui, Y., Anomalous Shape Changes of Silicon Nanopillars by Electrochemical Lithiation. *Nano Lett.* **2011,** *11* (7), 3034-3039.
61. Gao, H.; Xiao, L.; Plümel, I.; Xu, G.-L.; Ren, Y.; Zuo, X.; Liu, Y.; Schulz, C.; Wiggers, H.; Amine, K.; Chen, Z., Parasitic Reactions in Nanosized Silicon Anodes for Lithium-Ion Batteries. *Nano Lett.* **2017,** *17* (3), 1512-1519.
62. Xie, H.; Sayed, S. Y.; Kalisvaart, W. P.; Schaper, S. J.; Müller-Buschbaum, P.; Luber, E. J.; Olsen, B. C.; Haese, M.; Buriak, J. M., Adhesion and Surface Layers on Silicon Anodes Suppress Formation of c-$Li_{3.75}Si$ and Solid-Electrolyte Interphase. *ACS Appl. Energy Mater.* **2020,** *3* (2), 1609-1616.
63. Chon, M. J.; Sethuraman, V. A.; McCormick, A.; Srinivasan, V.; Guduru, P. R., Real-Time Measurement of Stress and Damage Evolution during Initial Lithiation of Crystalline Silicon. *Phys. Rev. Lett.* **2011,** *107* (4), 4.
64. Cho, J.-H.; Picraux, S. T., Silicon Nanowire Degradation and Stabilization during Lithium Cycling by SEI Layer Formation. *Nano Lett.* **2014,** *14* (6), 3088-3095.
65. Boniface, M.; Quazuguel, L.; Danet, J.; Guyomard, D.; Moreau, P.; Bayle-Guillemaud, P., Nanoscale Chemical Evolution of Silicon Negative Electrodes Characterized by Low-Loss STEM-EELS. *Nano Lett.* **2016,** *16* (12), 7381-7388.
66. Dupré, N.; Moreau, P.; De Vito, E.; Quazuguel, L.; Boniface, M.; Bordes, A.; Rudisch, C.; Bayle-Guillemaud, P.; Guyomard, D., Multiprobe Study of the Solid Electrolyte Interphase on Silicon-Based Electrodes in Full-Cell Configuration. *Chem. Mater.* **2016,** *28* (8), 2557-2572.
67. Xu, Y.; Wood, K.; Coyle, J.; Engtrakul, C.; Teeter, G.; Stoldt, C.; Burrell, A.; Zakutayev, A., Chemistry of Electrolyte Reduction on Lithium Silicide. *J. Phys. Chem. C* **2019,** *123* (21), 13219-13224.
68. Chan, C. K.; Peng, H.; Liu, G.; McIlwrath, K.; Zhang, X. F.; Huggins, R. A.; Cui, Y., High-performance lithium battery anodes using silicon nanowires. *Nat. Nanotechnol.* **2008,** *3* (1), 31-35.
69. McDowell, M. T.; Cui, Y., Single Nanostructure Electrochemical Devices for Studying Electronic Properties and Structural Changes in Lithiated Si Nanowires. *Adv. Energy Mater.* **2011,** *1* (5), 894-900.

70. Kim, H.; Han, B.; Choo, J.; Cho, J., Three-Dimensional Porous Silicon Particles for Use in High-Performance Lithium Secondary Batteries. *Angew. Chem. Int. Ed.* **2008,** *47* (52), 10151-10154.
71. Sepehri-Amin, H.; Ohkubo, T.; Kodzuka, M.; Yamamura, H.; Saito, T.; Iba, H.; Hono, K., Evidence for nano-Si clusters in amorphous SiO anode materials for rechargeable Li-ion batteries. *Scripta Mater.* **2013,** *69* (1), 92-95.
72. Hirata, A.; Kohara, S.; Asada, T.; Arao, M.; Yogi, C.; Imai, H.; Tan, Y.; Fujita, T.; Chen, M., Atomic-scale disproportionation in amorphous silicon monoxide. *Nat. Commun.* **2016,** *7* (1), 11591.
73. Miyachi, M.; Yamamoto, H.; Kawai, H.; Ohta, T.; Shirakata, M., Analysis of SiO Anodes for Lithium-Ion Batteries. *J. Electrochem. Soc.* **2005,** *152* (10), A2089-A2091.
74. Miyazaki, R.; Ohta, N.; Ohnishi, T.; Takada, K., Anode properties of silicon-rich amorphous silicon suboxide films in all-solid-state lithium batteries. *J. Power Sources* **2016,** *329*, 41-49.
75. Miyazaki, R., High-Capacity Anode Materials for All-Solid-State Lithium Batteries. *Front. Energy Res.* **2020,** *8* (171).
76. Haruta, M.; Doi, T.; Inaba, M., Oxygen-Content Dependence of Cycle Performance and Morphology Changes in Amorphous-SiO_x Thin-Film Negative Electrodes for Lithium-Ion Batteries. *J. Electrochem. Soc.* **2019,** *166* (2), A258-A263.
77. Yu, B. C.; Hwa, Y.; Park, C. M.; Sohn, H. J., Reaction mechanism and enhancement of cyclability of SiO anodes by surface etching with NaOH for Li-ion batteries. *J. Mater. Chem. A* **2013,** *1* (15), 4820-4825.
78. Nguyen, C. C.; Choi, H.; Song, S. W., Roles of Oxygen and Interfacial Stabilization in Enhancing the Cycling Ability of Silicon Oxide Anodes for Rechargeable Lithium Batteries. *J. Electrochem. Soc.* **2013,** *160* (6), A906-A914.
79. Takezawa, H.; Iwamoto, K.; Ito, S.; Yoshizawa, H., Electrochemical behaviors of nonstoichiometric silicon suboxides (SiO_x) film prepared by reactive evaporation for lithium rechargeable batteries. *J. Power Sources* **2013,** *244*, 149-157.
80. Chae, S.; Choi, S.-H.; Kim, N.; Sung, J.; Cho, J., Integration of Graphite and Silicon Anodes for the Commercialization of High-Energy Lithium-Ion Batteries. *Angew. Chem. Int. Ed.* **2020,** *59* (1), 110-135.
81. Fan, Y.; Zhang, Q.; Xiao, Q.; Wang, X.; Huang, K., High performance lithium ion battery anodes based on carbon nanotube–silicon core–shell nanowires with controlled morphology. *Carbon* **2013,** *59*, 264-269.
82. Forney, M. W.; Ganter, M. J.; Staub, J. W.; Ridgley, R. D.; Landi, B. J., Prelithiation of Silicon–Carbon Nanotube Anodes for Lithium Ion Batteries by Stabilized Lithium Metal Powder (SLMP). *Nano Lett.* **2013,** *13* (9), 4158-4163.
83. Evanoff, K.; Magasinski, A.; Yang, J.; Yushin, G., Nanosilicon-Coated Graphene Granules as Anodes for Li-Ion Batteries. *Adv. Energy Mater.* **2011,** *1* (4), 495-498.

84. Lee, J. K.; Smith, K. B.; Hayner, C. M.; Kung, H. H., Silicon nanoparticles–graphene paper composites for Li ion battery anodes. *Chem. Commun.* **2010,** *46* (12), 2025-2027.
85. Chan, C. K.; Patel, R. N.; O'Connell, M. J.; Korgel, B. A.; Cui, Y., Solution-Grown Silicon Nanowires for Lithium-Ion Battery Anodes. *ACS Nano* **2010,** *4* (3), 1443-1450.
86. Liu, N.; Wu, H.; McDowell, M. T.; Yao, Y.; Wang, C.; Cui, Y., A Yolk-Shell Design for Stabilized and Scalable Li-Ion Battery Alloy Anodes. *Nano Lett.* **2012,** *12* (6), 3315-3321.
87. Yang, J.; Wang, Y.-X.; Chou, S.-L.; Zhang, R.; Xu, Y.; Fan, J.; Zhang, W.-x.; Kun Liu, H.; Zhao, D.; Xue Dou, S., Yolk-shell silicon-mesoporous carbon anode with compact solid electrolyte interphase film for superior lithium-ion batteries. *Nano Energy* **2015,** *18*, 133-142.
88. Wang, J.; Zhao, H.; He, J.; Wang, C.; Wang, J., Nano-sized SiO_x/C composite anode for lithium ion batteries. *J. Power Sources* **2011,** *196* (10), 4811-4815.
89. Famprikis, T.; Canepa, P.; Dawson, J. A.; Islam, M. S.; Masquelier, C., Fundamentals of inorganic solid-state electrolytes for batteries. *Nature Mater.* **2019,** *18* (12), 1278-1291.
90. Takada, K., Progress in solid electrolytes toward realizing solid-state lithium batteries. *J. Power Sources* **2018,** *394*, 74-85.
91. Umeshbabu, E.; Zheng, B.; Yang, Y., Recent Progress in All-Solid-State Lithium−Sulfur Batteries Using High Li-Ion Conductive Solid Electrolytes. *Electrochemical Energy Reviews* **2019,** *2* (2), 199-230.
92. Kamaya, N.; Homma, K.; Yamakawa, Y.; Hirayama, M.; Kanno, R.; Yonemura, M.; Kamiyama, T.; Kato, Y.; Hama, S.; Kawamoto, K.; Mitsui, A., A lithium superionic conductor. *Nat. Mater.* **2011,** *10* (9), 682-6.
93. Capiglia, C.; Saito, Y.; Kageyama, H.; Mustarelli, P.; Iwamoto, T.; Tabuchi, T.; Tukamoto, H., ^{7}Li and ^{19}F diffusion coefficients and thermal properties of non-aqueous electrolyte solutions for rechargeable lithium batteries. *J. Power Sources* **1999,** *81-82*, 859-862.
94. Zugmann, S.; Gores, H. J., Transference Numbers of Ions in Electrolytes. In *Encyclopedia of Applied Electrochemistry*, Kreysa, G.; Ota, K.-i.; Savinell, R. F., Eds. Springer New York: New York, NY, 2014; pp 2086-2091.
95. Zhu, Y.; He, X.; Mo, Y., First principles study on electrochemical and chemical stability of solid electrolyte–electrode interfaces in all-solid-state Li-ion batteries. *J. Mater. Chem. A* **2016,** *4* (9), 3253-3266.
96. Cras, F. L.; Pecquenard, B.; Dubois, V.; Phan, V.-P.; Guy-Bouyssou, D., All-Solid-State Lithium-Ion Microbatteries Using Silicon Nanofilm Anodes: High Performance and Memory Effect. *Adv. Energy Mater.* **2015,** *5* (19), 1501061.
97. Chen, C.; Li, Q.; Li, Y.; Cui, Z.; Guo, X.; Li, H., Sustainable interfaces between Si anodes and garnet electrolytes for room-temperature solid-state batteries. *ACS Appl. Mater. Interfaces* **2018,** *10* (2), 2185-2190.

98. Sakabe, J.; Ohta, N.; Ohnishi, T.; Mitsuishi, K.; Takada, K., Porous amorphous silicon film anodes for high-capacity and stable all-solid-state lithium batteries. *Commun. Chem.* **2018,** *1* (1), 24.
99. Yamamoto, M.; Terauchi, Y.; Sakuda, A.; Kato, A.; Takahashi, M., Effects of volume variations under different compressive pressures on the performance and microstructure of all-solid-state batteries. *J. Power Sources* **2020,** *473*, 228595.
100. Cervera, R. B.; Suzuki, N.; Ohnishi, T.; Osada, M.; Mitsuishi, K.; Kambara, T.; Takada, K., High performance silicon-based anodes in solid-state lithium batteries. *Energy Environ. Sci.* **2014,** *7* (2), 662-666.
101. Okuno, R.; Yamamoto, M.; Terauchi, Y.; Takahashi, M., Stable cyclability of porous Si anode applied for sulfide-based all-solid-state batteries. *Energy Procedia* **2019,** *156*, 183-186.
102. Ohta, N.; Kimura, S.; Sakabe, J.; Mitsuishi, K.; Ohnishi, T.; Takada, K., Anode properties of Si nanoparticles in all-solid-state Li batteries. *ACS Appl. Energy Mater.* **2019,** *2* (10), 7005-7008.
103. Hori, S.; Suzuki, K.; Hirayama, M.; Kato, Y.; Kanno, R., Lithium superionic conductor $Li_{9.42}Si_{1.02}P_{2.1}S_{9.96}O_{2.04}$ with $Li_{10}GeP_2S_{12}$-type structure in the Li_2S–P_2S_5–SiO_2 pseudoternary system: synthesis, electrochemical properties, and structure–composition relationships. *Front. Energy Res.* **2016,** *4* (38).
104. Boebinger, M. G.; Lewis, J. A.; Sandoval, S. E.; McDowell, M. T., Understanding transformations in battery materials using in situ and operando experiments: progress and outlook. *ACS Energy Lett.* **2020,** *5* (1), 335-345.
105. Liu, D. Q.; Shadike, Z.; Lin, R. Q.; Qian, K.; Li, H.; Li, K. K.; Wang, S. W.; Yu, Q. P.; Liu, M.; Ganapathy, S.; Qin, X. Y.; Yang, Q. H.; Wagemaker, M.; Kang, F. Y.; Yang, X. Q.; Li, B. H., Review of Recent Development of In Situ/Operando Characterization Techniques for Lithium Battery Research. *Adv. Mater.* **2019,** *31* (28), 57.
106. Wang, Z.; Santhanagopalan, D.; Zhang, W.; Wang, F.; Xin, H. L.; He, K.; Li, J.; Dudney, N.; Meng, Y. S., In Situ STEM-EELS Observation of Nanoscale Interfacial Phenomena in All-Solid-State Batteries. *Nano Lett.* **2016,** *16* (6), 3760-7.
107. Misra, S.; Liu, N.; Nelson, J.; Hong, S. S.; Cui, Y.; Toney, M. F., In Situ X-ray Diffraction Studies of (De)lithiation Mechanism in Silicon Nanowire Anodes. *ACS Nano* **2012,** *6* (6), 5465-5473.
108. Shiraki, S.; Shirasawa, T.; Suzuki, T.; Kawasoko, H.; Shimizu, R.; Hitosugi, T., Atomically Well-Ordered Structure at Solid Electrolyte and Electrode Interface Reduces the Interfacial Resistance. *ACS Appl. Mater. Interfaces* **2018,** *10* (48), 41732-41737.
109. Santhanagopalan, D.; Qian, D.; McGilvray, T.; Wang, Z.; Wang, F.; Camino, F.; Graetz, J.; Dudney, N.; Meng, Y. S., Interface Limited Lithium Transport in Solid-State Batteries. *J. Phys. Chem. Lett.* **2014,** *5* (2), 298-303.
110. Liu, X.; Wang, D.; Liu, G.; Srinivasan, V.; Liu, Z.; Hussain, Z.; Yang, W., Distinct charge dynamics in battery electrodes revealed by in situ and operando soft X-ray spectroscopy. *Nat. Commun.* **2013,**

4, 2568.

111. Matsuda, Y.; Kuwata, N.; Okawa, T.; Dorai, A.; Kamishima, O.; Kawamura, J., In situ Raman spectroscopy of Li_xCoO_2 cathode in $Li/Li_3PO_4/LiCoO_2$ all-solid-state thin-film lithium battery. *Solid State Ion.* **2019,** *335*, 7-14.
112. Chen, K.; Shinjo, S.; Sakuda, A.; Yamamoto, K.; Uchiyama, T.; Kuratani, K.; Takeuchi, T.; Orikasa, Y.; Hayashi, A.; Tatsumisago, M.; Kimura, Y.; Nakamura, T.; Amezawa, K.; Uchimoto, Y., Morphological Effect on Reaction Distribution Influenced by Binder Materials in Composite Electrodes for Sheet-type All-Solid-State Lithium-Ion Batteries with the Sulfide-based Solid Electrolyte. *J. Phys. Chem. C* **2019,** *123* (6), 3292-3298.
113. Miyazaki, R.; Ohta, N.; Ohnishi, T.; Sakaguchi, I.; Takada, K., An amorphous Si film anode for all-solid-state lithium batteries. *J. Power Sources* **2014,** *272*, 541-545.
114. Ohara, S.; Suzuki, J.; Sekine, K.; Takamura, T., A thin film silicon anode for Li-ion batteries having a very large specific capacity and long cycle life. *J. Power Sources* **2004,** *136* (2), 303-306.
115. Graetz, J.; Ahn, C. C.; Yazami, R.; Fultz, B., Highly Reversible Lithium Storage in Nanostructured Silicon. *Electrochem. Solid-State Lett.* **2003,** *6* (9), A194.

Chapter 2. Experimental

2.1 Sample preparation

In the early-stage study, Si anode is often evaluated as a cathode versus Li metal anode, i.e., in half-cell configuration.[1] In this section, the preparation method for the Si thin-film cell with a structure of Cu/Si or SiO_x/$Li_{6.6}La_3Zr_{1.6}Ta_{0.4}O_{12}$ (LLZT)/Li is described (Figure 2 - 1).

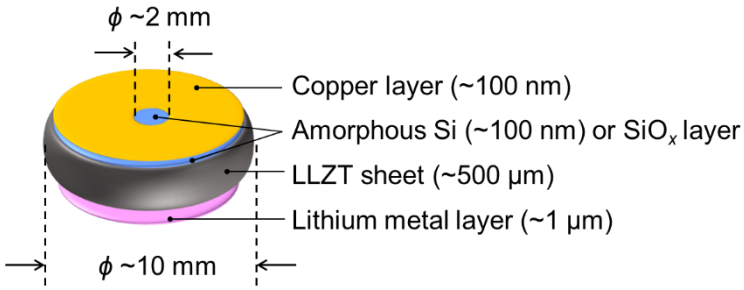

Figure 2 - 1. Schematic illustration of the Cu/amorphous Si or SiO_x/LLZT/Li metal cell.

2.1.1 Solid electrolytes

The garnet-type solid electrolyte was selected in the present study, because of its high ionic conductivity (10^{-4}–10^{-3} S/cm at 25°C), high stability, wide electrochemical window, and high mechanical properties.[2-3] The garnet-type $Li_{6.6}La_3Zr_{1.6}Ta_{0.4}O_{12}$ (LLZT) solid electrolyte sheets (Toshima Manufacturing Co., Ltd., Japan), with the diameter of 10 mm and thickness of 500 μm, were heated at ca. 600°C for two hours by a tubular furnace under an O_2 flow rate of 0.2 L/min to remove the internal water molecules. After transferring the LLZT sheets to the Ar-filled glove box, the surface was polished using 400-grit sand papers to eliminate resistive species such as Li_2CO_3 and LiOH.[4]

2.1.2 Amorphous Si and SiO_x layers

Amorphous Si films, used in Chapters 4 and 5, were deposited on the LLZT sheets by radio-frequency magnetron sputtering (SPAD-2240UM, Advanced Optics Vacuum Co., Ltd.) using Ar as the sputtering gas. The radio-frequency power was 200 W. The LLZT sheets were transferred from Ar-filled glove box to the sputtering chamber at the pressure of about 10^{-5} Pa without exposing to open air. Prior to the deposition, a 5N-pure Si target (Kojundo Chemical Laboratory Co., Ltd.) was pre-sputtered for 30 min to remove the possible oxide layer and impurities at the surface. The thickness of deposited Si on the LLZT sheet was controlled to be ca.100 nm, based on the deposition rate (2.08 Å/s) and time. The thickness of Si film with the deposition time of 37 min was determined by X-ray reflectometry (XRR, see Section 2.3.2).

The SiO_x thin films used in Chapter 6 were prepared on the LLZT sheets by radio-frequency magnetron sputtering using Ar/O_2 gas mixtures.[5] The flow rate of Ar and O_2 gas were set at 20 and 0.15 sccm, respectively. The deposition time was set to 37 min, which is the same time for preparing pure Si thin films with the thickness of ca. 100 nm, to retain the mass of Si in the deposited SiO_x and Si thin films for the calculation of the gravimetric capacity. During the sample manipulation, SiO_x thin film was exposed to air for 5 min.

2.1.3 Current collectors

The surface of sputter-deposited Si layer was coated with a copper layer as a current collector by direct current (DC) sputtering. The samples were mounted on the stage of QUICK COATER (SC-701, Sanyu Electron Co., Ltd.) in the Ar-filled glove box. The Cu deposition was performed at the pressure of about 10^{1} Pa. During the copper deposition, a center circular part with a diameter of about 2 mm was masked using a

stainless-steel stencil mask to yield an uncoated area exposing amorphous Si layer for XPS measurement.

2.1.4 Li metal layers

The LLZT surface of the LLZT/Si/Cu structure was polished by using 400-grit sand papers. The Li metal layer with a diameter of 8.5 mm was thermally deposited on the LLZT surface from a Li wire (Honjo Metal Co., Ltd.). The thickness of Li deposition is approximately 1.3 μm which is larger than that required for the formation of the theoretical maximum composition ($Li_{4.4}Si$) with the 100 nm-thick Si.

2.2 Characterization

2.2.1 Electrochemical measurements

2.2.1-1 Galvanostatic lithiation/delithiation analysis

The electrochemical lithiation/delithiation were carried out in the analysis chamber under the vacuum condition about 5×10^{-9} Torr. The sample holder in the chamber and a potentio-galvanostat (Bio-Logic SP-200, VSP-300) at the outside were connected by coaxial cables via vacuum feed through. The cell voltage, i.e., potential difference between Si as a working electrode and Li as a counter electrode, was monitored under constant current conditions. The cutoff potential was set to be 0.01 and 1.2 V (*vs.* Li^+/Li). The constant current was described in C-rates in this thesis. A 1C is defined as the current value for the lithiation process to reach full theoretical capacity, 4,200 mAh g^{-1}, in 1 hour, i.e., 4.2 A/g. The specific capacity is normalized by mass of deposited Si, which is calculated from the thickness (ca. 100 nm, see Section 2.3.2), deposition area (ϕ8 or 9 mm), and volumetric density of Si crystal (2.33 g/cm^3).

2.2.1-2 Differential capacity curves

After the lithiatiation/delithiation curves were smoothed by averaging, the capacity curves were differentiated by the corresponding potential to yield the differential capacity (d*Q*/d*V*) curves.

2.3 Surface analysis

2.3.1 Atomic force microscopy

The surface roughness of Si electrode on a LLZT solid electrode sheet was measured by AFM (BRUKER Multi Mode 8) in the Ar-filled glove box in the identical analysis area (projected area) to that of XPS.

The changes of the thickness and nanoscale mechanical properties of the Si thin-film electrode during the initial lithiation were monitored using *in-situ* AFM. The height change of the thin-film cell was tracked by monitoring the voltage for the z-position of the piezo scanner, V_z, as shown in Figure 2 - 2 (a).

In order to determine the correlation between the V_z and the height changes, a Au/SiN grid with an ordered pattern (Figures 2 - 2 (b) and (c)) was measured. From the height difference of the pattern (123 nm) and the corresponding V_z change (–7.99 V), the height-voltage response, –15.4 nm/V, was obtained (Figures 2 - 2 (d) and (e)).

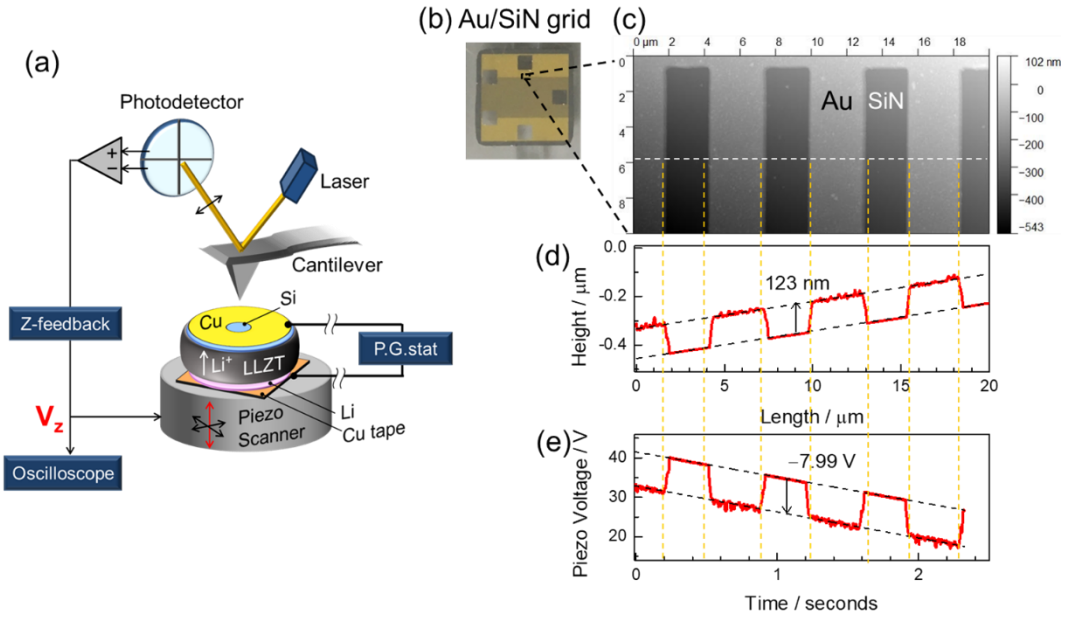

Figure 2 - 2. (a) Configuration for monitoring changes in thickness of amorphous-Si thin-film electrode by *in-situ* AFM. Z-axis feedback voltage to the piezoelectric scanner (V_z) was imported by an oscilloscope. (b)–(e) AFM measurement of a reference Au/SiN grid to clarify the piezo voltage-height response required for *in-situ* AFM (a); (b) Photograph of a Au/SiN grid, (c) AFM image with the scan rate 0.2 Hz, (d) height profile and (e) piezo voltage along the white line in (c).

2.3.2 X-ray diffraction and reflectometry

The crystallinity and thickness of deposited Si layer on a SUS substrate was characterized by using glazing incidence x-ray diffraction (GIXRD) and x-ray reflectometry (XRR), respectively. It is noted that LLZT substrate shows very strong diffraction peaks which make the structural analysis of Si thin film difficult. Thus, the Si thin film on SUS substrate was used for the GIXRD and XRR instead of LLZT. First, a SUS substate was polished by 800-grit sand papers and annealed in vacuum (~10^{-5} Pa) at 800 °C. The Si layer was deposited on the SUS substrate for the same time duration as that for making a Si/LLZT/Li structure. Both measurements were performed by using

SmartLab system (Rigaku) with Cu Kα radiation ($h\nu$=8,048 eV) and a specialized sample holder to prevent the sample from exposure to open air. In GIXRD measurements, the grazing angle of the incident x-rays was set to be 0.25° respect to the sample surface.

Figures 2 – 3 (a) and (b) show the GIXRD and XRR data of the Si layer deposited on the SUS substrate, respectively. The broad peaks around 2θ = 30° and 53° in GIXRD patterns (Figure 2 - 3 (a)) correspond to amorphous phase of the Si layer. Figure 2 - 3 (b) shows a typical XRR data of the amorphous Si layer deposited on the SUS substrate. According to the analysis of the periodic oscillation after the Fourier transform, the thickness of the Si layer was estimated to be 94.95 nm.

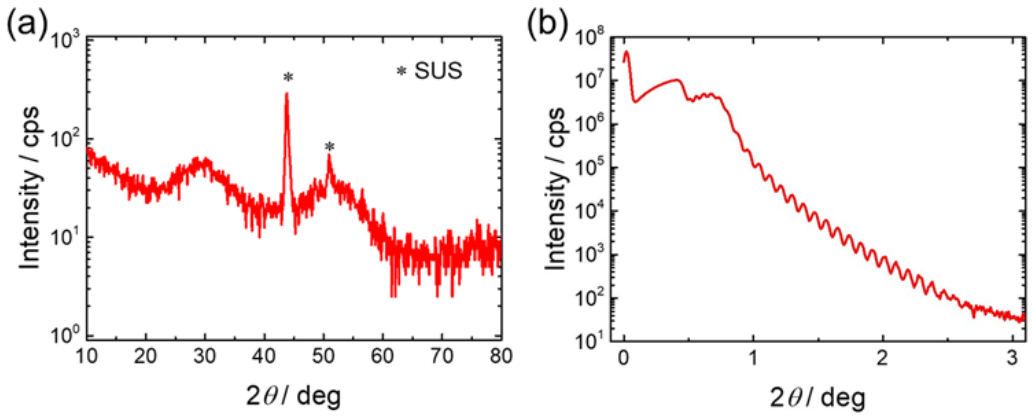

Figure 2 - 3. (a) Grazing incidence x-ray diffraction (GIXRD) patterns and (b) X-ray reflectometry (XRR) data of the amorphous Si layer on the SUS substrate.

2.3.3 X-ray photoelectron spectroscopy

X-ray photoelectron spectroscopy (XPS) was performed using AXIS NOVA (Shimadzu Kratos). This small section describes the principles, demonstration of depth analysis, development of an *in-situ* electrochemical XPS system, and data analysis.

2.3.3-1 Quantitative aspect and information depth

In XPS, samples are irradiated with x-rays, typically Al Kα, Mg Kα, and Ag Lα in laboratory available, and photoelectrons with various kinetic energy ejected from core levels are analyzed. The photoelectric effect can be represented by the following equation.

$$E_k = h\nu - E_b - \Phi, \qquad (2 - 1)$$

where E_k is the kinetic energy of emitted photoelectrons, $h\nu$ is the energy of incident x-rays, E_b is the binding energy of electrons at core levels, Φ is the work function of the sample of interest. The kinetic energy of photoelectrons, relative to the Fermi level of a sample, $E_k' = E_k + \Phi$, is measured by a hemispherical electron energy analyzer, and the population of photoelectrons is obtained with respect to E_b. The E_b is characteristic to core levels of chemical species and very sensitive to the chemical environment. Therefore, XPS enables us to analyze elemental composition, oxidation states (chemical bonding states), and electronic structure of a sample surface.

2.3.3-1.1 Photoelectron peak intensity

Peak intensity of photoelectrons from a material, x, is described by the equation (2 - 2).[6] Here, it is assumed that the effect of elastic scattering of photoelectrons on the peak intensity is negligible.

$$I_x = \frac{\Delta\Omega}{4\pi}\int_0^\infty I_0\sigma_x N_x W(\theta,\alpha)\exp\left[-\frac{z}{\lambda\cos\theta}\right]dz, \qquad (2 - 2)$$

where z is the depth from the sample surface, $\Delta\Omega$ is an acceptance angle of analyzer, I_0 is the intensity of incidence x-rays, σ_x is the ionization cross section of photoelectrons,[7] θ is the emission angle of photoelectrons, α is the angle between the

direction of incident x-rays and analyzer, $W(\theta, \alpha)$ is the angular asymmetry factor, N_x is the atom density, λ is the inelastic mean free paths (IMFPs) of the emitted photoelectrons in a matrix.[8-9] When the geometric arrangement of the detection system is identical, the equation can be expressed by the equation (2 - 3), using the detection efficiency of the photoelectrons emitted from the sample surface, $K = \frac{\Delta\Omega}{4\pi} W(\theta, \alpha)$.

$$I_x = K I_0 \sigma_x N_x \int_0^\infty \exp\left[-\frac{z}{\lambda \cos\theta}\right] dz, \qquad (2 - 3)$$

This equation indicates that the thickness of *x* can be determined using physical parameters and the peak intensity from each layer. In Chapters 4 and 5, the thickness of surface layers was estimated using the equation (2 - 3).

2.3.3-1.2 TPP-2M equation

To estimate the thickness of surface layers using equation (2 - 3), the IMFPs (λ) were obtained using TPP-2M formula proposed by Tanuma et al.[8-9] The TPP-2M equation is described as

$$\lambda = \frac{E}{E_p^2[\beta \ln(\gamma E) - (C/E) + (D/E^2)]}, \qquad (2 - 4)$$

$$\beta = -0.10 + 0.944\left(E_p^2 + E_g^2\right)^{-1/2} + 0.069\rho^{0.1}, \qquad (2 - 5)$$

$$\gamma = 0.191\rho^{-1/2}, \qquad (2 - 6)$$

$$C = 1.97 - 0.91U, \qquad (2 - 7)$$

$$D = 53.41 - 20.8U, \qquad (2 - 8)$$

$$U = N_v \rho / M = E_p^2 / 829.4, \qquad (2 - 9)$$

where E is the kinetic energy of emitted photoelectrons, E_p and E_g is the free-electron plasmon energy and the bandgap energy, N_v is the number of valence electrons per atom or molecule, ρ is the weight density, M is the atomic or molecular

weight.[9]

The information depth of XPS (defined as ~3λ) is calculated to be ~10 nm when the commonly used Al Kα (*hv*=1,486.7 eV) is employed as an incident x-ray source.[8-10] Thus, XPS is generally a surface sensitive technique with an information depth of about 3–10 nm. However, one can analyze the depth profile of chemical composition by tuning the energy of incident x-rays or takeoff angles (TOAs) of photoelectrons.

The use of incident x-rays with higher energy provides a larger probing depth because of the increase in the kinetic energy of photoelectrons and IMFPs. For example, the IMFPs of Si 2*p* photoelectrons in crystalline Si are estimated to be 3.09 and 5.60 nm when using the Al Kα (*hv*=1,486.7 eV) and the Ag Lα (*hv*=2,984.3 eV) x-rays, respectively.[8-9]

Angle-resolved XPS (ARXPS) is another useful technique for analyzing depth profile of electronic structure and chemical species at the surface vicinity. In ARXPS, photoelectron spectra with different surface sensitivity were obtained by changing the TOAs of photoelectrons. Figures 2 - 4 (a) and (b) show the configuration of ARXPS at the TOA of 90° and 15°, respectively. The configuration with small TOAs provides more surface-sensitive spectra, as shown in Figure 2 - 4 (b).

Figures 2 - 4 (c) and (d) show the example of ARXPS for two types of Mg-doped *p*-type GaN (*p*-GaN) films.[11] One is a *p*-GaN film with the thickness of 1 μm deposited on a GaN/sapphire substrate by metal organic chemical vapor deposition (MOCVD), denoted as "*p*-GaN-on-GaN/sapphire". The other is a *p*-GaN film deposited on a GaN substrate under the same condition, denoted as "*p*-GaN-on-GaN". In Figures 2 - 4 (c) and (d), the deconvoluted peaks at the lower binding energy at 18.4 eV and higher binding energy at 19.5 eV are corresponding to Ga-N and Ga-O related species,

respectively. In both samples, the Ga-O component was increased with decreasing the TOAs, indicating that the Ga-O related species were localized at the surface. As compared to *p*-GaN-on-GaN/sapphire (Figure 2 - 4 (c)), the formation of Ga-O species was suppressed at the surface of *p*-GaN-on-GaN sample (Figure 2 - 4 (d)). Formation of Ga-O species induces the instability of threshold voltage when *p*-GaN is used for metal-oxide-semiconductor field-effect transistors (MOSFETs). Thus, the depth-resolved XPS contributes to the quality control of electric devices.[11-12]

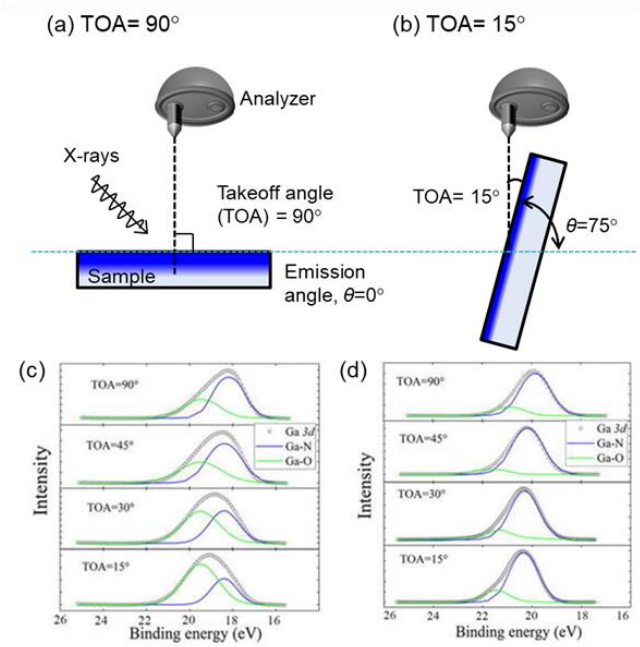

Figure 2 - 4. Configuration of angle-resolved XPS at takeoff angle of (a) 90° and (b) 15°. The blue shadow represents the information depth of XPS. Ga 3*d* photoelectron spectra for the (c) *p*-GaN-on-GaN/sapphire and (d) *p*-GaN-on-GaN samples obtained at different takeoff angles.[11]

Although Ar^+ ion sputtering is another option for analyzing depth profile of chemical species, uncertainty due to ion irradiation damage, surface reconstructions, and inhomogeneity derived from different sputtering rate among elements have been regarded as a problem.[13-14]

2.3.3-2 *In-situ* electrochemical XPS system

XPS is a powerful technique for analysing the chemical composition, oxidation states, and electronic structure of sample surfaces, as described above. In addition, XPS allows the acquisition of photoelectron signals from most elements without tuning photon energy of incident x-rays. If it can be applied to a certain position of the same electrochemical device under operation, the reaction process can be tracked in a stepwise manner without any influence of variation and inhomogeneity of samples.[15,16]

In-situ electrochemical XPS has been reported only for limited cases such as semiconductors,[17-19] electrocatalysts,[20-21] solid oxide fuel cells,[16, 22-24] and all-solid-state batteries.[25-37] For example, application of such *in-situ* electrochemical XPS to battery samples further offers a way not only to promote a proper assignment of each spectral feature to reaction products but also to correlate the effect of reaction products on the reversibility of charge/discharge reactions.[28,33]

To establish such advanced measurements and ensure their reliability, the development of specialized apparatus and sample holders has always been a prerequisite. For example, Whaley *et al.* developed an *in-situ* sample holder equipped with a resistive heater and three spring-loaded probes to heat and apply bias to an electrochemical device with a solid-oxide electrolyte, and used it for near ambient pressure XPS.[38] In addition, Wu *et al*. fabricated an *in-situ* sample holder capable of maintaining a high mechanical pressure to a bulk-type battery and used it to investigate the electrochemical reactions at the electrode/electrolyte interface, which is often responsible for ion transport during battery operation.[30, 34]

In the following section, we describe a developed series of *in-situ* XPS systems, including the appropriate apparatus, a specialized sample holder, a sample stage, and a transfer vessel, for tracking the successive electrochemical reactions of batteries.[39]

2.3.3-2.1 Specification of XPS apparatus

The bias application system and transfer vessel for *in-situ* XPS measuirements were designed to be compatible with a laboratory-based XPS instrument (AXIS NOVA, SHIMADZU Kratos).[39] Figure 2 - 5 shows a schematic illustration of the XPS apparatus composed of the sample entry chamber (SEC, A) and the sample analysis chamber (SAC, B). In a regular approach for transferring samples, the SEC (A) is pumped out after the sample stage is placed in the chamber under atmospheric conditions. A movable gripper comes from the SAC (B), and then, holds and transfers the sample stage to the analysis position. The XPS measurements are performed using a monochromatic Al Kα or Ag Lα source as incident x-rays (using C and D), magnetic (E) and electrostatic lenses (F), a hemispherical electron energy analyzer (G), and a delay-line detector (H). The gripper holds the sample stage for the duration of the XPS measurements. The angle of the incident x-rays to the sample surface is 35.5°. The aperture of the analyzer is located on the normal to the sample surface. The analysis area can be selected in several stages from ~180 μm^2 (circle with a diameter of 15 μm) to 210,000 μm^2 (rectangle of 700 μm × 300 μm) by tuning the magnetic lens (E), electrostatic lenses (F), angle defining iris, and aperture diameter of the analyzer. The solid angle for the collection of photoelectrons is approximately ±20°. The use of a magnetic lens (E) with a highly defined focus reduces the spherical aberration, resulting in high magnification and high spatial resolution on the order of micrometers. The

combination with the SAC camera (J) enables us to analyze a minute region of a size on the order of tens of micrometers.

The photon energy of Ag Lα x-rays (*hv*=2,984.3 eV) is higher than that of Al Kα x-rays (*hv*=1,486.7 eV), which means that the former can extract photoelectrons with higher energy from a core level and enable us to analyze the deeper position of the sample. This is an advantage for analyzing bulky samples including batteries.

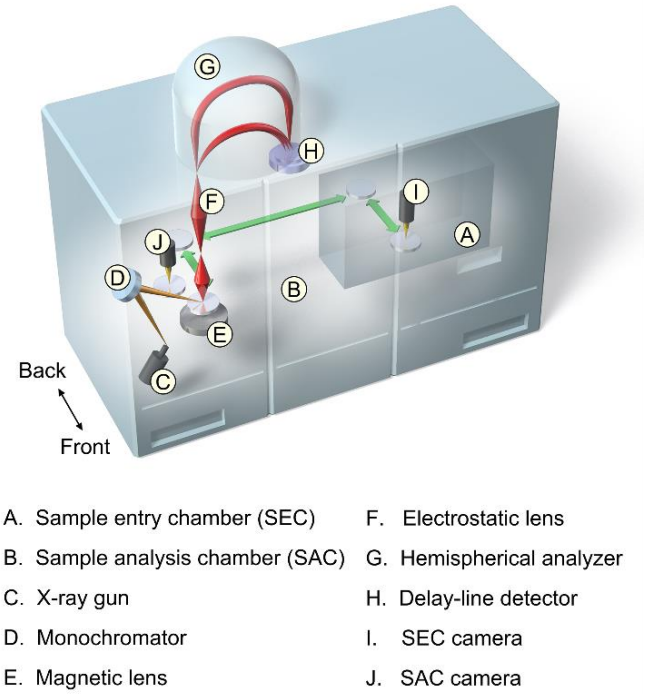

A. Sample entry chamber (SEC)
B. Sample analysis chamber (SAC)
C. X-ray gun
D. Monochromator
E. Magnetic lens
F. Electrostatic lens
G. Hemispherical analyzer
H. Delay-line detector
I. SEC camera
J. SAC camera

Figure 2 - 5. A schematic illustration of the XPS apparatus setup (AXIS NOVA, Shimadzu Kratos). The apparatus is composed of the sample entry chamber (SEC, A) and the sample analysis chamber (SAC, B).

2.3.3-2.2 Bias application system

Figures 2 - 6 (a)–(c) show the custom-made sample holder, the gripper holding the sample stage, and the electrical wiring in the XPS apparatus, respectively. Three electrical terminals are mounted on the sample holder, the sample stage, and the gripper. The phosphor bronze plates, which act as electrical terminals, are fixed on the sample

holder by ceramics screws. When the sample holder (Figure 2 - 6 (a)) is inserted into the groove of the sample stage, as shown in Figure 2 - 6 (b), terminals A–C of the sample holder are electrically connected to those of the sample stage. In addition, the terminals of the sample stage and gripper are connected through Kapton-coated copper wires and three copper rods when the gripper holds the sample stage and pushes the copper rods. Each terminal of the gripper is attached to an electrical wire (Figure 2 - 6 (b)) composed of silver-plated copper with a size of 24AWG. The wires were further coated with fluoro-ethylenepropylene (FEP) to prevent short circuits. The electrical wires were connected to the external coaxial cables and a potentio-galvanostat from the outside via a vacuum feed-through (Figure 2 - 6 (c)). The length of the electrical wire for each channel in the apparatus is approximately 3 m. Three independent electrical contacts were therefore established among the potentio-galvanostat, the gripper, the sample stage, and the sample holder, allowing *in-situ* XPS measurements of the sample in the analysis chamber to be carried out.

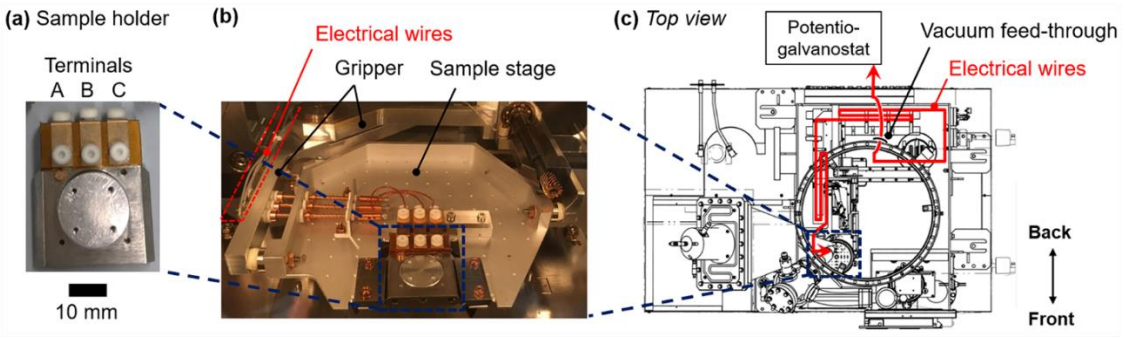

Figure 2 - 6. Photographic images of (a) the sample holder, and (b) the gripper holding the sample stage with the sample holder. (c) A schematic representation of the top view of the XPS apparatus with electrical wires for bias application.

2.3.3-2.3 Transfer vessel for air-sensitive samples

Figure 2 - 7 (a) shows the transfer vessel enabling the transfer of air-sensitive samples without exposure to open air. The transfer vessel contains a rod with a magnetic coupling to mount the sample holder with a screw and a gate valve to seal the sample holder inside. The inside of the vessel has a cylindrical shape with an inner diameter of ca. 40 mm and a length of ca. 150 mm. The sides of the transfer vessel are attached to a compound pressure gauge, a bellows seal valve (Swagelok, SS-4H), and a KF-16 flange, for gas inlet and outlet. The end of the transfer vessel is a KF-40 flange connected to a glove box filled with Ar gas and the sample entry chamber (SEC) of the XPS apparatus, as shown in Figure 2 - 7 (b).

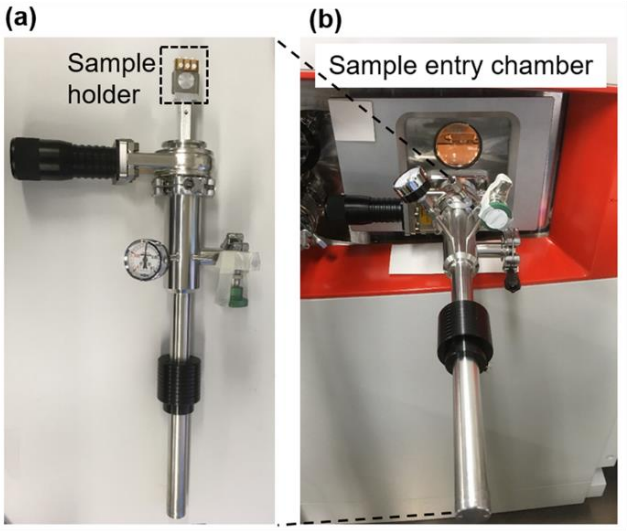

Figure 2 - 7. Photographic images of the transfer vessel (a) equipped with the sample holder, and (b) connected to the sample entry chamber (SEC) of the XPS apparatus.

The procedure for sample transfer using the vessel is as follows. Initially, a sample is placed on the sample holder in an Ar-filled glove box, and then the holder is fixed to the transfer rod of the vessel. After the sample holder is sealed by closing the gate valve, the

vessel is disconnected from the glove box and connected to the SEC of the XPS apparatus. Subsequently, the sample holder is inserted into the groove of the sample stage in the SEC under inert gas or vacuum conditions. Finally, the sample stage with the holder is transferred to the analysis position in the SAC by regular operation using the gripper as described above.

2.3.3-2.4 Operation test

Following their development, the application of a direct current (DC) voltage was confirmed by the photoelectron peak shift of the Au samples. Two pieces of Au foil (99.95%, Nilaco Co. Ltd., Japan) were placed in the sample holder in two circuits, as shown in Figures 2 - 8 (a) and (b). In the first circuit shown in Figure 2 - 8 (a), one Au foil was directly placed on a terminal of the sample holder and grounded to the sample holder and the hemispherical analyzer. This Au foil was used as the counter electrode (CE). The other Au foil, a working electrode (WE), was connected to another terminal but insulated (isolated) from the sample holder and the analyzer using a polyimide film. This circuit was denoted as “CE grounded”.[30] In the second circuit shown in Figure 2 - 8 (b), the roles of the WE and CE were switched; i.e., the Au foil grounded to the analyzer was used as a WE, and the isolated Au foil was used as a CE. This circuit was denoted as “WE grounded”.[30] The bias application was carried out in each circuit using a potentio-galvanostat (Bio-Logic VSP-300). XPS measurements were performed under a pressure of ~5×10^{-8} Torr, while external DC biases of −5, −2, 0, +2, and +5 V were applied to the WE *vs*. CE. A monochromatic Al Kα (1,486.7 eV) source at a power of 75 W was used as the incident X-ray source. The analysis area, takeoff angle, and pass energy of the photoelectrons were fixed at 700 μm × 300 μm, 90°, and 40 eV, respectively.

Figure 2 - 8 (c) shows the Au 4*f* photoelectron peaks from the Au foil in the circuit of the CE grounded (Figure 2 - 8 (a)). A doublet peak corresponding to Au $4f_{7/2}$ and $4f_{5/2}$ was observed for the Au foils, which were used as the WE and the CE. The Au 4*f* peaks from the grounded Au foil as a CE were identical under bias conditions (Figure 2 - 8 (c), lower plot). In contrast to the grounded CE, the peaks from the other Au foil as a WE were shifted by the applied bias (Figure 2 - 8 (c), upper plot). A larger applied bias causes a peak shift to higher binding energy. The correlation between the shift direction and the applied bias is in agreement with that reported in previous works.[17, 40] It was therefore demonstrated that the DC voltage was successfully applied to the sample holder in the analysis chamber.

We performed the same measurement in the other circuit to clarify the correlation between the applied bias and the direction of the peak shift. Figure 2 - 8 (d) shows the Au 4*f* photoelectron peaks obtained in the circuit of the WE grounded (Figure 2 - 8 (b)). The Au 4*f* peaks, where the grounded Au foil was used as a WE, were identical, independent of the applied bias (Figure 2 - 8 (d), upper plot). In contrast, those from the case where the Au foil was used as a CE, which was insulated from the analyzer, showed a shift corresponding to the applied bias (Figure 2 - 8 (d), lower plot). Overall, a larger bias voltage was found to cause a peak shift to lower binding energy.

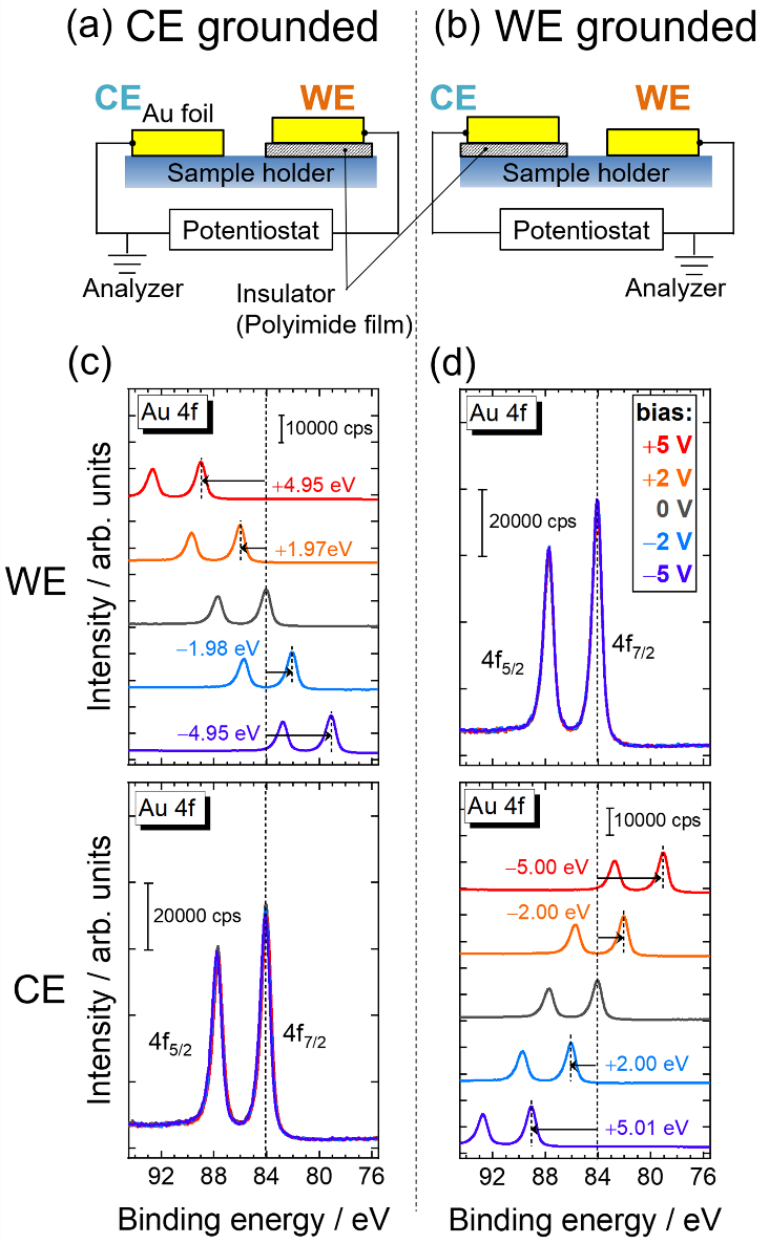

Figure 2 - 8. Simplified schematic representations of the two electrical circuits for confirming the application of direct current (DC) voltage to the sample holder: (a) the counter electrode (CE) or (b) working electrode (WE) grounded to the analyzer. (c)–(d) Au 4*f* photoelectron peaks under bias conditions in each circuit. The dashed lines in the graphs indicate the binding energies of the Au 4$f_{7/2}$ peaks, determined by curve fitting using the Voigt function after Shirley background subtraction.

Figure 2 - 9 summarizes the correlation between the applied bias and the direction of the Au 4*f* peak shift when the CE or WE was grounded to the analyzer.[30] In both circuits, Au 4*f* peaks from the Au foils insulated (isolated) from the analyzer showed a shift corresponding to the applied bias voltage, while those from the grounded Au foils were identical. Although the direction of the peak shift from the isolated Au foils with respect to a certain bias was opposite in the two circuits, the relationship of their energy levels was preserved. For example, when a positive bias was applied to the WE, the Fermi energy of the CE remained higher than that of the WE in both circuits, as shown in Figure 2 - 9. It was therefore confirmed that a positive or negative bias was properly applied to the sample in the analysis chamber.

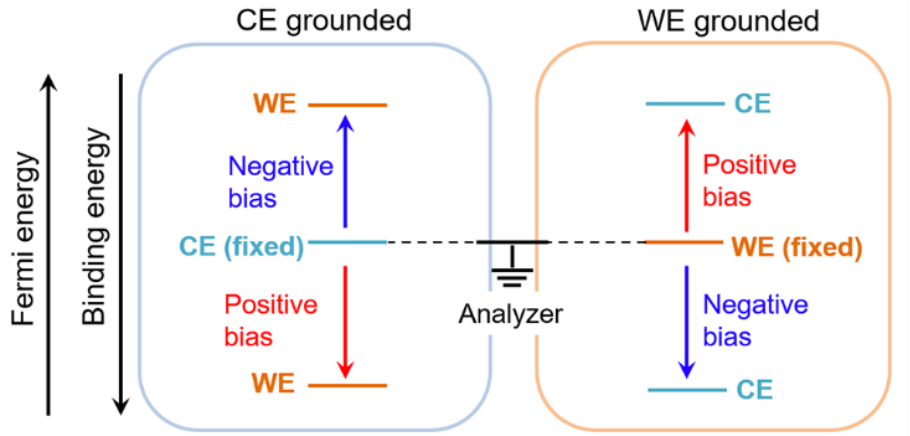

Figure 2 - 9. The correlation between the applied bias and the direction of the Au 4*f* peak shift when the (a) CE or (b) WE was grounded to the analyzer.

Our research group previously demonstrated *in-situ* electrochemical XPS of solid/liquid interfaces using hard x-rays at a synchrotron radiation facility in 2012.[41] Subsequently, chemical species in the liquid were observed using a laboratory XPS apparatus equipped with a conventional Al Kα source, as mentioned above.[42] It is anticipated that the combination of these techniques will allow the *in-situ* XPS

observation of electrochemical and electrocatalytic reactions at solid/liquid interfaces.[43-46]

In summary, we developed an *in-situ* electrochemical X-ray photoelectron spectroscopy (XPS) system capable of bias application to an electrochemical device in the analysis chamber under vacuum conditions, and a transfer vessel for transferring air-sensitive samples without exposure to open air. The application of a direct current voltage to the specialized sample holder in the analysis chamber was confirmed from the Au 4*f* peak shifts of the Au foil.

In the following XPS measurements in this study, the copper current collector in contact with Si layer of a thin-film cell was electrically connected to the sample holder and analyzer, i.e., “WE grounded” circuit, to assign photoelectron peaks based on chemical shifts due to changes of chemical bonding states, not on the potential gradient due to applied bias.

2.3.3-3 Configuration of *in-situ* electrochemical XPS

The Li layer of the thin-film cell with a structure of Li/LLZT/Si/Cu was bound to the copper foil, the thin-film cell was loaded on a sample holder (Figure 2 - 10 (a)), as shown in Figure 2 - 11 in an Ar-filled glove box. The bottom side (Li side) was electrically isolated from the sample holder by a polyimide film and connected to the terminal A. The top side (Si side) was connected to the sample holder and the terminal B. Then, the cell-loaded sample holder was sealed in a vacuum suitcase (Figures 2 - 10 (b) and (c)), and transferred into the XPS apparatus (AXIS NOVA, Shimadzu Kratos) without exposing to open air by attaching the vacuum suitcase to the load lock (Figure 2 - 10 (d)). Once the sample holder was mounted on the stage in the analysis chamber by

a regular transfer operation (Figure 2 - 10 (e)), the terminal B, as well as the sample holder, was electrically grounded with the hemispherical analyzer of XPS apparatus. Since the terminals A and B are connected to the external coaxial cables via vacuum feed through, bias can be applied to the terminals A and B at the outside by using a potentio-galvanostat (Bio-Logic SP-200, VSP-300).

The XPS measurements were performed in the analysis chamber under the vacuum condition about 5×10^{-9} Torr. Upon the repeated electrochemical processes, exactly the same spot of the Si electrode was measured by XPS under the open-circuit condition and during lithiation/delithiation processes. A monochromatic Al Kα ($h\nu$=1,486.7 eV) source operated at 300 W was used as an incident X-ray. The takeoff angle and pass energy of photoelectrons were fixed at 90° and 80 eV, respectively.

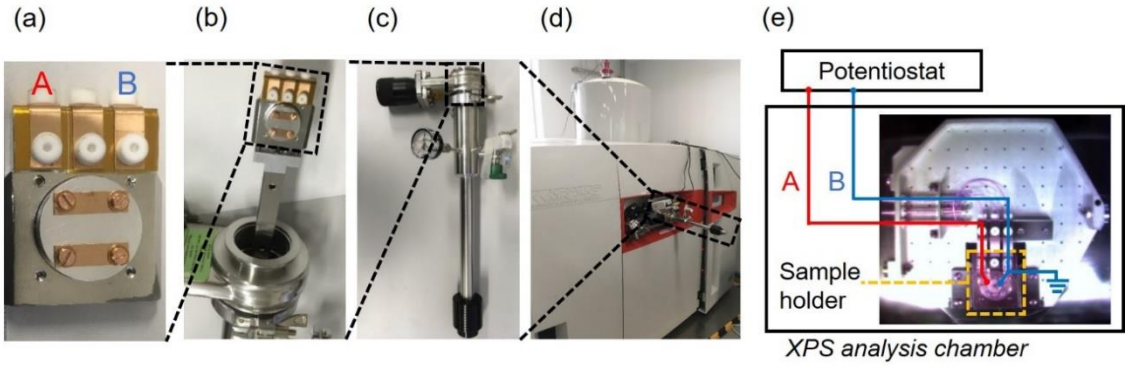

Figure 2 - 10. Photographs of (a) the sample holder and (b)–(c) the vacuum suitcase for transferring samples without air exposure. (d) Laboratory-type XPS apparatus. (e) The simplified schematics of the analysis chamber, electrical connections, and the stage with the sample holder. The terminals A and B were connected to the potentiostat via vacuum feed through and external coaxial cables.

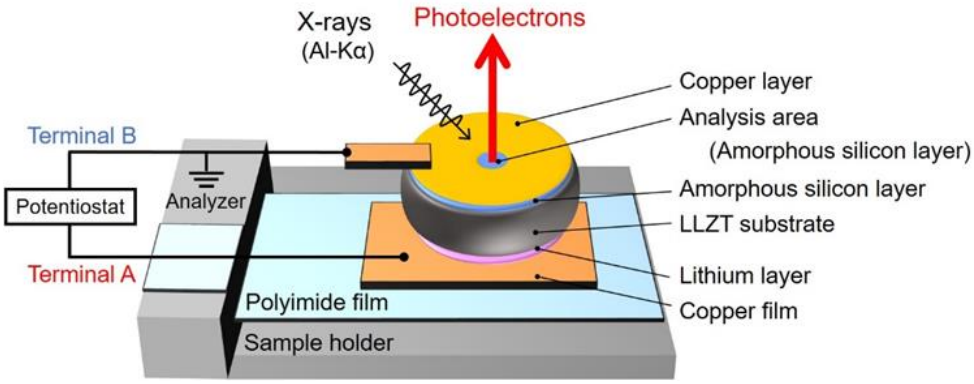

Figure 2 - 11. Schematic illustration of the amorphous Si/LLZT/Li metal cell and the configuration of *in-situ* electrochemical XPS measurements.

2.3.3-4 Data analysis

Obtained photoelectron spectra were fitted by Voigt functions using IGOR Pro software (WaveMetrics, Inc.) to analyze the peak positions and the integrated peak area.

2.3.3-4.1 Background subtraction

In XPS spectra, the major reason for the background formation is the repeated inelastic-scattering of photoelectrons ejected from core levels. Prior to the curve fitting described below, the background related to the scattered photoelectrons from core levels was subtracted from the original spectra. In the present study, the Shirley approach[47] was adopted for background subtractions. In the Shirley approach, background curve is determined based on the assumption that the number of inelastic-scattered photoelectrons and the background intensity is proportional to the intensity of core-level peaks. The Shirley approach is less accurate than the Tougaad approach[48] due to not taking into account the energy dependence, however, the former is sufficient for a narrow range of spectra and a short acquisition time unlike the latter. This advantage related to the acquisition time can be beneficial to *in-situ* measurements where reactions are in progress.

2.3.3-4.2 Curve fitting

After the Shirley background subtraction, curve fittings were performed by Voigt function defined as the convolutional integration of Gaussian and Lorentzian. The Gaussian represents the totalization of broadening processes such as line shape of x-rays, the electron energy analyzer, and phonon broadening. The Lorentzian represents natural line shape with consideration of core-hole lifetime.[49]

2.3.3-4.3 Binding energy calibration

The binding energy is usually referenced to the Fermi level of the electron energy analyzer. When conductive samples such as metals are set on a sample holder, the Fermi level of the samples is identical to the Fermi level of the analyzer. However, in case of low conductivity and insulating samples such as polymers and semiconductors, the Fermi level does not align with that of the analyzer due to the charging effect. Therefore, the correction of the binding energy is necessary for accurate peak assignment. The hydrocarbon peak in C 1*s* energy region from contaminating carbon species (which are present in a vacuum chamber) is commonly used for the reference of the charge collection.[50] This process is based on the assumption that the contaminating carbon is located on the sample surface close to the probing depth of the XPS measurements, and the Fermi level of the contaminating carbon corresponds to that of the sample surface. In the present study, the hydrocarbon peak in C 1*s* energy region was fixed at 285.0 eV for the calibration of binding energy when measuring low conductive samples.

References

1. Feng, K.; Li, M.; Liu, W.; Kashkooli, A. G.; Xiao, X.; Cai, M.; Chen, Z., Silicon-Based Anodes for Lithium-Ion Batteries: From Fundamentals to Practical Applications. *Small* **2018,** *14* (8), 1702737.
2. Murugan, R.; Thangadurai, V.; Weppner, W., Fast lithium ion conduction in garnet-type

$Li_7La_3Zr_2O_{12}$. *Angew. Chem. Int. Ed. Engl.* **2007,** *46* (41), 7778-81.

3. Wang, C.; Fu, K.; Kammampata, S. P.; McOwen, D. W.; Samson, A. J.; Zhang, L.; Hitz, G. T.; Nolan, A. M.; Wachsman, E. D.; Mo, Y.; Thangadurai, V.; Hu, L., Garnet-Type Solid-State Electrolytes: Materials, Interfaces, and Batteries. *Chem. Rev.* **2020,** *120* (10), 4257-4300.
4. Ferraresi, G.; El Kazzi, M.; Czornomaz, L.; Tsai, C.-L.; Uhlenbruck, S.; Villevieille, C., Electrochemical performance of all-solid-state Li-ion batteries based on garnet electrolyte using silicon as a model electrode. *ACS Energy Lett.* **2018,** *3* (4), 1006-1012.
5. Haruta, M.; Doi, T.; Inaba, M., Oxygen-Content Dependence of Cycle Performance and Morphology Changes in Amorphous-SiO_x Thin-Film Negative Electrodes for Lithium-Ion Batteries. *J. Electrochem. Soc.* **2019,** *166* (2), A258-A263.
6. Hofmann, S., *Auger- and X-Ray Photoelectron Spectroscopy in Materials Science*. 2013; Vol. 49.
7. Yeh, J. J.; Lindau, I., Atomic subshell photoionization cross sections and asymmetry parameters: $1 \leqslant Z \leqslant 103$. *At. Data Nucl. Data Tables* **1985,** *32* (1), 1-155.
8. Tanuma, S.; Powell, C. J.; Penn, D. R., Calculations of electron inelastic mean free paths. III. Data for 15 inorganic compounds over the 50–2000 eV range. *Surf. Interface Anal.* **1991,** *17* (13), 927-939.
9. Tanuma, S.; Powell, C. J.; Penn, D. R., Calculation of electron inelastic mean free paths (IMFPs) VII. Reliability of the TPP-2M IMFP predictive equation. *Surf. Interface Anal.* **2003,** *35* (3), 268-275.
10. Tanuma, S.; Powell, C. J.; Penn, D. R., Calculations of electron inelastic mean free paths. IX. Data for 41 elemental solids over the 50 eV to 30 keV range. *Surf. Interface Anal.* **2011,** *43* (3), 689-713.
11. Sang, L.; Ren, B.; Endo, R.; Masuda, T.; Yasufuku, H.; Liao, M.; Nabatame, T.; Sumiya, M.; Koide, Y., Boosting the doping efficiency of Mg in p-GaN grown on the free-standing GaN substrates. *Appl. Phys. Lett.* **2019,** *115* (17), 172103.
12. Zhang, K.; Liao, M.; Imura, M.; Nabatame, T.; Ohi, A.; Sumiya, M.; Koide, Y.; Sang, L., Electrical hysteresis in p-GaN metal–oxide–semiconductor capacitor with atomic-layer-deposited Al_2O_3 as gate dielectric. *Applied Physics Express* **2016,** *9* (12), 121002.
13. Lewin, E.; Gorgoi, M.; Schäfers, F.; Svensson, S.; Jansson, U., Influence of sputter damage on the XPS analysis of metastable nanocomposite coatings. *Surf. Coat. Technol.* **2009,** *204* (4), 455-462.
14. Steinberger, R.; Walter, J.; Greunz, T.; Duchoslav, J.; Arndt, M.; Molodtsov, S.; Meyer, D. C.; Stifter, D., XPS study of the effects of long-term Ar^+ ion and Ar cluster sputtering on the chemical degradation of hydrozincite and iron oxide. *Corros. Sci.* **2015,** *99*, 66-75.
15. Casalongue, H. S.; Kaya, S.; Viswanathan, V.; Miller, D. J.; Friebel, D.; Hansen, H. A.; Norskov, J. K.; Nilsson, A.; Ogasawara, H., Direct observation of the oxygenated species during oxygen reduction on a platinum fuel cell cathode. *Nat. Commun.* **2013,** *4* (1), 2817.
16. Zhang, C.; Grass, M. E.; McDaniel, A. H.; DeCaluwe, S. C.; El Gabaly, F.; Liu, Z.; McCarty, K. F.; Farrow, R. L.; Linne, M. A.; Hussain, Z.; Jackson, G. S.; Bluhm, H.; Eichhorn, B. W., Measuring

fundamental properties in operating solid oxide electrochemical cells by using *in situ* X-ray photoelectron spectroscopy. *Nat. Mater.* **2010,** *9* (11), 944-9.

17. Ulgut, B.; Suzer, S., XPS studies of SiO_2/Si system under external bias. *J. Phys. Chem. B* **2003,** *107* (13), 2939-2943.
18. Ertas, G.; Suzer, S., XPS analysis with external bias: a simple method for probing differential charging. *Surf. Interface Anal.* **2004,** *36* (7), 619-623.
19. Yamashita, Y.; Ohmori, K.; Ueda, S.; Yoshikawa, H.; Chikyow, T.; Kobayashi, K., Bias-voltage application in hard X-tay photoelectron spectroscopy for characterization of advanced materials. *e-J. Surf. Sci. Nanotechnol.* **2010,** *8*, 81-83.
20. Favaro, M.; Drisdell, W. S.; Marcus, M. A.; Gregoire, J. M.; Crumlin, E. J.; Haber, J. A.; Yano, J., An operando investigation of (Ni–Fe–Co–Ce)O_x system as highly efficient electrocatalyst for oxygen evolution reaction. *ACS Catal.* **2017,** *7* (2), 1248-1258.
21. Favaro, M.; Yang, J.; Nappini, S.; Magnano, E.; Toma, F. M.; Crumlin, E. J.; Yano, J.; Sharp, I. D., Understanding the oxygen evolution reaction mechanism on CoO_x using operando ambient-pressure X-ray photoelectron spectroscopy. *J. Am. Chem. Soc.* **2017,** *139* (26), 8960-8970.
22. DeCaluwe, S. C.; Grass, M. E.; Zhang, C. J.; El Gabaly, F.; Bluhm, H.; Liu, Z.; Jackson, G. S.; McDaniel, A. H.; McCarty, K. F.; Farrow, R. L.; Linne, M. A.; Hussain, Z.; Eichhorn, B. W., In situ characterization of ceria oxidation states in high-temperature electrochemical cells with ambient pressure XPS. *J. Phys. Chem. C* **2010,** *114* (46), 19853-19861.
23. El Gabaly, F.; Grass, M.; McDaniel, A. H.; Farrow, R. L.; Linne, M. A.; Hussain, Z.; Bluhm, H.; Liu, Z.; McCarty, K. F., Measuring individual overpotentials in an operating solid-oxide electrochemical cell. *Phys. Chem. Chem. Phys.* **2010,** *12* (38), 12138-45.
24. Bozzini, B.; Amati, M.; Gregoratti, L.; Kiskinova, M., In-situ photoelectron microspectroscopy and imaging of electrochemical processes at the electrodes of a self-driven cell. *Sci. Rep.* **2013,** *3* (1), 2848.
25. Tonti, D.; Pettenkofer, C.; Jaegermann, W., *In situ* photoelectron spectroscopy study of a TiS_2 cathode in an operating battery system. *Electrochem. Solid-State Lett.* **2000,** *3* (5), 220-223.
26. Tonti, D.; Pettenkofer, C.; Jaegermann, W., Origin of the electrochemical potential in intercalation electrodes: experimental estimation of the electronic and ionic contributions for Na intercalated into TiS_2. *J. Phys. Chem. B* **2004,** *108* (41), 16093-16099.
27. Lu, Y. C.; Crumlin, E. J.; Veith, G. M.; Harding, J. R.; Mutoro, E.; Baggetto, L.; Dudney, N. J.; Liu, Z.; Shao-Horn, Y., *In situ* ambient pressure X-ray photoelectron spectroscopy studies of lithium-oxygen redox reactions. *Sci. Rep.* **2012,** *2*, 715.
28. Koerver, R.; Walther, F.; Aygun, I.; Sann, J.; Dietrich, C.; Zeier, W. G.; Janek, J., Redox-active cathode interphases in solid-state batteries. *J. Mater. Chem. A* **2017,** *5* (43), 22750-22760.
29. Guhl, C.; Kehne, P.; Ma, Q.; Tietz, F.; Alff, L.; Komissinskiy, P.; Jaegermann, W.; Hausbrand, R.,

In-operando photoelectron spectroscopy for batteries: set-up using pristine thin film cathode and first results on Na_xCoO_2. *Rev. Sci. Instrum.* **2018,** *89* (7), 073104.

30. Wu, X.; Villevieille, C.; Novak, P.; El Kazzi, M., Monitoring the chemical and electronic properties of electrolyte-electrode interfaces in all-solid-state batteries using operando X-ray photoelectron spectroscopy. *Phys. Chem. Chem. Phys.* **2018,** *20* (16), 11123-11129.
31. Akada, K.; Sudayama, T.; Asakura, D.; Kitaura, H.; Nagamura, N.; Horiba, K.; Oshima, M.; Hosono, E.; Harada, Y., *Operando* measurement of single crystalline $Li_4Ti_5O_{12}$ with octahedral-like morphology by microscopic X-ray photoelectron spectroscopy. *J. Electron. Spectrosc. Relat. Phenom.* **2019,** *233*, 64-68.
32. Akada, K.; Sudayama, T.; Asakura, D.; Kitaura, H.; Nagamura, N.; Horiba, K.; Oshima, M.; Hosono, E.; Harada, Y., Microscopic photoelectron analysis of single crystalline $LiCoO_2$ particles during the charge-discharge in an all solid-state lithium ion battery. *Sci. Rep.* **2019,** *9* (1), 12452.
33. Liu, Z.; Li, G. Z.; Borodin, A.; Liu, X. X.; Li, Y.; Endres, F., In situ X-ray photoelectron spectroscopy investigation of the solid electrolyte interphase in a $Li/Li_{6.4}Ga_{0.2}La_3Zr_2O_{12}/LiFePO_4$ all-solid-state battery. *J. Solid State Electrochem.* **2019,** *23* (7), 2107-2117.
34. Wu, X.; Villevieille, C.; Novak, P.; El Kazzi, M., Insights into the chemical and electronic interface evolution of $Li_4Ti_5O_{12}$ cycled in Li_2S-P_2S_5 enabled by operando X-ray photoelectron spectroscopy. *J. Mater. Chem. A* **2020,** *8* (10), 5138-5146.
35. Kiuchi, H.; Hikima, K.; Shimizu, K.; Kanno, R.; Fukunaga, T.; Matsubara, E., Operando hard X-ray photoelectron spectroscopy of $LiCoO_2$ thin film in an all-solid-state lithium ion battery. *Electrochem. Commun.* **2020,** *118*, 106790.
36. Endo, R.; Ohnishi, T.; Takada, K.; Masuda, T., *In situ* observation of lithiation and delithiation reactions of a silicon thin film electrode for all-solid-state lithium-ion batteries by X-ray photoelectron spectroscopy. *J. Phys. Chem. Lett.* **2020,** *11* (16), 6649-6654.
37. Tonti, D.; Pettenkofer, C.; Jaegermann, W., In-Situ Photoelectron Spectroscopy Study of a TiS_2 Thin Film Cathode in an Operating Na Intercalation Electrochemical Cell. *Ionics* **2000,** *6* (3-4), 196-202.
38. Whaley, J. A.; McDaniel, A. H.; El Gabaly, F.; Farrow, R. L.; Grass, M. E.; Hussain, Z.; Liu, Z.; Linne, M. A.; Bluhm, H.; McCarty, K. F., Note: fixture for characterizing electrochemical devices in-operando in traditional vacuum systems. *Rev. Sci. Instrum.* **2010,** *81* (8), 086104.
39. Endo, R.; Ohnishi, T.; Takada, K.; Masuda, T., Instrumentation for tracking electrochemical reactions by x-ray photoelectron spectroscopy under conventional vacuum conditions. *Journal of Physics Communications* **2021,** *5* (1), 015001.
40. Dickinson, T.; Povey, A. F.; Sherwood, P. M. A., Differential sample charging in ESCA. *J. Electron. Spectrosc. Relat. Phenom.* **1973,** *2* (4), 441-447.
41. Masuda, T.; Yoshikawa, H.; Noguchi, H.; Kawasaki, T.; Kobata, M.; Kobayashi, K.; Uosaki, K., *In situ* x-ray photoelectron spectroscopy for electrochemical reactions in ordinary solvents. *Appl. Phys.*

Lett. **2013,** *103* (11), 111605.

42. Endo, R.; Watanabe, D.; Shimomura, M.; Masuda, T., *In situ* X-ray photoelectron spectroscopy using a conventional Al-Kα source and an environmental cell for liquid samples and solid-liquid interfaces. *Appl. Phys. Lett.* **2019,** *114* (17), 173702.
43. Velasco-Vélez, J. J.; Pfeifer, V.; Havecker, M.; Weatherup, R. S.; Arrigo, R.; Chuang, C. H.; Stotz, E.; Weinberg, G.; Salmeron, M.; Schlogl, R.; Knop-Gericke, A., Photoelectron spectroscopy at the graphene-liquid interface reveals the electronic structure of an electrodeposited cobalt/graphene electrocatalyst. *Angew. Chem. Int. Ed. Engl.* **2015,** *54* (48), 14554-8.
44. Nemšák, S.; Strelcov, E.; Duchoň, T.; Guo, H.; Hackl, J.; Yulaev, A.; Vlassiouk, I.; Mueller, D. N.; Schneider, C. M.; Kolmakov, A., Interfacial electrochemistry in liquids probed with photoemission electron microscopy. *J. Am. Chem. Soc.* **2017,** *139* (50), 18138-18141.
45. Nemšák, S.; Strelcov, E.; Guo, H.; Hoskins, B. D.; Duchoň, T.; Mueller, D. N.; Yulaev, A.; Vlassiouk, I.; Tselev, A.; Schneider, C. M.; Kolmakov, A., In aqua electrochemistry probed by XPEEM: experimental setup, examples, and challenges. *Top. Catal.* **2018,** *61* (20), 2195-2206.
46. Masuda, T., Various spectroelectrochemical cells for in situ observation of electrochemical processes at solid-liquid interfaces. *Top. Catal.* **2018,** *61* (20), 2103-2113.
47. Shirley, D. A., High-Resolution X-Ray Photoemission Spectrum of the Valence Bands of Gold. *Physical Review B* **1972,** *5* (12), 4709-4714.
48. Tougaard, S., Low energy inelastic electron scattering properties of noble and transition metals. *Solid State Commun.* **1987,** *61* (9), 547-549.
49. Conny, J. M.; Powell, C. J., Standard test data for estimating peak parameter errors in x-ray photoelectron spectroscopy III. Errors with different curve-fitting approaches. *Surf. Interface Anal.* **2000,** *29* (12), 856-872.
50. Johansson, G.; Hedman, J.; Berndtsson, A.; Klasson, M.; Nilsson, R., Calibration of electron spectra. *J. Electron. Spectrosc. Relat. Phenom.* **1973,** *2* (3), 295-317.

Chapter 3. Solution species quantitatively observed using environmental cells and X-ray photoelectron spectroscopy

3.1 Introduction

Prior to the investigation of electrochemical reaction in relation to the all-solid-state batteries by the newly developed *in-situ* X-ray photoelectron spectroscopy (XPS), XPS observation of liquid samples encapsulated in an environmental cell was demonstrated for the future possible application of this system to the liquid-type batteries. [1]

Brief overview of XPS observation for liquid samples and solid/liquid interfaces

XPS, which can nondestructively analyze the composition, oxidation states, and chemical bonding of elements at a solid surface, is one of the indispensable techniques for current research and development. In XPS, since photoelectrons emitted by irradiation of x-rays are detected by an electron analyzer, a vacuum condition is essential to avoid significant intensity loss due to the scattering of photoelectrons in gas and liquid phases. However, tremendous efforts have been devoted to utilizing XPS for liquid samples[2-3] and solid/liquid interfaces.[4-6] Siegbahn *et al.* performed pioneering photoelectron spectroscopy measurements of liquid samples by using the technique called "liquid jet" in the 1970s[7-9] shortly after the development of XPS by himself. In this system, a flowing liquid column was generated by using a liquid nozzle placed in a vacuum chamber, and photoelectrons emitted at a surface of the liquid column were

detected by the differentially-pumped electron analyzer at a high vacuum (<2×10^{-5} Torr). This technique has been utilized for a wide variety of systems such as water,[10-11] organic solvents,[12] ionic species,[13] and nanoparticles in a liquid phase.[14-16]

Besides electrochemical-XPS systems equipped with an electrochemical cell and an electron analyzer,[17-21] a few innovative techniques for liquid samples and solid/liquid interfaces have been developed. One is the utilization of ionic liquids, whose vapor pressure is almost zero even in a vacuum. Electrochemical processes taking place at ionic liquid/electrode interfaces have been investigated by detecting photoelectrons emitted at surfaces of ionic liquids and electrodes.[22-24] Although these studies provide important information, physicochemical properties of ionic liquids are significantly different from those of water or organic solvents. Therefore, an alternative approach is required for such ordinary liquids.

In combination with a near ambient pressure (NAP-)XPS which can measure solid/liquid or solid/gas interfaces in a relatively low vacuum using a differential pumping system,[4, 25-29] a “dip and pull” method has been utilized for a thin liquid-layer-coated electrode surface partially pulled up from a liquid reservoir placed in an analysis chamber.[30-31] When the thickness of the liquid layer is very thin (~10 nm), not only the solution species but also the adsorbed species on and the oxidation state of electrode surfaces can be analyzed by detecting the photoelectrons emitted at the electrified interfaces through the liquid layer.[32-33]

Another approach is the utilization of an environmental cell in which a liquid or gas sample can be sealed in a vacuum chamber by using a thin membrane such as graphene oxide,[34] Si,[35-36] and graphene[37-44] as a window for x-rays/photoelectrons and a separator between vacuum and ambient. In contrast to the dip and pull method, this technique, in

principle, does not impose limitation on the thickness of the liquid phase, because neither x-rays nor photoelectrons pass through the liquid. However, photoelectron intensity can be substantially attenuated when passing through the membrane because of the scattering of photoelectrons. For example, the attenuation length of photoelectrons is typically about several nanometers[45] in the case of Mg Kα (*hv*=1,253.6 eV) or Al Kα (*hv*=1,486.7 eV) excitation, which is widely used in a laboratory-based apparatus. Utilization of hard x-rays at synchrotron radiation facilities was considered as an effective approach to detect the photoelectrons through the membrane, because it can significantly increase the attenuation length of photoelectrons. However, it brings about an inevitable reduction in the photoionization cross-sections. Therefore, it is desirable to introduce environmental cells into the common laboratory-based apparatus. The utilization of soft X-rays and thin silicon nitride membranes that have been proposed and demonstrated previously,[34,46] combined with the recent improvements in the laboratory XPS instrument, enables one to revisit this issue.

In our previous report, an environmental cell equipped with a 15 nm-thick Si membrane as a quasi-transparent window was fabricated.[35] Then, an *in-situ* XPS study of electrochemical oxidation of Si at the Si/water interface was carried out under bias application by employing hard X-rays (~6 keV) from a synchrotron source. In the present chapter, we fabricated an environmental cell with a 5 nm-thick silicon nitride membrane and demonstrated XPS of liquid samples in the cell using laboratory-based apparatus with a conventional Al Kα source. Solutions of cesium chloride (CsCl) in water at various concentrations were encapsulated in the cells, and the photoelectrons emitted from the chemical species in the solution with a different concentration were quantitatively detected.

3.2 Environmental cells

Solutions of cesium chloride (CsCl; Kanto Kagaku, 98.0%) with concentrations of 0.6, 1.1, 2.6, and 4.5 M were prepared using pure water from the Milli-Q system (Merck Millipore). Because silicon nitride membrane is most probably non-stoichiometric, it is denoted as SiN.[34] SiN microchips (SiMPore Inc.) were applied as a window of the environmental cell which can encapsulate a liquid sample in its cavity. The microchip has a 5 nm-thick quasi-transparent SiN membrane part whose size is 30 μm-square on the center of a 3 mm-length Si chip, as shown in Figures 3 - 1 (a)–(c).

Figure 3 - 1 (d) illustrates the dimension of the environmental cell and the principle of XPS measurement of liquid samples. The procedure for preparing the environmental cell was reported previously.[35] A plasma treatment (PIB-10, Vacuum Device) was performed to yield a hydrophilic SiN surface, and a droplet of the solution was placed on the surface. After combining the chip with a conductive copper tape (Seiwa Electric MFD), the surrounding of the chip was sealed by posting a sealant available for vacuum (Torr seal®, Varian), and then dried at room temperature in an ambient condition. The resulting cells were screened for the XPS measurements by observing optical images with a microscope, as shown in Figure 3 - 1 (e).

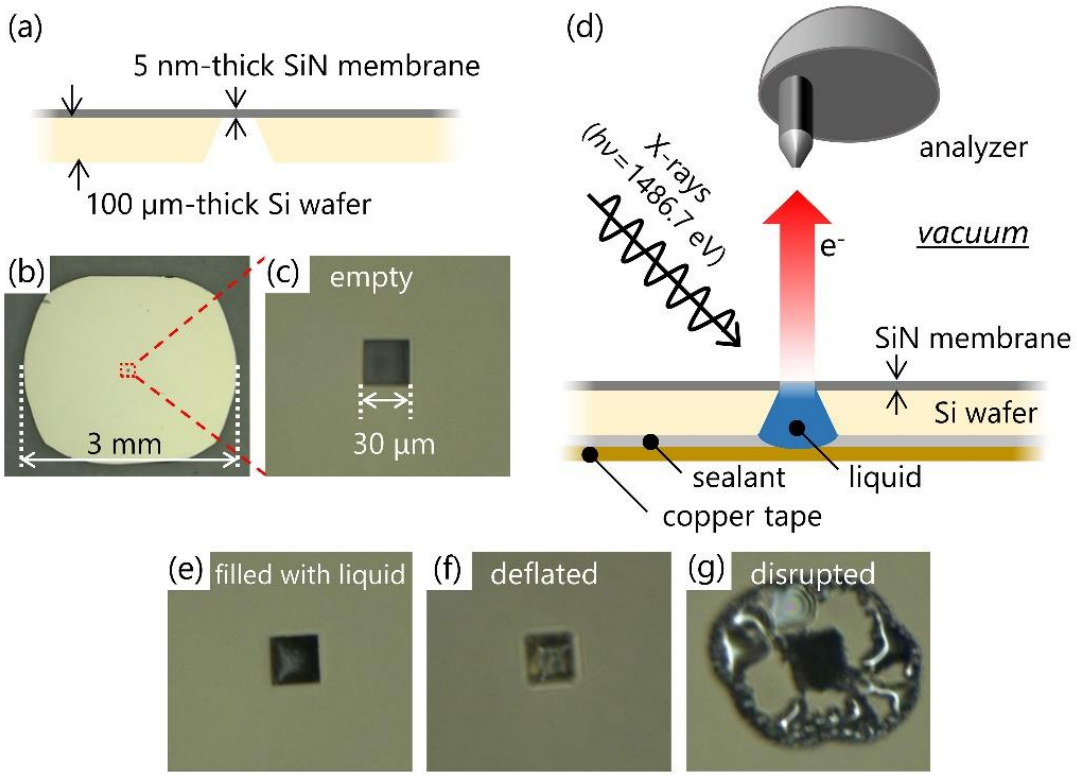

Figure 3 - 1. (a) Cross-sectional and (b) top views of the Si chip and (c) a magnified image of the quasi-transparent SiN membrane. (d) Schematic illustration of the environmental cell and configuration of the XPS system. Photographs of the quasi-transparent windows used for screening: (e) filled with a liquid sample, (f) deflated, and (g) disrupted causing leakage of the liquid sample.

In general, a thinner membrane has a better transparency for photoelectrons, although its mechanical strength becomes weaker (the membrane can be ruptured easily). The attenuation ratio, I_s/I_0, of photoelectrons for three different membranes with thicknesses of 5, 10, and 15 nm was estimated using the following equation:

$$I_s/I_0 = \exp(-d/\lambda \cdot \cos\theta), \qquad (3 - 1)$$

where d, λ, and θ are the thickness of the membrane, the inelastic mean free path of electrons (IMFPs) calculated by the TPP-2M equation,[45] and the emission angle of photoelectrons (0°), respectively. We assumed the stoichiometric Si_3N_4 membranes for

the calculation of λ_{IMFP}. Figure 3 - 2 shows the attenuation ratio of photoelectron through the 5, 10, and 15 nm-thick Si_3N_4 membranes as a function of the kinetic energy of photoelectrons. It suggests that, in the case of 5 nm-thick Si_3N_4 membrane, approximately 20% of photoelectrons ejected from the Cs 4*d* level by Al Kα excitation (kinetic energy = 1,410 eV) pass through the membrane without inelastic scattering, whereas only 4 and 0.8% of photoelectrons pass through 10 and 15 nm-thick membranes. Thus, the 5 nm-thick SiN membrane was chosen as a window for the environmental cells.

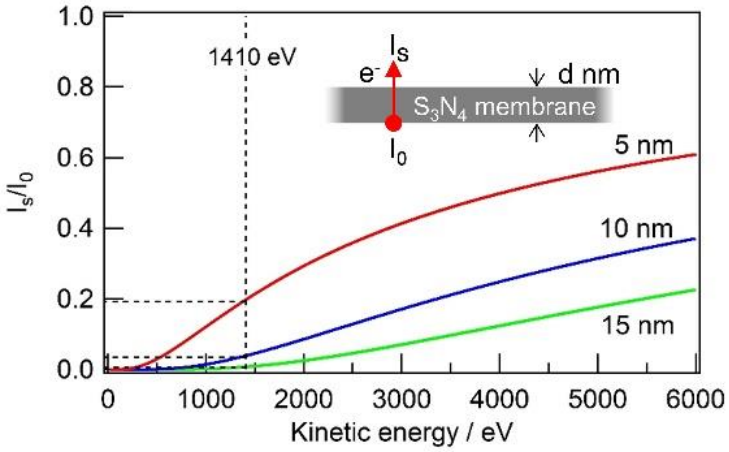

Figure 3 - 2 . Attenuation ratio of the photoelectron intensity (I_S/I_0) passing through the 5 nm (red), 10 nm (blue), and 15 nm-thick (green) Si_3N_4 membranes as a function of the kinetic energy of photoelectrons.

XPS measurements were conducted in AXIS NOVA (Shimadzu Kratos) equipped with a monochromatic Al Kα source with an operating X-ray power of 300 W without charge neutralization by an electron gun. Photoelectron emission angle (θ) was fixed at 0° and the aperture of the hemispherical analyzer was kept at a perpendicular position to the sample surface. The analysis area was a spot with a diameter of 110 μm, and the energy of photoelectrons passing through the analyzer (pass energy) was 160 eV. The

vacuum pressure in the analysis chamber was about 5×10^{-8} Torr.

As a reference sample, cesium chloride solution was drop-casted on a hydrophilic SiN membrane and the dried sample was measured with and without charge neutralization.

3.3 Results and Discussion

3.3.1 XPS observation of CsCl aqueous solutions

Photoelectron spectra in Cs 4d region

The red curve in Figure 3 - 3 shows the Cs 4*d* photoelectron spectrum taken from the cell containing 4.5 M CsCl aqueous solution. A doublet peak corresponding to the Cs $4d_{5/2}$ and $4d_{3/2}$ were observed at 75.8 and 78.1 eV, respectively. The ratio of the peak integrations was calculated to be approximately 3:2 by curve fitting and it is in good agreement with the theoretical value from the split peaks of the *d* orbital.[47] The Cs 4*d* peaks were observed only in the quasi-transparent window part, showing that the obtained Cs 4*d* signals were indeed emitted from the aqueous CsCl solution encapsulated in the cell and detected through the membrane.

The dried CsCl powder deposited on the membrane was measured as a reference through the membrane without charge neutralization. The Cs 4*d* peak shifted to the higher binding energy by more than 5 eV (blue curve in Figure 3 - 3) with respect to that of the liquid sample (red curve in Figure 3 - 3). In addition, the ratio of the Cs $4d_{5/2}$ and $4d_{3/2}$ peaks showed approximately 1:1, which significantly deviates from the theoretical value 3:2. This change, so called charge-up, was caused by the emission of photoelectrons from the highly resistive CsCl. This difference between the solid and

liquid samples implies that the solution is certainly sealed in the cell and acts as conduction paths for electrons. When the solid CsCl was measured with charge neutralization by an electron gun which supplies low energy electrons to compensate the charge due to the ejected photoelectrons, a doublet Cs 4*d* peak in the theoretical ratio was observed at the almost same energy (black curve in Figure 3 - 3) with that of the aqueous solution (red curve in Figure 3 - 3), confirming that the cesium ions observed as a red curve in Figure 3 - 3 certainly exist in the liquid phase.

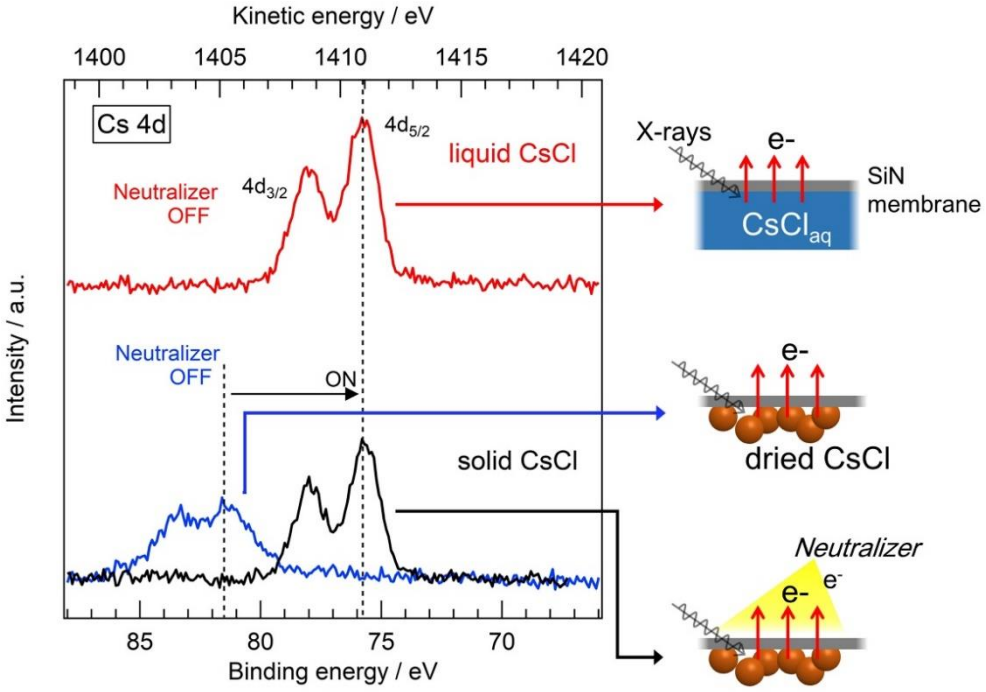

Figure 3 - 3. Cs 4*d* photoelectron spectra acquired from the cells filled with a 4.5 M aqueous CsCl solution without charge neutralization (red curve) and a dry solid CsCl sample without (blue curve) and with charge neutralization (black curve).

As shown in Figure 3 - 3, the Cs 4*d* peak of the dry solid CsCl sample (blue curve in Figure 3 - 3) shifted to a higher binding energy owing to the charge-up effect, although no shift was observed in the spectra of aqueous CsCl solution (red curve in Figure 3 - 3), proving that water provides conduction paths. In the Si 2*p* region of the dry solid CsCl

sample (black curve in Figure 3 - 4 (a)), a peak corresponding to the SiN membrane underneath the dry CsCl powder also shifted owing to the charge-up. On the other hand, no such shift was observed in the spectra acquired from cells containing aqueous CsCl solutions (gray, green, blue, and red curves in Figure 3 - 4 (a)), confirming the effective suppression of charging by water.

A peak was observed in the C 1*s* region of the photoelectron spectra acquired from cells containing aqueous CsCl solutions (Figure 3 - 4 (b)). Carbon is considered to be a contaminant adsorbed on the surface of the SiN membrane on the external surface of the cell (that is, the surface not in contact with the liquid but in contact with vacuum). Because the C 1*s* peaks are slightly shifted to the higher binding energy, the SiN surface at the external side of the cell might be slightly charged, unlike the internal surface in contact with the liquid.

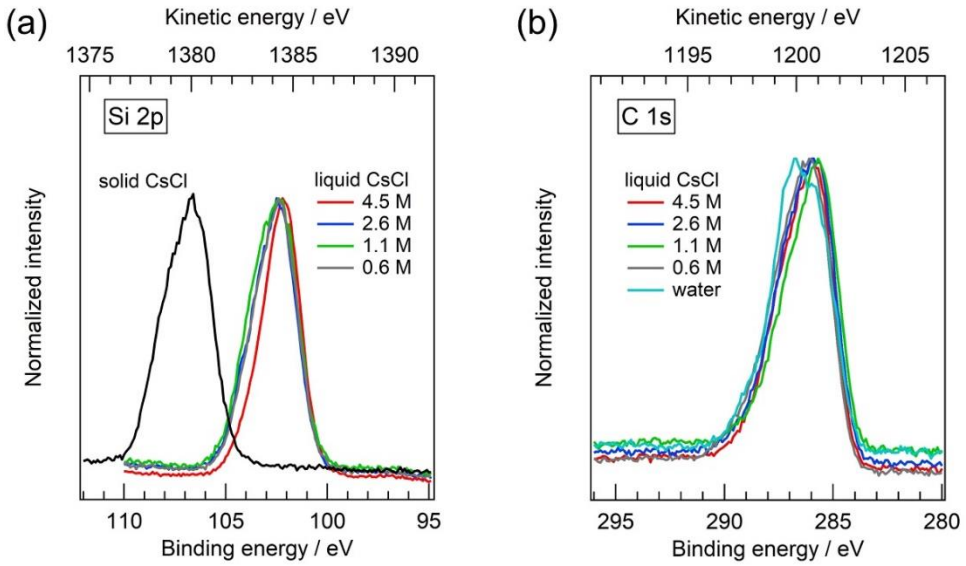

Figure 3 - 4. Photoelectron spectra acquired from cells containing aqueous CsCl solutions in the regions of (a) Si 2*p* and (b) C 1*s*. Si 2*p* spectrum of the dry CsCl sample is also shown for comparison.

The quantitative analysis of cesium ions in solutions was performed as shown in Figures 3 - 5 (a)–(c). The intensity of Cs 4$d_{5/2}$ peak increased in proportion to the concentration of the CsCl solution when the cells filled with aqueous CsCl solutions at different concentrations (0.6, 1.1, 2.6, and 4.5 M) were analyzed as well as pure water as a reference. This result clearly indicates the capability of this technique for quantitative characterization of chemical species in solution. Meanwhile, the position of Cs 4$d_{5/2}$ peak at each concentration remains almost constant (Figure 3 - 5 (c), standard deviation ±0.13 eV), suggesting that the oxidation state of cesium ions was almost identical.

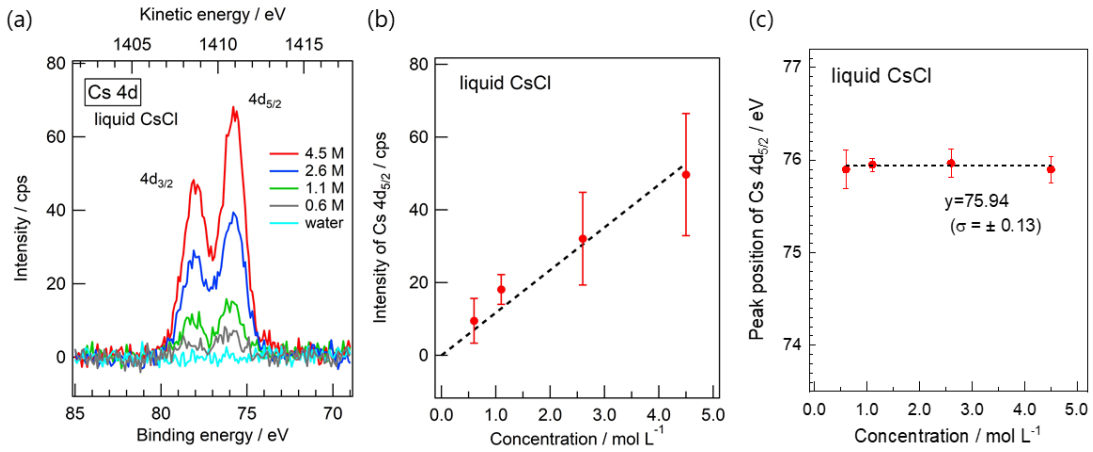

Figure 3 - 5. (a) Cs 4*d* photoelectron spectra of pure water and 0.6, 1.1, 2.6, and 4.5 M aqueous CsCl solutions in environmental cells. Each spectrum was collected with an acquisition time of ~200 min. Linear approximation was adopted for background subtraction. Concentration-dependence of the (b) intensity and (c) position of the Cs 4$d_{5/2}$ peak. The black dashed lines are linear fits to the data. The error bars represent standard deviation from the mean (n=2 or 3).

Wide scan spectra and photoelectron spectra in Cs 4d, Si 2s, Si 2p, and N 1s regions

Figure 3 - 6 (a) shows wide scan spectra of pure water and 0.6, 1.1, 2.6, and 4.5 M aqueous CsCl solutions filled in cells. Not only Cs 4*d* but also Cs 3*d* peaks were observed from the aqueous CsCl solution, as shown in Figures 3 - 6 (b) and (c). Peak areas of Cs 4*d*, Si 2*s*, Si 2*p*, and N 1*s* are summarized in Table 3 - 1. The peak area ratios of Cs 4*d*/Si 2*s*, Cs 4*d*/Si 2*p*, and Cs 4*d*/N 1*s* were also proportionally increased with the concentrations, as shown in Figures 3 - 7 (a)–(c).

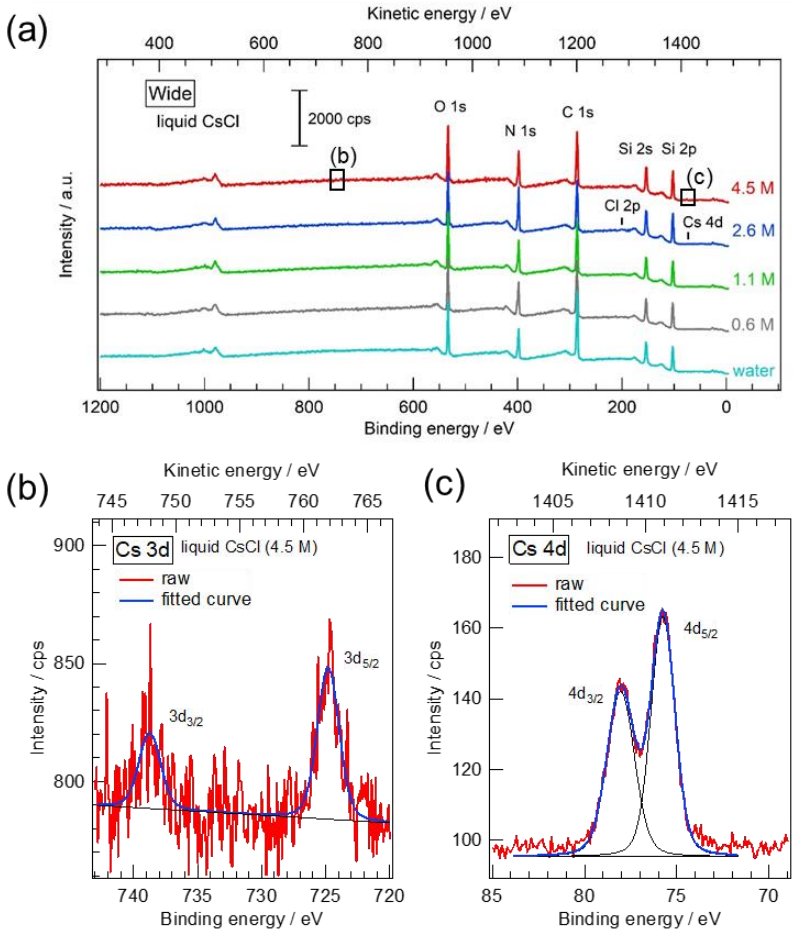

Figure 3 - 6. (a) Wide scan, (b) Cs 3*d*, and (c) Cs 4*d* photoelectron spectra of pure water and 0.6, 1.1, 2.6, and 4.5 M aqueous CsCl solutions in cells.

Table 3 - 1. Peak areas of Cs 4*d*, Si 2*s*, Si 2*p*, and N 1*s* and the ratios of Cs 4*d*/Si 2*s*, Cs 4*d*/Si 2*p*, and Cs 4*d*/N 1*s* for aqueous CsCl solutions and pure water.

Concentration/ mol L^{-1}	Peak area/ cps				Peak area ratio		
	Cs 4*d*	Si 2*s*	Si 2*p*	N 1*s*	Cs 4*d*/Si 2*s*	Cs 4*d*/Si 2*p*	Cs 4*d*/N 1*s*
4.5	154.0 ± 50.7	4230 ± 930	4282 ± 924	5764 ± 2130	0.0355 ± 0.0042	0.0350 ± 0.0043	0.0267 ± 0.0013
2.6	99.4 ± 38.7	3983 ± 967	4262 ± 1031	4894 ± 1009	0.0256 ± 0.0111	0.0237 ± 0.0098	0.0203 ± 0.0090
1.1	47.5 ± 7.6	3527 ± 771	3812 ± 782	4647 ± 882	0.0146 ± 0.0053	0.0134 ± 0.0047	0.0102 ± 0.0037
0.6	25.5 ± 18.4	3271 ± 369	3535 ± 306	4442 ± 537	0.0074 ± 0.0046	0.0069 ± 0.0045	0.0057 ± 0.0033
0	0	2769	2910	3116	0	0	0

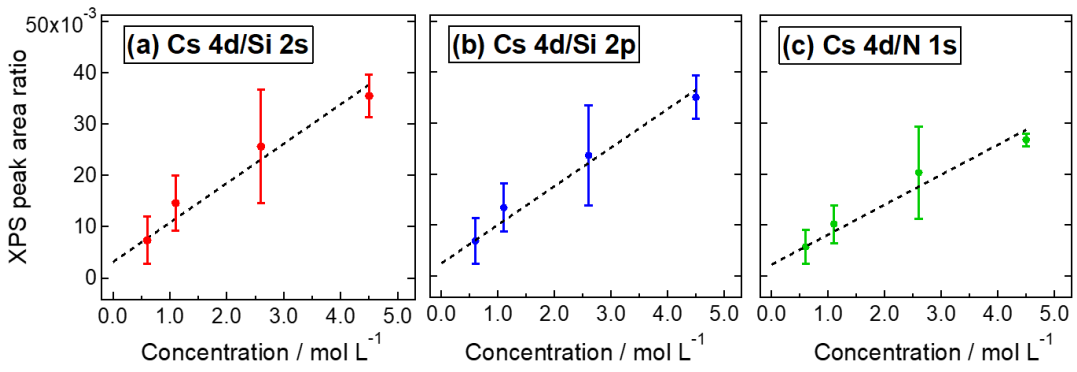

Figure 3 - 7. Dependence of the ratios of (a) Cs 4*d*/Si 2*s*, (b) Cs 4*d*/Si 2*p*, and (c) Cs 4*d*/N 1*s* on the concentration of CsCl in water. Dashed lines are linear fits to the data.

Photoelectron spectra in Cl 2p and O 1s regions

Cl 2*p* and O 1*s* energy regions were measured to observe the chloride ions and liquid H_2O in the aqueous solution. Figures 3 - 8 (a) and (b) show the photoelectron spectra in the Cl 2*p* and O 1*s* regions acquired from the cells filled with pure water and 0.6 and 1.1 M aqueous CsCl solutions. In the Cl 2*p* region, the plasmon loss peak of Si 2*s* overlapped with the Cl 2*p* peaks. Moreover, Cl components were incorporated in the SiN membranes because a gas containing Cl species was used as a precursor for the formation of the SiN membrane. In the O 1*s* region, the peak observed at ~533 eV should be due to contaminants such as carbonates and silicon oxide at the SiN membrane. These strong features hindered the quantitative deconvolution of the peaks corresponding to chloride ions and H_2O in the aqueous solution.

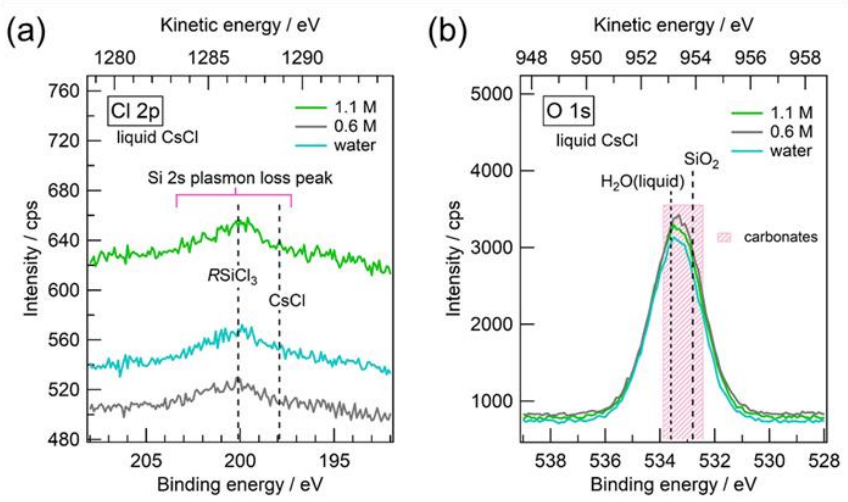

Figure 3 - 8. Photoelectron spectra acquired from cells filled with pure water and 0.6 and 1.1 M aqueous CsCl solutions in the region of (a) Cl 2*p* and (b) O 1*s*. Dashed lines indicate the peak positions of *R*$SiCl_3$ (*R*: alkyl group),[48] CsCl,[49] H_2O (liquid),[34] and SiO_2.[50] respectively. The shaded area corresponds to contaminants such as carbonates.[51]

3.4 Conclusions

We fabricated environmental cells filled with aqueous CsCl solutions of various concentrations using a 5 nm-thick SiN membrane as a transparent window for the transmission of x-rays and photoelectrons. The Cs 4*d* photoelectrons passing through the membrane were detected using a laboratory-based XPS apparatus equipped with a conventional Al Kα source. Furthermore, the peak intensity increased proportionally with the concentration of the solutions.

Chemical species located in deeper regions were quantitatively observed using XPS, proving the capability of this technique for quantitative characterization of liquid samples and solid/liquid interfaces.

References

1. Endo, R.; Watanabe, D.; Shimomura, M.; Masuda, T., *In situ* X-ray photoelectron spectroscopy using a conventional Al-Kα source and an environmental cell for liquid samples and solid-liquid interfaces. *Appl. Phys. Lett.* **2019,** *114* (17), 173702.
2. Winter, B.; Faubel, M., Photoemission from Liquid Aqueous Solutions. *Chem. Rev.* **2006,** *106* (4), 1176-1211.
3. Winter, B., Liquid microjet for photoelectron spectroscopy. *Nucl. Instrum. Methods Phys. Res., Sect. A* **2009,** *601* (1-2), 139-150.
4. Salmeron, M.; Schlogl, R., Ambient pressure photoelectron spectroscopy: A new tool for surface science and nanotechnology. *Surf. Sci. Rep.* **2008,** *63* (4), 169-199.
5. Trotochaud, L.; Head, A. R.; Karslioglu, O.; Kyhl, L.; Bluhm, H., Ambient pressure photoelectron spectroscopy: Practical considerations and experimental frontiers. *J. Phys. Condens: Matter* **2017,** *29* (5), 053002.
6. Masuda, T., Various spectroelectrochemical cells for in situ observation of electrochemical processes at solid-liquid interfaces. *Top. Catal.* **2018,** *61* (20), 2103-2113.
7. Siegbahn, H.; Siegbahn, K., ESCA applied to liquids. *J. Electron. Spectrosc. Relat. Phenom.* **1973,** *2* (3), 319-325.
8. Siegbahn, H.; Asplund, L.; Kelfve, P.; Hamrin, K.; Karlsson, L.; Siegbahn, K., ESCA applied to

liquids. II. Valence and core electron spectra of formamide. *J. Electron. Spectrosc. Relat. Phenom.* **1974,** *5* (1), 1059-1079.

9. Siegbahn, H.; Asplund, L.; Kelfve, P.; Siegbahn, K., Esca applied to liquids III. ESCA phase shifts in pure and mixed organic solvents. *J. Electron. Spectrosc. Relat. Phenom.* **1975,** *7* (5), 411-419.
10. Winter, B.; Weber, R.; Widdra, W.; Dittmar, M.; Faubel, M.; Hertel, I. V., Full Valence Band Photoemission from Liquid Water Using EUV Synchrotron Radiation. *J. Phys. Chem. A* **2004,** *108* (14), 2625-2632.
11. Winter, B.; Aziz, E. F.; Hergenhahn, U.; Faubel, M.; Hertel, I. V., Hydrogen bonds in liquid water studied by photoelectron spectroscopy. *J. Chem. Phys.* **2007,** *126* (12), 124504.
12. Perrine, K. A.; Van Spyk, M. H. C.; Margarella, A. M.; Winter, B.; Faubel, M.; Bluhm, H.; Hemminger, J. C., Characterization of the Acetonitrile Aqueous Solution/Vapor Interface by Liquid-Jet X-ray Photoelectron Spectroscopy. *J. Phys. Chem. C* **2014,** *118* (50), 29378-29388.
13. Winter, B.; Weber, R.; Schmidt, P. M.; Hertel, I. V.; Faubel, M.; Vrbka, L.; Jungwirth, P., Molecular structure of surface-active salt solutions: Photoelectron spectroscopy and molecular dynamics simulations of aqueous tetrabutylammonium iodide. *J. Phys. Chem. B* **2004,** *108* (38), 14558-14564.
14. Söderström, J.; Ottosson, N.; Pokapanich, W.; Öhrwall, G.; Björneholm, O., Functionalized nanoparticles in aqueous surroundings probed by X-ray photoelectron spectroscopy. *J. Electron. Spectrosc. Relat. Phenom.* **2011,** *184* (7), 375-378.
15. Brown, M. A.; Beloqui Redondo, A.; Sterrer, M.; Winter, B.; Pacchioni, G.; Abbas, Z.; van Bokhoven, J. A., Measure of Surface Potential at the Aqueous–Oxide Nanoparticle Interface by XPS from a Liquid Microjet. *Nano Lett.* **2013,** *13* (11), 5403-5407.
16. Olivieri, G.; Brown, M. A., Structure of a Core–Shell Type Colloid Nanoparticle in Aqueous Solution Studied by XPS from a Liquid Microjet. *Top. Catal.* **2016,** *59* (5-7), 621-627.
17. Mayer, T.; Lebedev, M.; Hunger, R.; Jaegermann, W., Elementary processes at semiconductor/electrolyte interfaces: perspectives and limits of electron spectroscopy. *Appl. Surf. Sci.* **2005,** *252* (1), 31-42.
18. Lebedev, M. V.; Calvet, W.; Kaiser, B.; Jaegermann, W., Synchrotron Photoemission Spectroscopy Study of p-GaInP2(100) Electrodes Emersed from Aqueous HCl Solution under Cathodic Conditions. *J. Phys. Chem. C* **2017,** *121* (16), 8889-8901.
19. Wakisaka, M.; Mitsui, S.; Hirose, Y.; Kawashima, K.; Uchida, H.; Watanabe, M., Electronic structures of Pt-Co and Pt-Ru alloys for CO-tolerant anode catalysts in polymer electrolyte fuel cells studied by EC-XPS. *J. Phys. Chem. B* **2006,** *110* (46), 23489-96.
20. Wakisaka, M.; Suzuki, H.; Mitsui, S.; Uchida, H.; Watanabe, M., Increased Oxygen Coverage at Pt−Fe Alloy Cathode for the Enhanced Oxygen Reduction Reaction Studied by EC−XPS. *The Journal of Physical Chemistry C* **2008,** *112* (7), 2750-2755.
21. Wong, R. A.; Yokota, Y.; Wakisaka, M.; Inukai, J.; Kim, Y., Discerning the Redox-Dependent

Electronic and Interfacial Structures in Electroactive Self-Assembled Monolayers. *J. Am. Chem. Soc.* **2018,** *140* (42), 13672-13679.

22. Taylor, A. W.; Qiu, F.; Villar-Garcia, I. J.; Licence, P., Spectroelectrochemistry at ultrahigh vacuum: in situ monitoring of electrochemically generated species by X-ray photoelectron spectroscopy. *Chem. Commun.* **2009,** (39), 5817-9.
23. Wibowo, R.; Aldous, L.; Jacobs, R. M. J.; Manan, N. S. A.; Compton, R. G., In situ electrochemical-X-ray Photoelectron Spectroscopy: Rubidium metal deposition from an ionic liquid in competition with solvent breakdown. *Chem. Phys. Lett.* **2011,** *517* (1-3), 103-107.
24. Tang, C. Y.; Haasch, R. T.; Dillon, S. J., In situ X-ray photoelectron and Auger electron spectroscopic characterization of reaction mechanisms during Li-ion cycling. *Chem. Commun.* **2016,** *52* (90), 13257-13260.
25. Casalongue, H. S.; Kaya, S.; Viswanathan, V.; Miller, D. J.; Friebel, D.; Hansen, H. A.; Norskov, J. K.; Nilsson, A.; Ogasawara, H., Direct observation of the oxygenated species during oxygen reduction on a platinum fuel cell cathode. *Nat. Commun.* **2013,** *4* (1), 2817.
26. Takagi, Y.; Wang, H.; Uemura, Y.; Ikenaga, E.; Sekizawa, O.; Uruga, T.; Ohashi, H.; Senba, Y.; Yumoto, H.; Yamazaki, H.; Goto, S.; Tada, M.; Iwasawa, Y.; Yokoyama, T., In situ study of an oxidation reaction on a Pt/C electrode by ambient pressure hard X-ray photoelectron spectroscopy. *Appl. Phys. Lett.* **2014,** *105* (13), 131602.
27. Nemsak, S.; Shavorskiy, A.; Karslioglu, O.; Zegkinoglou, I.; Rattanachata, A.; Conlon, C. S.; Keqi, A.; Greene, P. K.; Burks, E. C.; Salmassi, F.; Gullikson, E. M.; Yang, S. H.; Liu, K.; Bluhm, H.; Fadley, C. S., Concentration and chemical-state profiles at heterogeneous interfaces with sub-nm accuracy from standing-wave ambient-pressure photoemission. *Nat. Commun.* **2014,** *5*, 5441.
28. Saveleva, V. A.; Papaefthimiou, V.; Daletou, M. K.; Doh, W. H.; Ulhaq-Bouillet, C.; Diebold, M.; Zafeiratos, S.; Savinova, E. R., Operando Near Ambient Pressure XPS (NAP-XPS) Study of the Pt Electrochemical Oxidation in H2O and H2O/O2 Ambients. *J. Phys. Chem. C* **2016,** *120* (29), 15930-15940.
29. Streibel, V.; Hävecker, M.; Yi, Y.; Velasco-Vélez, J. J.; Skorupska, K.; Stotz, E.; Knop-Gericke, A.; Schlögl, R.; Arrigo, R., In Situ Electrochemical Cells to Study the Oxygen Evolution Reaction by Near Ambient Pressure X-ray Photoelectron Spectroscopy. *Top. Catal.* **2018,** *61* (20), 2064-2084.
30. Axnanda, S.; Crumlin, E. J.; Mao, B.; Rani, S.; Chang, R.; Karlsson, P. G.; Edwards, M. O.; Lundqvist, M.; Moberg, R.; Ross, P.; Hussain, Z.; Liu, Z., Using "Tender" X-ray Ambient Pressure X-Ray Photoelectron Spectroscopy as A Direct Probe of Solid-Liquid Interface. *Sci. Rep.* **2015,** *5*, 9788.
31. Lichterman, M. F.; Hu, S.; Richter, M. H.; Crumlin, E. J.; Axnanda, S.; Favaro, M.; Drisdell, W.; Hussain, Z.; Mayer, T.; Brunschwig, B. S.; Lewis, N. S.; Liu, Z.; Lewerenz, H.-J., Direct observation of the energetics at a semiconductor/liquid junction by operando X-ray photoelectron spectroscopy.

Energy Environ. Sci. **2015,** *8* (8), 2409-2416.

32. Ali-Löytty, H.; Louie, M. W.; Singh, M. R.; Li, L.; Sanchez Casalongue, H. G.; Ogasawara, H.; Crumlin, E. J.; Liu, Z.; Bell, A. T.; Nilsson, A.; Friebel, D., Ambient-Pressure XPS Study of a Ni–Fe Electrocatalyst for the Oxygen Evolution Reaction. *J. Phys. Chem. C* **2016,** *120* (4), 2247-2253.
33. Favaro, M.; Jeong, B.; Ross, P. N.; Yano, J.; Hussain, Z.; Liu, Z.; Crumlin, E. J., Unravelling the electrochemical double layer by direct probing of the solid/liquid interface. *Nat. Commun.* **2016,** *7*, 12695.
34. Kolmakov, A.; Dikin, D. A.; Cote, L. J.; Huang, J.; Abyaneh, M. K.; Amati, M.; Gregoratti, L.; Gunther, S.; Kiskinova, M., Graphene oxide windows for in situ environmental cell photoelectron spectroscopy. *Nat. Nanotech.* **2011,** *6* (10), 651-7.
35. Masuda, T.; Yoshikawa, H.; Noguchi, H.; Kawasaki, T.; Kobata, M.; Kobayashi, K.; Uosaki, K., *In situ* x-ray photoelectron spectroscopy for electrochemical reactions in ordinary solvents. *Appl. Phys. Lett.* **2013,** *103* (11), 111605.
36. Masuda, T.; Uosaki, K., In situ determination of electronic structure at solid/liquid interfaces. *J. Electron. Spectrosc. Relat. Phenom.* **2017,** *221*, 88-98.
37. Kraus, J.; Reichelt, R.; Gunther, S.; Gregoratti, L.; Amati, M.; Kiskinova, M.; Yulaev, A.; Vlassiouk, I.; Kolmakov, A., Photoelectron spectroscopy of wet and gaseous samples through graphene membranes. *Nanoscale* **2014,** *6* (23), 14394-403.
38. Nemšák, S.; Strelcov, E.; Duchoň, T.; Guo, H.; Hackl, J.; Yulaev, A.; Vlassiouk, I.; Mueller, D. N.; Schneider, C. M.; Kolmakov, A., Interfacial electrochemistry in liquids probed with photoemission electron microscopy. *J. Am. Chem. Soc.* **2017,** *139* (50), 18138-18141.
39. Velasco-Vélez, J. J.; Pfeifer, V.; Havecker, M.; Weatherup, R. S.; Arrigo, R.; Chuang, C. H.; Stotz, E.; Weinberg, G.; Salmeron, M.; Schlogl, R.; Knop-Gericke, A., Photoelectron spectroscopy at the graphene-liquid interface reveals the electronic structure of an electrodeposited cobalt/graphene electrocatalyst. *Angew. Chem. Int. Ed. Engl.* **2015,** *54* (48), 14554-8.
40. Velasco-Vélez, J. J.; Pfeifer, V.; Havecker, M.; Wang, R.; Centeno, A.; Zurutuza, A.; Algara-Siller, G.; Stotz, E.; Skorupska, K.; Teschner, D.; Kube, P.; Braeuninger-Weimer, P.; Hofmann, S.; Schlogl, R.; Knop-Gericke, A., Atmospheric pressure X-ray photoelectron spectroscopy apparatus: Bridging the pressure gap. *Rev. Sci. Instrum.* **2016,** *87* (5), 053121.
41. Knop-Gericke, A.; Pfeifer, V.; Velasco-Vélez, J. J.; Jones, T.; Arrigo, R.; Havecker, M.; Schlogl, R., In situ X-ray photoelectron spectroscopy of electrochemically active solid-gas and solid-liquid interfaces. *J. Electron. Spectrosc. Relat. Phenom.* **2017,** *221*, 10-17.
42. Weatherup, R. S.; Eren, B.; Hao, Y.; Bluhm, H.; Salmeron, M. B., Graphene Membranes for Atmospheric Pressure Photoelectron Spectroscopy. *J. Phys. Chem. Lett.* **2016,** *7* (9), 1622-7.
43. Nguyen, L.; Tao, P. P.; Liu, H.; Al-Hada, M.; Amati, M.; Sezen, H.; Gregoratti, L.; Tang, Y.; House, S. D.; Tao, F. F., X-ray Photoelectron Spectroscopy Studies of Nanoparticles Dispersed in Static

Liquid. *Langmuir* **2018,** *34* (33), 9606-9616.

44. Nguyen, L.; Tao, P. P.; Liu, H.; Al-Hada, M.; Amati, M.; Sezen, H.; Tang, Y.; Gregoratti, L.; Tao, F. F., Studies of surface of metal nanoparticles in a flowing liquid with XPS. *Chem. Commun.* **2018,** *54* (71), 9981-9984.
45. Tanuma, S.; Powell, C. J.; Penn, D. R., Calculation of electron inelastic mean free paths (IMFPs) VII. Reliability of the TPP-2M IMFP predictive equation. *Surf. Interface Anal.* **2003,** *35* (3), 268-275.
46. III, C. E. B.; Grunthaner, F. J.; Grunthaner, P. J. Electron transmissive window usable with high pressure electron spectrometry. U.S. Patent 6,803,570 B1, 12 Oct, 2004.
47. Wagner, C. D.; Davis, L. E.; Zeller, M. V.; Taylor, J. A.; Raymond, R. H.; Gale, L. H., Empirical Atomic Sensitivity Factors for Quantitative Analysis by Electron Specroscopy for Chemical Analysis. *Surf. Interface Anal.* **1981,** *3* (5), 211-225.
48. Paz, Y.; Trakhtenberg, S.; Naaman, R., REACTION BETWEEN O(P-3) AND ORGANIZED ORGANIC THIN-FILMS. *J. Phys. Chem.* **1994,** *98* (51), 13517-13523.
49. Nefedov, V. I.; Salyn, Y. V.; Baranovskii, I. B.; Maiorova, A. G., X-RAY ELECTRON STUDIES OF RH AND PT COMPOUNDS WITH METAL-METAL BOND. *Zh. Neorg. Khim.* **1980,** *25* (1), 216-225.
50. Lars, S.; Andersson, T.; Scurrell, M. S., Infrared and ESCA studies of a heterogenized rhodium carbonylation catalyst. *J. Catal.* **1979,** *59* (3), 340-356.
51. Beamson, G.; Briggs, D., *High Resolution XPS of Organic Polymers: The Scienta ESCA300 Database*. Wiley: 1992.

Chapter 4. Static and dynamic analyses of initial lithiation/delithiation of amorphous-Si thin-film electrodes

4.1 Introduction

Si thin-film electrodes in a similar structure were previously explored by a few research groups.[1-2] For example, Chen et al. demonstrated that Si/LLZT/Li-configured amorphous-Si films exhibited a stable cycle performance without any remarkable side reactions at Si/LLZT interfaces.[1] Sakabe et al. constructed amorphous-Si thin films on a thiophosphate-based solid electrolyte ($80Li_2S{\cdot}20P_2S_5$ glass).[2] In these studies, although a significant volumetric change of the Si electrodes (approximately 300%) due to the lithiation was observed by scanning electron microscopy (SEM), relatively stable cycle performance and high capacity retention after 100 cycles were achieved. The first lithiation and delithiation of a Si/LLZT/Li-configured amorphous-Si thin-film electrode deposited on a $Li_{6.6}La_3Zr_{1.6}Ta_{0.4}O_{12}$ (LLZT) solid electrolyte were statically and dynamically studied using an *in-situ* XPS system on the basis of the elemental composition and chemical state of the Si thin-film electrode. In addition, the volumetric expansion of the Si thin-film electrode was monitored using *in-situ* AFM in the first lithiation.

4.2 Results and Discussion

4.2.1 Galvanostatic potential profiles

Cycle performances measured under Ar and vacuum

Figure 4 - 1 compares the galvanostatic lithiation/delithiation potential profiles measured under Ar and vacuum without applying compression. The potential profiles were obtained using the sample holder previously described in Chapter 2 without applying any compression to the thin-film cell.

Under Ar, the thin-film cell showed an irreversible potential profile (Figure 4 - 1 (a)). The first lithiation capacity measured under Ar reached 4,236 mAh g^{-1}, which is much higher than the theoretical capacity at room temperature (3,579 mAh g^{-1}). In the subsequent delithiation, however, stable current was not observed and the potential difference between Si and Li electrodes became zero. This short circuit is considered to be due to the dendrite formation of the LLZT/Li interfaces.[3, 4] In contrast, the potential profile measured under vacuum was reversible as is the potential profile measured under Ar with compression (Figure 4 - 1 (b)).

Figures 4 - 2 (a) and (b) show the AC impedance profiles for the thin-film cells cycled under Ar and vacuum, respectively. The resistance of the cell cycled under Ar (Figure 4 - 2 (a)) was much lower than that of the one cycled under vacuum (Figure 4 - 2 (b)) and almost zero, confirming the short-circuit of thin-film cell cycled under Ar without applying any compression.

Si thin-film cells needs to be cycled under compression under Ar;[5] otherwise, they either exhibit rapid capacity fading or short-circuit, as in the present case. In the present study, however, reversible cycling was achieved without applying any compression under vacuum. Thus, all the following measurements were performed under vacuum

without applying any compression unless otherwise noted.

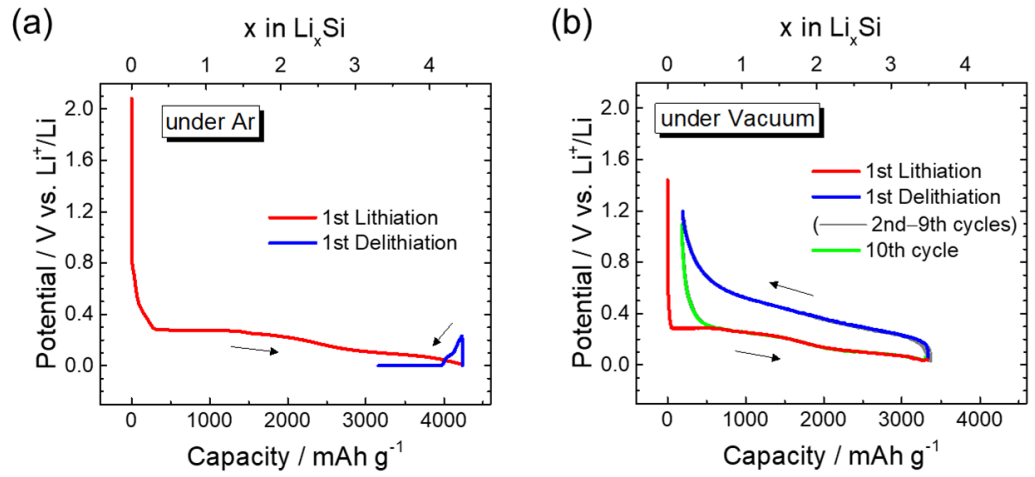

Figure 4 - 1. Galvanostatic lithiation/delithiation potential profiles obtained for Si/LLZT/Li cell at 0.02 C and cutoff potential in range 0.01–1.2 V *vs.* Li$^+$/Li (a) under Ar and (b) vacuum (5 × 10^{-9} Torr). Both thin-film cells were cycled without applying any compression. Specific capacity was normalized by mass of deposited Si.

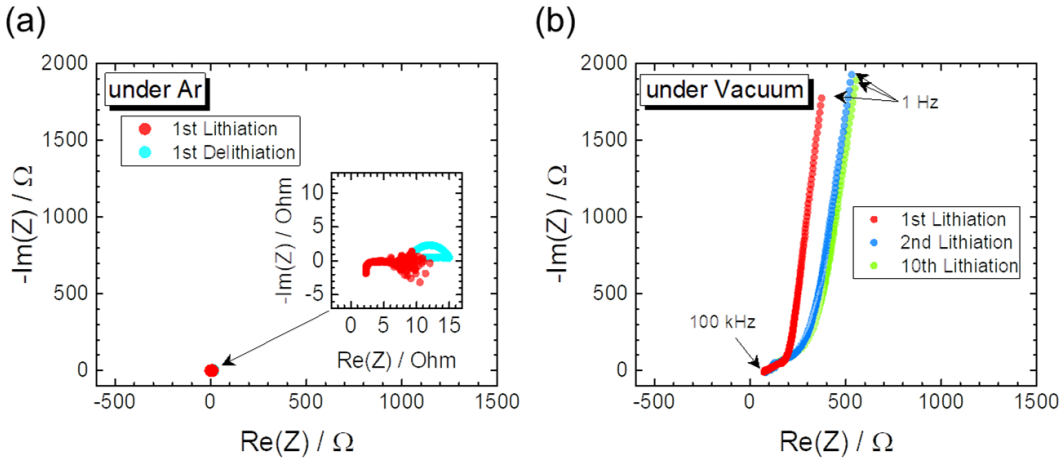

Figure 4 - 2. Electrochemical impedance profiles obtained for Si/LLZT/Li thin-film cells cycled under (a) Ar and (b) vacuum (5 × 10^{-9} Torr). Inset of (a) shows magnified region of impedance profile near arrow head. Measurements were performed from 100 kHz to 1 Hz by applying 10-mV-amplitude AC signal.

First lithiation/delithiation cycles measured using in-situ XPS

Figure 4 - 3 shows the galvanostatic lithiation/delithiation potential profiles of thin-film cell measured under vacuum in the first cycle. The charge integrations obtained for the first lithiation (from A to B) and delithiation (from B to C) were 3,330 and 3,137 mAh g^{-1}, respectively. Their difference, i.e., the irreversible capacity, was 193 mAh g^{-1}. The electrical charges obtained for the first lithiation/delithiation are in good agreement with previous reports.[2, 6] The composition of lithium silicide at B and C are denoted as Li_xSi and Li_ySi, respectively. Assuming that all the electrical charges were used to form lithium silicide, the apparent compositions were estimated to be $Li_{3.49}Si$ and $Li_{0.20}Si$ at B and C, respectively. However, the formation of Li_2O, as revealed by XPS (see static XPS results), suggests that the lithium silicide partially reacted with oxygen species. Thus, *x* and *y* should be somewhat lower than 3.49 and 0.20, respectively (to be discussed in the following sections).

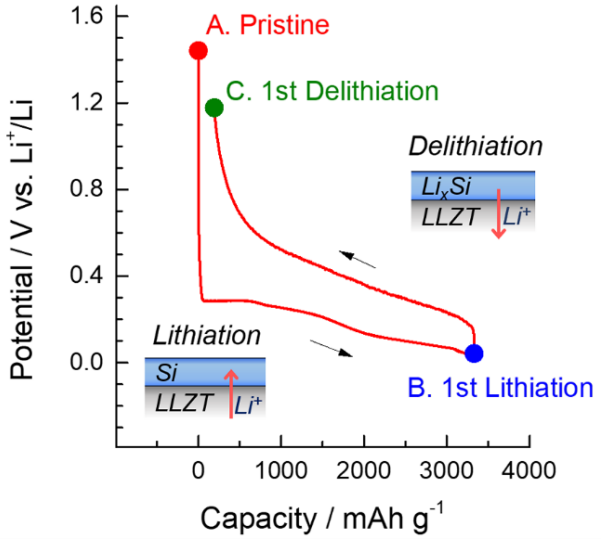

Figure 4 - 3. Galvanostatic first lithiation/delithiation potential profiles obtained for Si/LLZT/Li cell cycled at 0.02 C and cutoff potential in range 0.01–1.2 V *vs.* Li^+/Li. XPS measurements were performed at red, blue, and green points denoted by A–C, respectively.

Cycle performance

The cycle performance and corresponding coulombic efficiency obtained in subsequent cycles are shown in Figure 4 - 4. Samples 1 and 2 were both prepared in the same batch. Although the capacity gradually decreased with increasing the number of cycles, the coulombic efficiency remained at approximately 100% after the second cycle. It is noted that, although a certain area of Si electrode is exposed to vacuum for XPS without a Cu current collector, the reversible capacity and cycle performance of this cell is almost identical to the cell where the entire Si electrode is covered by a Cu current collector.

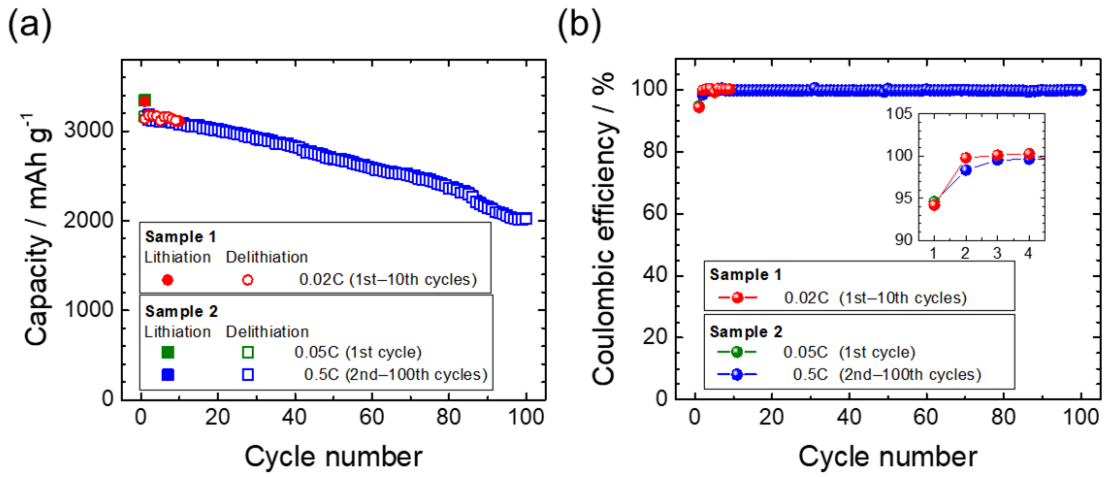

Figure 4 - 4. (a) Cycle performance and (b) corresponding coulombic efficiency of Si/LLZT/Li cells (samples 1 and 2) measured at different current densities in ultrahigh-vacuum (UHV) chamber of XPS apparatus. Inset shows magnified view of (b). Sample 1 was used for static *in-situ* XPS measurements. Specific capacity was normalized by mass of deposited Si.

4.2.2 Static reaction analysis of electrochemical lithiation of Si anode at various states of charge

4.2.2.1 Static XPS analysis using Al Kα incident x-rays

Figure 4 - 5 shows the XPS spectra generated for the Li 1*s*, Si 2*p*, and O 1*s* energy regions of the Si surface at A–C of the potential profile in Figure 4 - 3. Although no peak was observed in the Li 1*s* region of the spectrum for the pristine Si electrode (Figure 4 - 5 A), a broad Li peak appeared after the lithiation (Figure 4 - 5 B), indicating that the Li ions was reductively inserted into the Si electrode from the LLZT and then uniformly diffused to reach the analysis surface.

The broad Li 1*s* peak was deconvoluted into peaks attributed to lithium oxide (Li_2O), lithium carbonate (Li_2CO_3), lithium silicates (Li silicates), and lithium silicides (Li_xSi).[7-9] The formation of Li_2O and Li_2CO_3 are commonly detected as byproduct using various analysis techniques,[10-12] suggesting the side reactions of Li_xSi with a trace amount of oxygen species and/or carbon dioxide possibly from the ultrahigh-vacuum (UHV) chamber or LLZT. The broad Li 1*s* peak composed of peaks attributed to Li_2O, Li_2CO_3, and Li silicates remained after delithiation. This shows that those are inactive irreversible species.

In the Si 2*p* region of the spectrum for the pristine Si electrode (Figure 4 - 5 A), strong and small peaks were observed at 99.1 and 101.9 eV, corresponding to bulk Si and a native suboxide (SiO_z), respectively, formed by reaction of the sputter-deposited Si surface with a trace amount of oxygen under vacuum.[13-14] After the lithiation (Figure 4 - 5 B), the intensity of the Si peak decreased by approximately 20 times, probably due to the insertion of Li into Si and the formation of upper Li_2O, Li_2CO_3, and Li-silicates layers More interestingly, the peaks corresponding to Si and SiO_z both shifted to lower

binding energies of up to 95.2 and 101.0 eV, respectively. The former and latter peaks were attributed to the Li_xSi and Li silicates formed by the lithiation of the bulk Si and suboxide (SiO_z), respectively.[12, 15-17] After the subsequent delithiation (Figure 4 - 5 C), the Li_xSi peak at 95.2 eV shifted to higher binding energy of 97.5 eV, but did not revert to the original position at 99.1 eV corresponding to the bulk Si. This observation is indeed consistent with the existence of irreversible capacity loss in Figure 4 - 3. In contrast, the Li-silicates peak at 101.0 eV did not shift during delithiation, confirming that the Li silicates are also irreversibility species.

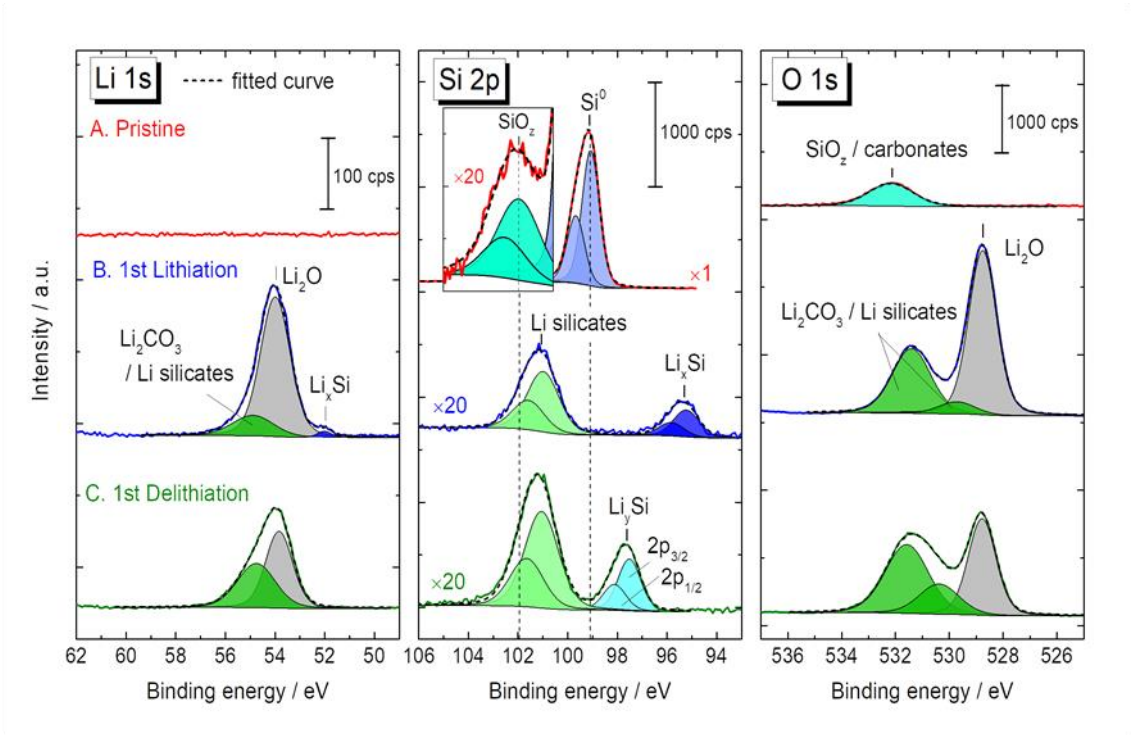

Figure 4 - 5. Li 1*s*, Si 2*p*, and O 1*s* spectra generated for Si electrode at A–C shown in Figure 4 - 3: (A) pristine electrode and after the first (B) lithiation and (C) delithiation. Si 2*p* spectra are multiplied by numbers indicated in respective spectra for easier comparison. All spectra were obtained using an Al Kα source ($h\nu$ = 1,487 eV). All binding energies were calibrated based on hydrocarbon C 1*s* peak at 285.0 eV.

One may consider that Li can be extracted from the Li silicates by successive lithiation/delithiation cycles. Figure 4 - 6 shows the Li-silicate peaks and their integrations during the first few cycles. The change in the peak integration for the Li-silicate species was negligible, implying that the Li-silicate species were inactive during successive cycles. The peak position and the electrochemical inactivity both suggest that the main Li-silicate component was lithium orthosilicate, Li_4SiO_4.[12, 18]

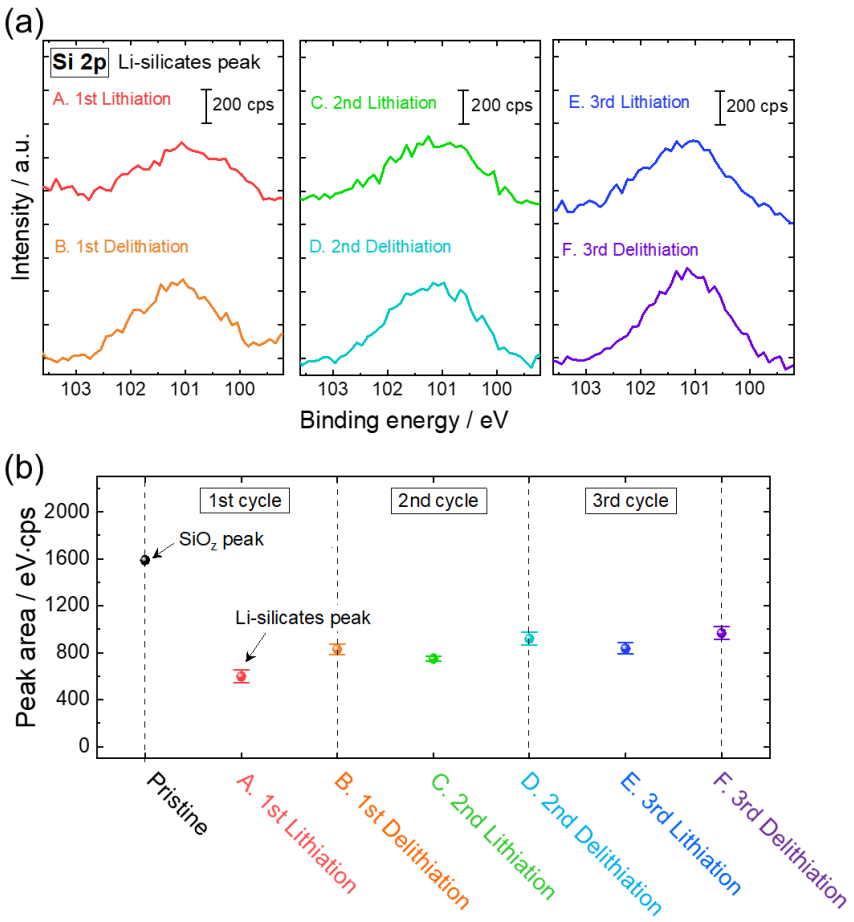

Figure 4 - 6. (a) Photoelectron peaks in Si 2*p* region corresponding to Li silicates and (b) their integrations after each lithiation/delithiation. Data points and error bars represent average of three measurements and standard deviations, respectively.

The O 1*s* peak attributed to the pristine Si electrode (Figure 4 - 5 A) originated from the native suboxide, SiO_z, and contaminating carbonate species adsorbed at the electrode surface. After the lithiation (Figure 4 - 5 B), bimodal peaks attributable to Li_2O[8, 19] and Li_2CO_3/Li silicates[12, 16-18] were observed at 528.8 and 531.4 eV, respectively.

4.2.2.2 Depth analysis using Ag Lα incident x-rays

Because the photon energy of Ag Lα x-rays ($h\nu$ = 2,984 eV) is higher than that of Al Kα ones ($h\nu$ = 1,487 eV), photoelectrons with higher kinetic energy can be expected. Therefore, the utilization of the former enables to detect photoelectrons emitted at the deeper region for in-depth analysis. In addition, core levels which cannot be excited by Al Kα radiation can be excited using such a high-energy x-ray source.

Figures 4 - 7 and 4 - 8 show the wide- and narrow-scan XPS spectra acquired using Al Kα and Ag Lα sources, respectively. As compared to the Al Kα excitation, the ratio of the Li-silicates peak to the Li_xSi peak in the Si 2*p* region was smaller for the Ag Lα excitation (right column in Figure 4 - 8), indicating that the Li silicates were localized on the Si-electrode surface.

In addition, the ratio of the Li_xSi peak to those of other components (i.e., Li_2O and Li silicates/Li_2CO_3) was larger for the Ag Lα excitation, suggesting the formation of Li_2O, Li silicates, and Li_2CO_3 over the Li_xSi.

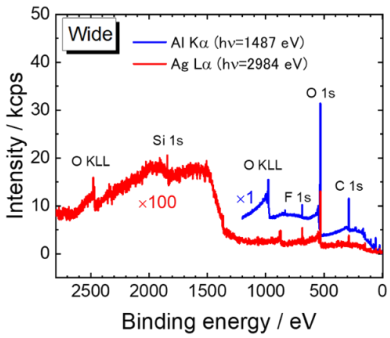

Figure 4 - 7. Wide-scan spectra generated for Si electrode after fifth lithiation. For easier comparison, peak intensity is multiplied by numbers indicated in respective spectra.

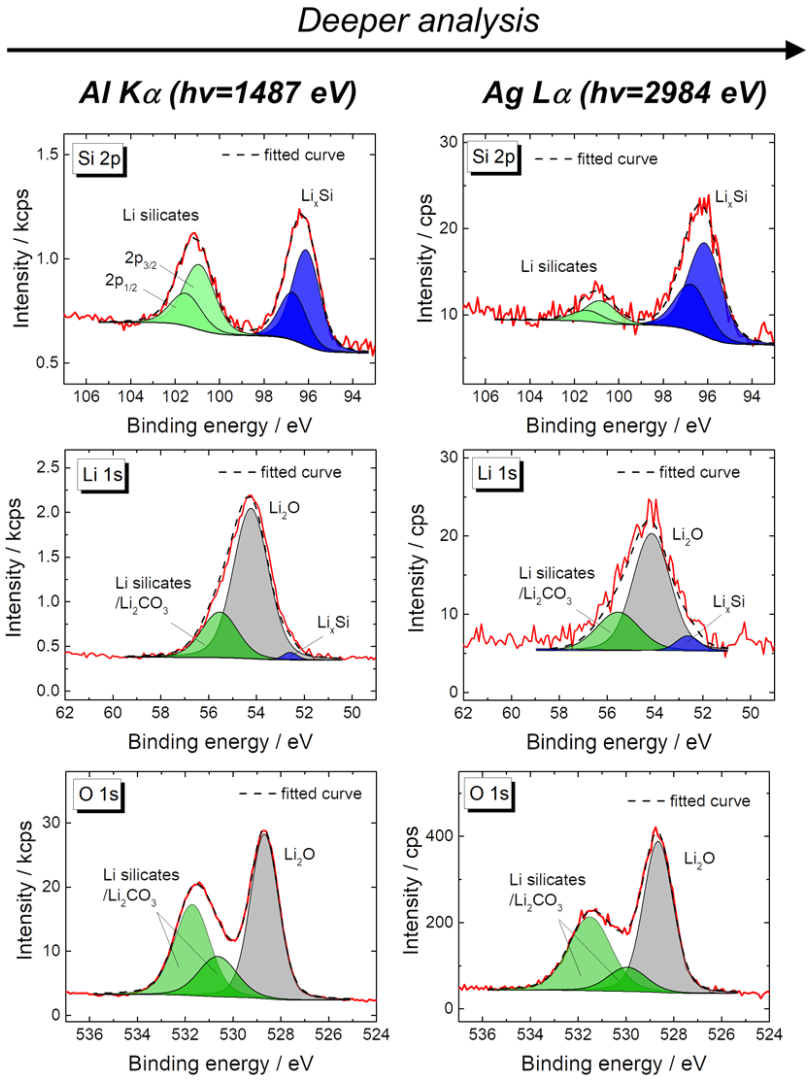

Figure 4 - 8. Si 2*p*, Li 1*s*, and O 1*s* spectra generated for Si electrode after fifth lithiation. Evolution plotted as functions of Al Kα ($h\nu$ = 1,487 eV) and Ag Lα ($h\nu$ = 2,984 eV) incident x-ray photon energies.

Figure 4 - 9 shows the C 1*s* XPS spectra acquired using the Al Kα x-ray source under each electrochemical condition. The intensity of the C 1*s* peaks corresponding to the organic contamination (hydrocarbon; 285 eV) and lithium carbonate (Li_2CO_3; 290 eV) increased after the first lithiation and subsequent cycles, while that of the O 1*s* and Li 1*s* peaks corresponding to Li_2O decreased from the B to C in Figure 4 - 5, implying that Li_2CO_3 was formed by the reaction between of Li_2O formed at outermost layer at B with a trace amount of residual gas in the vacuum chamber.

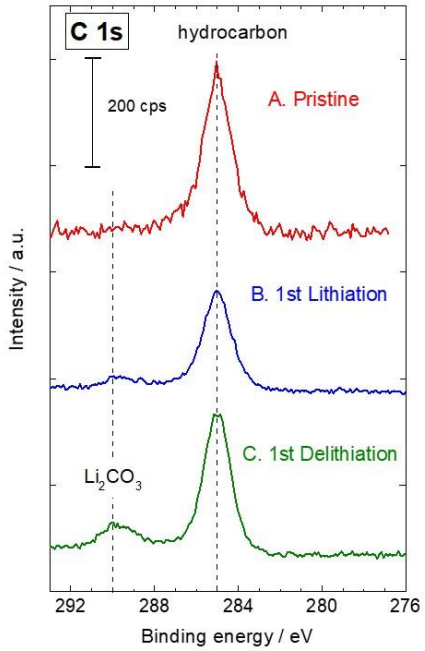

Figure 4 - 9. C 1*s* spectra generated for Si electrode under each electrochemical condition. Dashed lines indicate positions of peaks attributed to Li_2CO_3 and hydrocarbons, respectively.[8] All spectra were obtained using Al Kα incident x-rays. All binding energies were calibrated based on hydrocarbon C 1*s* peak at 285.0 eV.

4.2.2.3 Quantitative estimation of surface layers

Figure 4 - 10 shows the structural models proposed for estimating the thickness of the pristine and lithiated Si-electrode surface layers (from A to B in Figure 4 - 5). The thickness of the Si suboxide (SiO_z; *a*), lithium oxide (Li_2O; *b*), and lithium orthosilicate

(Li_4SiO_4; c) layers was estimated using the peak intensities and known physical parameters such as the inelastic mean free paths and atomic densities.

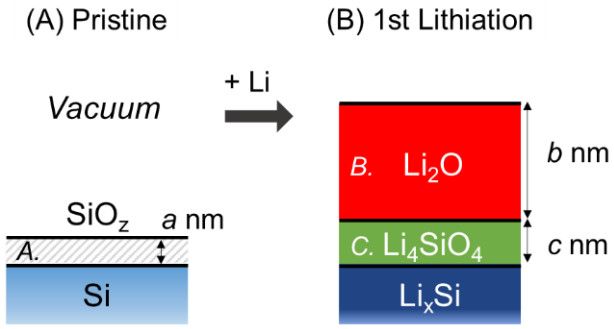

Figure 4 - 10. Structural models proposed for estimating thickness of (A) pristine and (B) lithiated Si-electrode surface layers.

Thickness of SiO_z layer

First, the thickness of the SiO_z layer (a) was determined using the following equation.[20] Here, the SiO_2 physical properties were used for the calculation.

$$a = \lambda_{SiO_2} \ln\left(\frac{n_{Si}}{n_{SiO_2}}\frac{\lambda_{Si}}{\lambda_{SiO_2}}\frac{I_{SiO_2}}{I_{Si}} + 1\right), \qquad (4\text{ -}1)$$

where $\lambda_{SiO_2}(= 3.09\ \text{nm})$ and $\lambda_{Si}\ (= 3.75\ \text{nm})$ are the inelastic mean free paths of the Si $2p$ photoelectrons in SiO_2 and bulk Si, respectively, obtained using the TPP-2M formula;[21] $n_{SiO_2}\ (= 5.00 \times 10^{22}\ \text{atoms/cm}^3)$ and $n_{Si}\ (= 2.28 \times 10^{22}\ \text{atoms/cm}^3)$ are the Si atomic densities of SiO_2 and bulk Si;[22] and $I_{SiO_2}/I_{Si}\ (= 0.073)$ is the intensity ratio of the SiO_z peak to bulk Si peak in the Si $2p$ region.

Thickness of Li_4SiO_4 layer

The appearance of Li-silicate peak and the disappearance of SiO_z peak simultaneously occur (Si $2p$ region in Figure 4 - 5 B), implying that the native oxide (SiO_z) was fully converted to Li_4SiO_4 by lithiation. Hence, the thickness of the Li_4SiO_4 layer (c) was obtained from that of the SiO_2 layer (a) using the volumetric ratio of their

unit cells. According to the densities of Si atoms in SiO_2, ($n_{SiO_2} = 2.28 \times 10^{22}$ atoms/cm^3) and Li_4SiO_4 ($n_{Li_4SiO_4} = 1.21 \times 10^{22}$ atoms/cm^3),[7] the lattice volumetric ratio ($V_{Li_4SiO_4}/V_{SiO_2}$) can be expressed as follows:

$$V_{Li_4SiO_4}/V_{SiO_2} = n_{SiO_2}/n_{Li_4SiO_4},$$

$$V_{Li_4SiO_4}/V_{SiO_2} = 1.88,$$

$$\therefore\ c = 1.88a, \qquad (4\text{ - }2)$$

Thickness of Li_2O layer

According to the discussion that the intensity of the Si 2*p* peaks considerably decreased while strong Li_2O and Li_4SiO_4 peaks simultaneously appeared in Figures 4 - 5 B, the Li_2O and Li_4SiO_4 layers were formed at the outermost layer of the Si electrode. The depth analysis performed using Ag Lα incident x-rays (Figure 4 - 8) also support the formation of Li_2O and Li_4SiO_4 layers at the outermost surface.

The thickness of the Li_2O layer (*b*) (Figure 4 - 10 B) was estimated using the intensities of the Li_2O peak in O 1*s* region $\left(I_{Li_2O,\,O1s}\right)$ and Li_4SiO_4 peak in Si 2*p* region $\left(I_{Li_4SiO_4,\,Si2p}\right)$, respectively, after the first lithiation. The intensity of each peak is expressed as follows:

$$I_{Li_2O,\,O1s} = KI_X\sigma_{O1s}n_{Li_2O,O}\int_0^b \exp\left(-x/\lambda_{Li_2O,O1s}\right)dx$$

$$= KI_X\sigma_{O1s}n_{Li_2O,O}\lambda_{Li_2O,O1s}\left[1-\exp\left(-b/\lambda_{Li_2O,O1s}\right)\right],$$

$$I_{Li_4SiO_4,\,Si2p} = KI_X\sigma_{Si2p}n_{Li_4SiO_4,Si}\exp\left(-b/\lambda_{Li_2O,Si2p}\right)\int_0^c \exp\left(-x/\lambda_{Li_4SiO_4,Si2p}\right)dx$$

$$= KI_X\sigma_{Si2p}n_{Li_4SiO_4,Si}\lambda_{Li_4SiO_4,Si2p}\exp\left(-b/\lambda_{Li_2O,Si2p}\right)\left[1-\exp\left(-c/\lambda_{Li_4SiO_4,Si2p}\right)\right],$$

where K is the detection efficiency of the photoelectrons emitted from the sample, and I_X is the flux of the incident x-rays.

$$\therefore \frac{I_{Li_2O,\,O1s}}{I_{Li_4SiO_4,\,Si2p}} = \frac{\sigma_{O1s}}{\sigma_{Si2p}} \frac{n_{Li_2O,O}}{n_{Li_4SiO_4,Si}} \frac{\lambda_{Li_2O,O1s}}{\lambda_{Li_4SiO_4,Si2p}} \frac{\left[1-\exp\left(-b/\lambda_{Li_2O,O1s}\right)\right]}{\exp\left(-b/\lambda_{Li_2O,Si2p}\right)\left[1-\exp\left(-c/\lambda_{Li_4SiO_4,Si2p}\right)\right]}, \quad (4\text{ -}3)$$

where $I_{Li_2O,\,O1s}/I_{Li_4SiO_4,\,Si2p}$ $(= 46.2)$ is the experimentally obtained peak-intensity ratio; σ_{O1s} $(= 2.93)$ and $\sigma_{Si2p}(= 0.817)$ are the O 1*s* and Si 2*p* photoionization cross-sections;[23] $n_{Li_2O,O}(= 3.98 \times 10^{22}\ \text{atoms/cm}^3)$ and $n_{Li_4SiO_4,Si}(= 1.21 \times 10^{22}\ \text{atoms/cm}^3)$ are the densities of O and Si atoms in Li_2O and Li_4SiO_4, respectively;[24] and $\lambda_{Li_2O,O1s}(= 2.70\ \text{nm})$, $\lambda_{Li_4SiO_4,Si2p}(= 3.40\ \text{nm})$, and $\lambda_{Li_2O,Si2p}$ $(= 3.62\ \text{nm})$ are the inelastic mean free paths of photoelectrons from O 1*s*, Si 2*p*, and Si 2*p* in Li_2O, Li_4SiO_4, and Li_2O,[21] respectively.

According to the equations (4 -1)–(4 -3), thicknesses *a*, *b*, and *c* were obtained to be 0.5, 2.5, and 0.9 nm, respectively. The proposed structural models of the pristine and lithiated Si electrodes are shown in Figure 4 - 11.

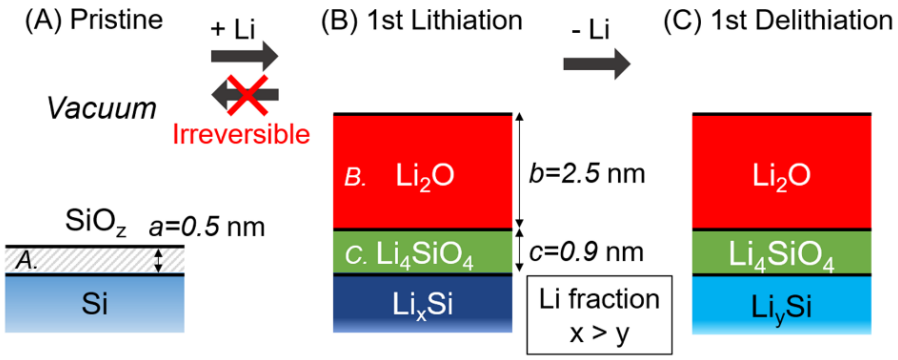

Figure 4 - 11. Proposed structural models of (A) pristine, (B) lithiated, and (C) delithiated Si electrodes. Thickness of each layer was estimated using peak-intensity attenuation ratio and known physical properties.

4.2.2.4 Effect of surface roughness on estimated thickness

Figures 4 - 12 show AFM images of surfaces of the pristine Si electrode and the electrode lithiated tenth times, respectively. The relative surface area (*R*)—(defined as the true surface area divided by the projected one)—of the pristine Si electrode (Figure 4 - 12 (a)) was calculated as 1.03 using Gwyddion 2.56 software.[25] *R* increased to 1.19 after the tenth lithiation (Figure 4 - 12 (b)) and was widely distributed in the range 1.11–1.26 in the projected 20 × 20 μm^2 area owing to the nonuniformly formed cracks and agglomerations, as shown by the red squares in Figure 4 - 12. XPS measurements in the 110 × 110 μm^2 analysis area show the average relative surface area accounting for the nonuniform surface roughness.

Gunter et al.[26, 27] and Werner[28] used Monte Carlo simulations to determine the correlation between *R* obtained for rough Si substrates and SiO_2-overlayer thickness overestimated using angle-resolved XPS. On the basis of their method,[26-28] the thickness of the SiO_z, Li_2O, and Li_4SiO_4 layers (*a*, *b*, and *c* = 0.5, 2.5, and 0.9 nm) could be overestimated by ~10, <~30, and <~30%, respectively.

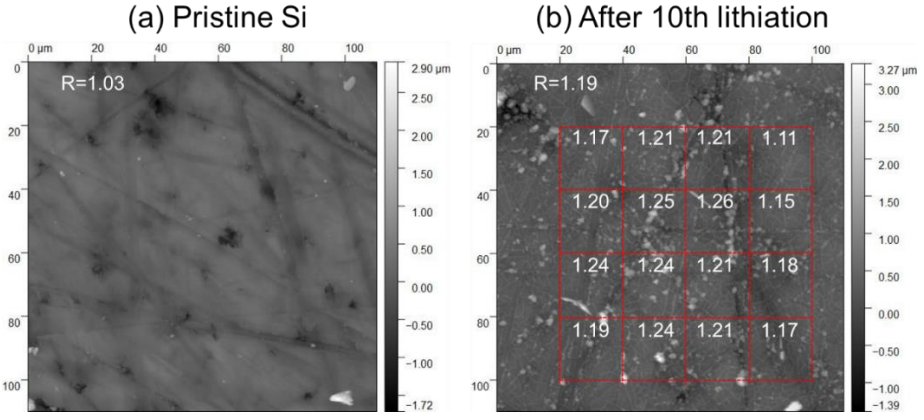

Figure 4 - 12. AFM images of (a) pristine Si-thin-film electrode and (b) Si-thin-film electrode lithiated ten times. Projected 110 × 110 μm^2 area was measured using resolution of 512 × 512 pixels. Area in each red square is 20 × 20 μm^2. *R* values represent relative surface area, defined as true surface area divided by projected one.

4.2.2.5 Formation of irreversible species and their effect on capacity loss

The Li_xSi and Li_ySi compositions were quantified by the thickness experimentally determined using XPS and the lithiation/delithiation electrochemical response. The number of moles of electrons, N_{total}, for the first lithiation (from A to B in Figure 4 - 3) can be represented by the following equation:

$$N_{total} = N_{Li_2O} + N_{Li_4SiO_4} + N_{Li_xSi}, \quad (4 - 4)$$

where N_{Li_2O}, $N_{Li_4SiO_4}$, and N_{Li_xSi} are the number of moles of Li ions used to form Li_2O, Li_4SiO_4, and Li_xSi, respectively. The charge integration for the first lithiation (from A to B in Figure 4 - 3) was 3,330 mAh g^{-1}; thus, N_{total} = 1.75 × 10^{-6} mol. On the basis of the Li_2O- and Li_4SiO_4-layer thicknesses (b = 2.5; c = 0.9 nm), the corresponding Li atomic densities (N_{Li_2O} and $N_{Li_4SiO_4}$) were estimated at 2.10 × 10^{-8} and 4.60 × 10^{-9} mol, respectively. From Equation (4), N_{Li_xSi} was estimated at 1.72 × 10^{-6} mol. Here, the number of moles of Si atoms (5.01 × 10^{-7} mol) in Li_xSi was obtained by subtracting that in the Li_4SiO_4 layer from that in the pristine Si electrode (ϕ9 mm × 95.0 nm); thus, $x \approx 3.44$.

The relationship of the formation of Li_2O and Li_4SiO_4 to the irreversible capacity loss was estimated at approximately 25%.

After the first lithiation, all the subsequent lithiations/delithiations proceeded with approximately 100% coulombic efficiency (as shown in Figure 4 - 4); that is, all the electrical charge was consumed for lithiation (3,137 mAh g^{-1} corresponding to 1.65 × 10^{-6} mol) during delithiation from Li_xSi to Li_ySi (i.e., from B to C in Figure 4 - 3). Thus, y was determined as 0.15.

The estimated capacity and composition in the present research reasonably agree with those determined based on the volumetric change ratio of the Li_xSi layer, as measured using x-ray reflectivity (XRR) and reported by Toney et. al.[29]

4.2.3 Dynamic observation of electrochemical lithiation/delithiation of Si anode

4.2.3.1 Dynamic *in-situ* electrochemical XPS

As mentioned in Section 4.2.2, Li was quasi-reversibly and irreversibly inserted into the Si bulk and native suboxide, respectively, after the lithiation. To further elucidate the lithiation/delithiation mechanism, the first cycle was monitored in a stepwise manner by sequentially generating XPS spectra for each element at the Si-thin-film electrode.

Figure 4 - 13 (a) shows the galvanostatic first lithiation/delithiation potential profiles generated at 0.05 C and cutoff potentials of 1.2 and 0.01 V *vs*. Li^+/Li, respectively. The upper axis of the graph represents the apparent Li content in lithium silicide (Li_xSi), which is calculated based on the integrated electrical charge obtained for the Si lithiation and thickness. For example, the first lithiation and delithiation capacities were 3,342 and 3,162 mAh g^{-1}, and the corresponding apparent Li contents in Li_xSi were 3.50 and 0.19, respectively. In the present experiment, the apparent Li content obtained without calibrating the charge consumed for the irreversible byproducts (Section 4.2.2.3) is shown for simplicity.

To dynamically track lithiation, the following sequential *in-situ* XPS measurements were carried out, as shown in Figure 4 - 13 (b). The sequence consisted of measuring narrow-scan XPS spectra in the Si 2*p* and C, O, and Li 1*s* regions. The total time required to on segment was 0.47 h (28.2 min). In total, spectra were obtained 33 and 31 times during lithiation and delithiation over approximately 15.4 and 14.3 h, respectively. In all the spectra, the binding energy was calibrated using the surface-hydrocarbon C 1*s* peak at 285.0 eV. Because the peak shifted over time, it was used to calibrate all the

other spectra (i.e., Si 2*p* and Li and O 1*s*) after the position of the hydrocarbon peak was linearly extrapolated.

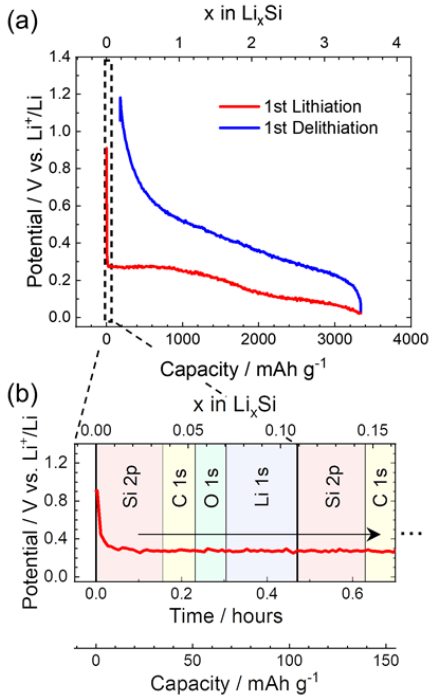

Figure 4 - 13. (a) Galvanostatic lithiation/delithiation potential profiles generated at 0.05 C and cutoff potential in range 0.01–1.2 V *vs.* Li$^+$/Li. (b) Magnified graph of dashed area in (a). Vertical lines indicate acquisition time for XPS spectra.

Figure 4 - 14 (a) shows the time course XPS data obtained in the Li 1*s* region during the lithiation. Although surface-sensitive XPS measurements were applied to starting the other side of the Si/LLZT interface, a broad Li 1*s* peak appeared immediately after starting lithiation (even at the initial acquisition), suggesting the very high Li-diffusivity in Si.[30-31] Furthermore, the Li 1*s* peak was deconvoluted into three major peaks attributed to Li_2CO_3/Li silicates, Li_2O, and Li_xSi at 55.5, 54.1, and 53.6 eV, respectively, when Li content was x = 0.13. In addition, the Li_xSi peak gradually increased in intensity and shifted to lower binding energy up to 52.1 eV after lithiation, as shown in Figure 4 - 14 (b).

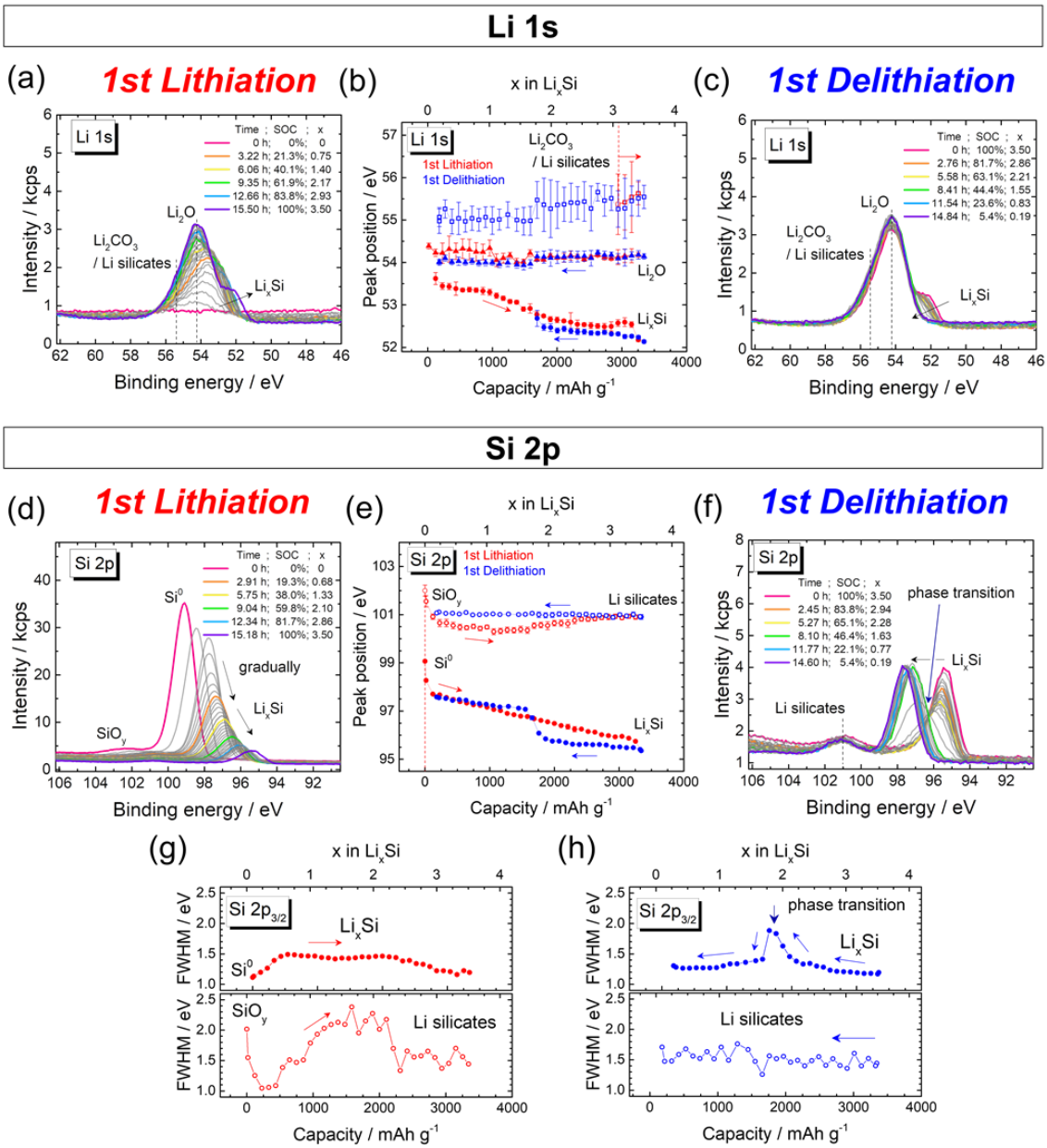

Figure 4 - 14 . Li 1*s* and Si 2*p* spectra generated during (a, d) lithiation and (c, f) delithiation at cutoff potential in range 0.01–1.2 V *vs.* Li^+/Li. Error bars represent uncertainty in peak positions and were set to ±2σ, where σ are standard deviations extracted from curve fitting. (g, h) Full widths at half maximum (FWHMs) of Si 2*p* peaks correspond to Si^0/Li_xSi and SiO_y/Li silicates.

In the subsequent delithiation, the Li_xSi peak at 52.1 eV shifted back to a higher binding energy, indicating decreased Li content (Figures 4 - 14 (b) and (c)).

Furthermore, the Li_xSi peak decreased, and eventually disappeared at a capacity of 1,587 mAh g^{-1} (when $x = 1.66$), as shown in Figure 4 - 14 (c).

Figures 4 - 14 (d)–(f) show the Si 2*p* spectra and the evolution of the peak position during the first lithiation/delithiation. As with the Li 1*s* peak, the bulk Si peak at 99.1 eV shifted to lower binding energy with increasing Li content. The intensity change of the Si^0 peak due to the Li insertion is expected to be ~35.7%. However, it eventually became approximately ~8.3% of the original intensity because of the formation of overlayers such as Li_2O and Li_2CO_3. As shown in Figure 4 - 14 (e), the Li_xSi peak position monotonically decreased with a slope of –0.59 eV/*x* with increase in the Li content, except in the initial and final stages of lithiation (i.e., when $x \approx 0$–0.25 and 3.3–3.5, respectively).

In contrast to the linear relationship between the peak position and Li content, delithiation showed interesting behavior (Figure 4 - 14 (f)). The Li_xSi peak linearly shifted with a slope of –0.23 eV/*x* to a higher binding energy (Li content $x = 3.5$–2.0). Then, the Li_xSi peak drastically shifted from 95.7 to 97.1 eV in the region $x = 2.0$–1.6. When the Li content reached to $x = 1.6$–0.2, it reverted to a linear shift with a slope of –0.35 eV/*x*. Meanwhile, the peak intensity monotonically increased from approximately 2,450 to 2,750 counts per second (cps) owing to the decreased Li content. In addition, the Li_xSi peak broadened in the region where $x = 2.0$–1.6, implying variation in multiple Li_xSi phases. Such drastic changes in the Li_xSi peak in the region where $x = 2.0$–1.6 are attributable to the phase transition from a crystalline $Li_{15}Si_4$ to a single amorphous Li_xSi (where $x < 2.0$). Although the crystalline $Li_{15}Si_4$ structure was preserved up to $x = 2.0$, the coexisting amorphous Li_xSi was preferentially delithiated, thereby gently shifting

the Li_xSi peak (when Li content x = 3.5–2.0). The peak sharpening at approximately x = 1.6 is attributable to the completion of the phase transition.

The Li content at which the amorphization of crystalline $Li_{15}Si_4$ occurred is in good agreement with the previously reported values determined by different techniques.[32-33] Li and Dahn found the amorphization at Li content $x \approx 2$ during a biphasic lithiation/delithiation by using *in-situ* XRD.[32] Furthermore, Gauthier et al. used *ex-situ* electron energy-loss spectroscopy (EELS) to show that crystalline $Li_{15}Si_4$ was replaced by amorphous Li_xSi when $x \approx 2 \pm 0.3$ in Si-based nanocomposite electrodes.[33]

Figures 4 - 15 (a) and (c) show the Si 2*p* spectra generated for the first lithiation and delithiation at a cutoff potential of 0.09 V *vs.* Li^+/Li for lithiation, which is more positive than the regular measurements (0.01 V *vs.* Li^+/Li), to reduce the amount of Li insertion. In the lithiation, the Li_xSi peak monotonically shifted to a 96.1 eV energy with increasing Li content (Figure 4 - 15 (b)), as is the case of a cutoff potential of 0.01 V *vs.* Li^+/Li (Figure 4 - 14 (d)). However, the drastic changes corresponding to the phase transition was absent, suggesting that the phase transition does not occur when the Li insertion was stopped at certain level.

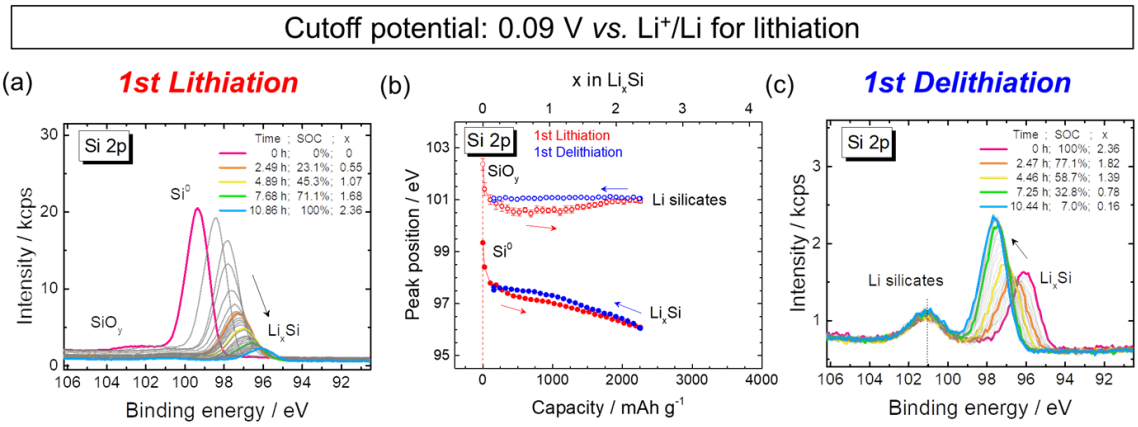

Figure 4 - 15. Si 2*p* spectra generated during first (a) lithiation and (c) delithiation at cutoff potential in range 0.09–1.2 V *vs.* Li^+/Li. (b) Evolution of peak position determined using curve fitting analysis.

Figure 4 - 16 shows the first lithiation/delithiation potential profiles and corresponding differential capacity (dQ/dV) curves generated at cutoff potentials of 0.01 and 0.09 V *vs*. Li^+/Li for lithiation. The curves for the negative and positive dQ/dV regions were obtained from the smoothed lithiation and delithiation potential profiles (i.e., black curves in Figure 4 - 16 (a)), respectively. The delithiation dQ/dV curves measured with a cut off potential of 0.09 V (bottom of Figures 4 – 16) showed broad peaks corresponding to the delithiation of Li-rich and -poor amorphous Li_xSi at approximately 0.29 and 0.49 V, respectively.[34-35]

Besides the two peaks in the dQ/dV curves with a cutoff potential of 0.09 V *vs*. Li^+/Li, an additional peak was observed at approximately 0.41 V *vs*. Li^+/Li in the delithiation dQ/dV curve with a cutoff potential of 0.01 V *vs*. Li^+/Li (top of Figures 4 - 16). Hatchard et al. found a similar peak. They attributed it to the phase transition of crystalline $Li_{15}Si_4$ to amorphous Li_xSi using XRD.[36] The potential at 0.41 V *vs*. Li^+/Li is indeed consistent with that of drastic change of the Si 2*p* peak corresponding to the phase transition (Figure 4 - 14 (f)).

The dQ/dV peaks at 0.29 and 0.41 V attributable to the delithiation of amorphous Li_xSi and the amorphization of crystalline $Li_{15}Si_4$ suggest that the crystalline $Li_{15}Si_4$ was formed during the first lithiation (~0.01 V *vs*. Li/Li^+). In addition, delithiation followed a biphasic reaction between amorphous Li_xSi and crystalline $Li_{15}Si_4$ up to approximately 0.41 V.

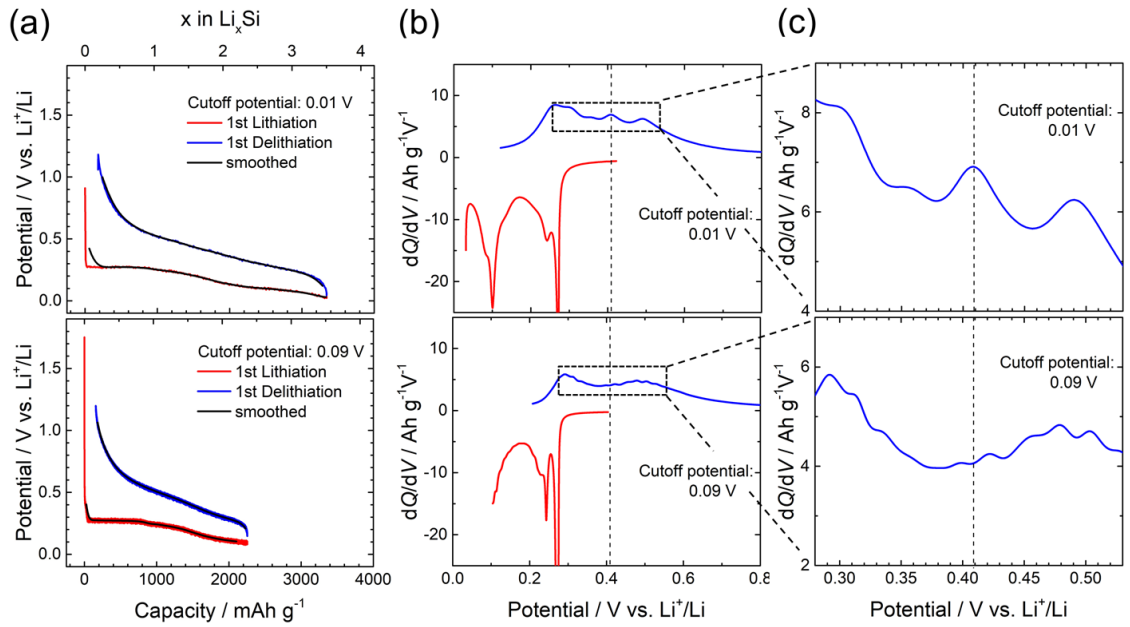

Figure 4 - 16. (a) Galvanostatic first lithiation/delithiation potential profiles and (b) corresponding differential capacity (d*Q*/d*V*) curves generated for Si/LLZT/Li thin-film cells. Lithiation cutoff potentials were set at (top) 0.01 and (bottom) 0.09 V *vs.* Li$^+$/Li. (c) Magnified graph of dashed box shown in (b). Vertical dashed line represents peak position corresponding to amorphization of crystalline $Li_{15}Si_4$.

4.2.3.2 X-ray diffraction

The formation of crystalline $Li_{15}Si_4$, which was indicated by d*Q*/d*V* analysis (Figures 4 - 16), was investigated by the *ex-situ* grazing-incidence X-ray diffraction (GIXRD). Figure 4 - 17 (a) shows the GIXRD patterns generated at an incidence of 0.25° for the Si thin-film electrodes deposited on either a SUS (stainless steel) substrate or a LLZT solid-electrolyte sheet, as shown in the inset of Figure 4 - 17 (a).

The GIXRD pattern of the Si thin-film on the SUS substrate (blue) showed broad peaks at $2\theta \approx 30$ and 53°, corresponding to amorphous Si. However, the GIXRD pattern of the Si thin-film on the LLZT substrate before (green) and after 10

lithiation/delithiation cycles (red) did not show any peaks attributable to either Si or Li_xSi.

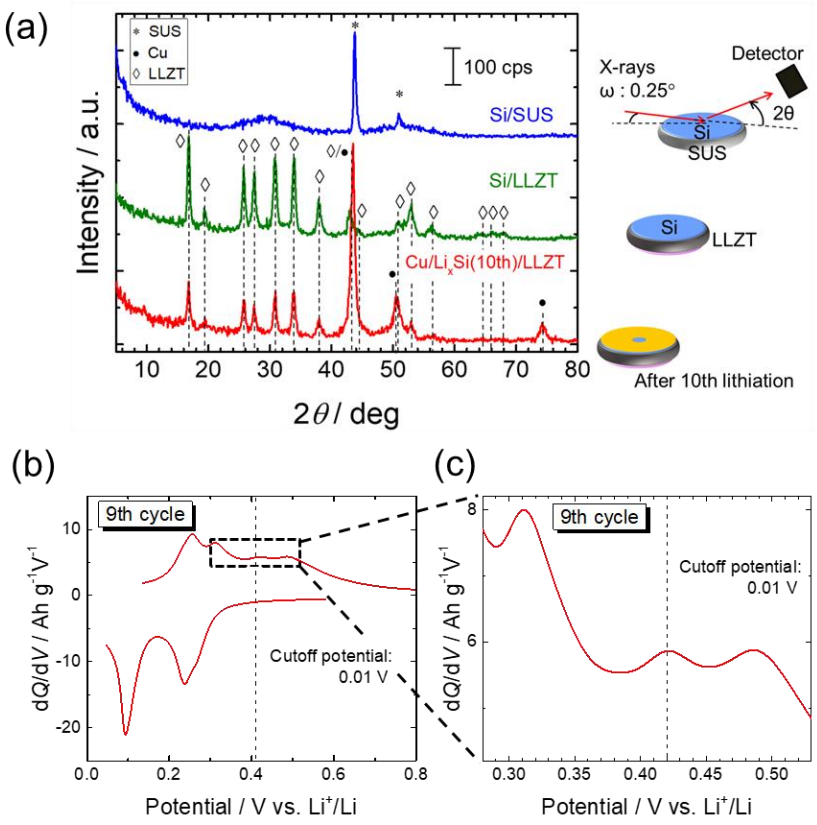

Figure 4 - 17. (a) *Ex-situ* grazing-incidence x-ray diffraction patterns generated for amorphous Si films deposited on either SUS substrate (Si/SUS) or LLZT solid-electrolyte sheet (Si/LLZT) and for Si-thin-film electrode deposited on LLZT sheet and lithiated ten times at cutoff potential in range 0.01–1.2 V *vs.* Li^+/Li ($Cu/Li_xSi/(10th)/LLZT$). Inset presents configuration used for measurements. (b) d*Q*/d*V* curve generated in ninth cycle of $Cu/Li_xSi/(10th)/LLZT$ measurement sample. (c) Magnified graph of dashed box shown in (b). Vertical dashed line represents peak position corresponding to formation of crystalline $Li_{15}Si_4$.

Figures 4 - 17 (b) and (c) show the corresponding d*Q*/d*V* curves generated in the previous (i.e., ninth) lithiation cycle for the Si thin-film electrode used for the GIXRD measurements. Although the small d*Q*/d*V* peak at approximately 0.42 V indicates

crystalline $Li_{15}Si_4$, the GIXRD measurements (red in Figure 4 - 17 (a)) did not show any peaks attributable to $Li_{15}Si_4$, implying that the crystalline-$Li_{15}Si_4$ phase was too small. According to the previous report, the XRD peaks can be obtained if the crystalline size is more than a few nm.[37] The strong peaks originating from the cubic phase of the LLZT garnet structure (ICSD#83607)[38] hindered the identification of those originating from the Si thin film.

The first lithiation/delithiation cycle of the bulk Si^0 can be described as shown in Figure 4 - 18; that is, (1) and (2) a Li was inserted into the amorphous bulk Si, and amorphous Li_xSi was formed. (3) By increasing the amount of inserted Li, crystalline $Li_{15}Si_4$ was formed in the range of $Li_{2.0}Si$ ~ $Li_{1.6}Si$, producing coexistence of amorphous Li_xSi and crystalline $Li_{15}Si_4$. (4) Li was extracted from the amorphous Li_xSi when x = 3.5–2.0 in the subsequent biphasic delithiation. (5) The crystalline $Li_{15}Si_4$ was transformed into amorphous $Li_{15}Si_4$ when $x \approx$ 2.0–1.6, thereby becoming a single amorphous Li_xSi phase. (6) After the phase transition, delithiation proceeded by a single-phase reaction in the amorphous Li_xSi. The relatively wide transition state (where Li content x = 2.0–1.6) is considered to be due to the nonuniform potential distribution in the Si electrode.

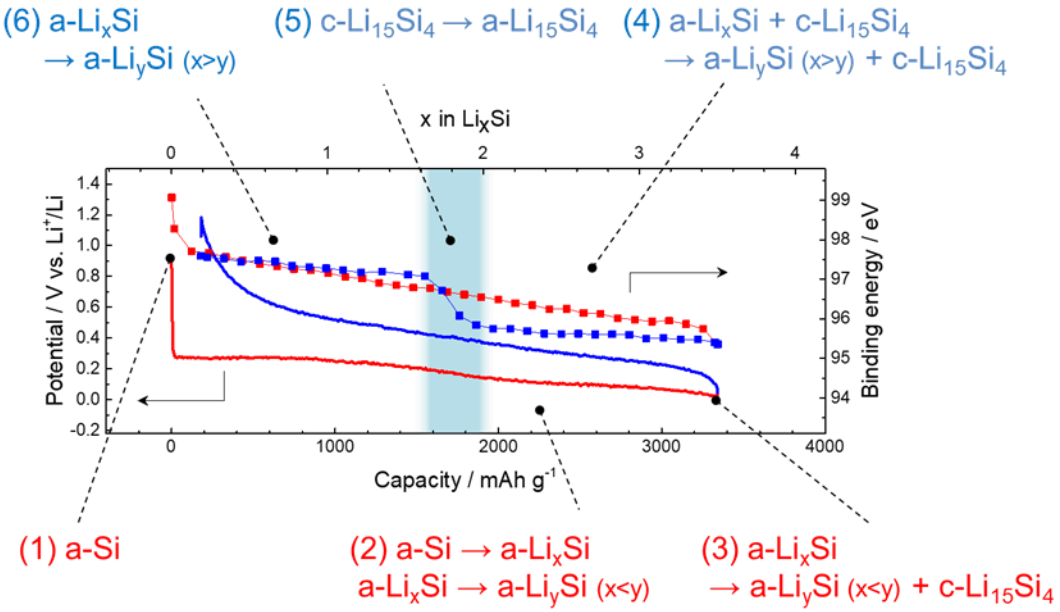

Figure 4 - 18. Galvanostatic first lithiation/delithiation potential profiles and binding energy of Li_xSi Si 2*p* peaks plotted as functions of capacity and Li content in Li_xSi. (a = amorphous; c = crystalline). Blue shaded area represents region where crystalline $Li_{15}Si_4$ amorphized in delithiation. Insets represent reactions in each process described in main text.

4.2.3.3 Formation mechanism of surface layers

The formation mechanism of Li silicates, Li_2O, and Li_2CO_3 was also investigated. The full width at half maximum (FWHM) of the SiO_y/Li silicate peaks considerably varied up to approximately 2,300 mAh g^{-1} (x = 2.4 for Li_xSi) in the first lithiation (Figure 4 - 14 (g)). However, that of the Li-silicate peaks only negligibly changed in the subsequent delithiation (bottom of Figure 4 - 14 (h)). Moreover, the O 1*s* peaks at 528.7 and 531.4 eV, corresponding to Li_2O and Li_2CO_3/Li silicates, respectively, appeared in the early stage of lithiation (~1,000 mAh g^{-1} and $x \approx 1$ in Li_xSi), as shown in Figure 4 - 19 (a). The C 1*s* spectra also showed the formation of Li_2CO_3 when $x \approx 3.0$ (Figures 4 - 19 (a) and (b)). The peaks attributed to the Li silicates, Li_2O, and Li_2CO_3 were identical

during the subsequent delithiation, confirming that these species were electrochemically inactive.

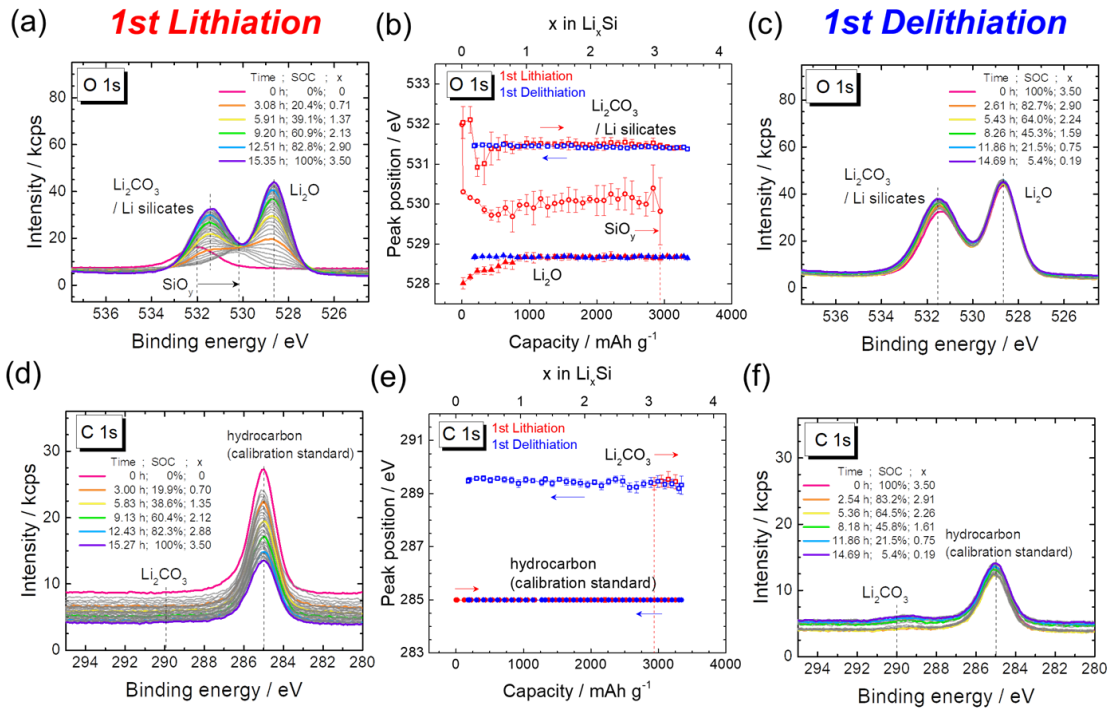

Figure 4 - 19. O and C 1*s* spectra generated during the first (a) lithiation and (c) delithiation. (b) Evolution of peak position was determined using curve-fitting analysis.

4.2.3.4 Volumetric expansion of Si anode monitored using *in-situ* AFM during first lithiation

The changes in the thickness and nanomechanical properties of the Si-thin-film electrode were monitored using *in-situ* AFM during the first lithiation. The change in the height of the thin-film cell (ΔZ_{cell}), was measured by monitoring the *z*-position of the piezo scanner. The ΔZ_{cell} can be represented by the following equation:

$$\Delta Z_{cell} = \Delta Z_{Si} + \Delta Z_{Li}, \qquad (4 - 5)$$

where ΔZ_{Si} and ΔZ_{Li} are the changes in the thickness of the Si electrode and metallic

Li layer deposited on another LLZT surface, respectively. The ΔZ_{Li} can be calculated from charge integration (blue curve in Figure 4 - 20 (b)).

Figures 4 - 20 (a) and (b) show the galvanostatic potential profile generated in the lithiation and the corresponding changes in ΔZ_{cell}, respectively. However, the ΔZ_{cell} exhibited a large error in an open-circuit-voltage state (red curve in Figure 4 - 20 (b)), possibly owing to thermal drift. This large error hindered the quantitative analysis of the changes in the thickness.

Force–distance curves were generated at various electrochemical states, as shown in Figure 4 - 20 (d). The corresponding AFM images are also shown in Figure 4 - 20 (e). The slope of the force–distance curve (ΔF/ΔD) steepened with increasing lithiation time, suggesting that the Si electrode surface became softer with the formation of Li_xSi, Li silicates, and Li_2O.[39]

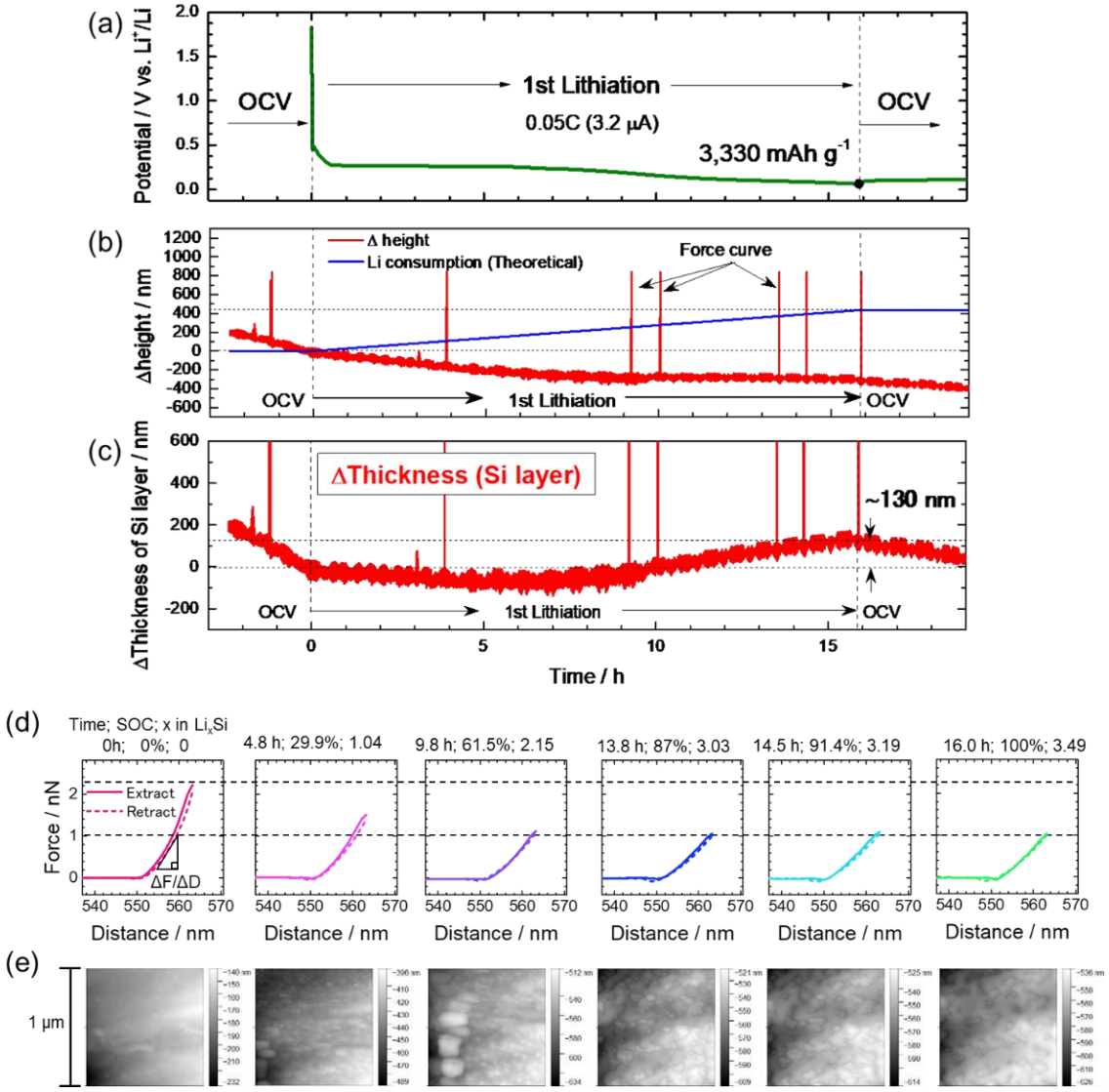

Figure 4 - 20. (a) Galvanostatic potential profile generated in the first lithiation at 0.05 C. (b) Changes in height of thin-film cell (red) measured by monitoring piezo scanner, and estimated changes in thickness of metallic Li layer (blue) deposited on counter electrode. (c) Estimated thickness evolution of Si-thin-film electrode. (d) Force–distance curves generated utilizing Si probe showing 40-N/m spring contact at various electrochemical states. Extraction and retraction scan rates were both 1 Hz. Deflection sensitivity of 0.073 nm/mV and Q factor of 386 were used to convert cantilever amplitude into contact force plotted on *y*-axis. (e) Representative AFM images. Projected area (1 × 1 μm) was measured using resolution of 256 × 256 pixels and scanned at 0.2 Hz.

4.3 Conclusions

In conclusion, we investigated the lithiation/delithiation of an amorphous Si electrode in a thin-film-cell configuration by *in-situ* XPS, AFM, and electrochemical analysis. A quasi-reversible shift in the Si 2*p* peak corresponding to the lithiation/delithiation of the Si and the formation of irreversible species such as Li silicates, Li_2O, and Li_2CO_3 were observed, as shown in Figure 4 - 21. The irreversible-species-containing surface layers, the lithium-silicide concentration, and the Li_2O- and Li_4SiO_4-formation-induced contribution to the capacity loss were quantitatively analyzed. In addition, the drastic shift in the Li_xSi peak originating from the amorphization of the crystalline $Li_{15}Si_4$ formed when Li was inserted in to Li_xSi up to x = 3.5 was dynamically observed at Li content x = 2.0–1.6 (in Li_xSi) in delithiation. Furthermore, the surface of Si electrode in the first lithiation was observed using AFM.

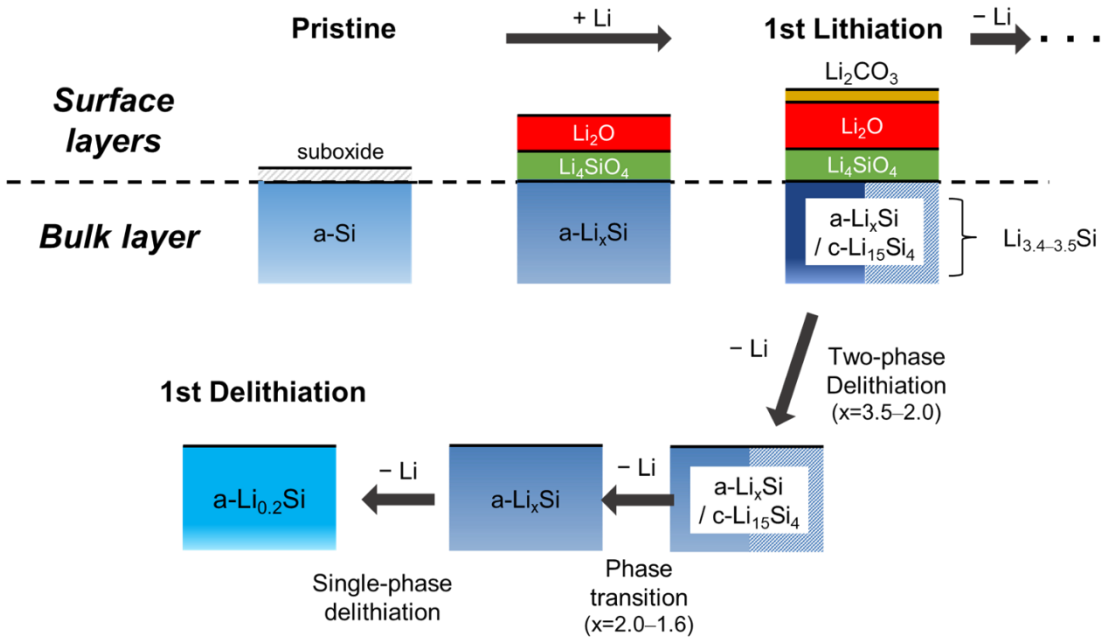

Figure 4 - 21. Schematic illustrating first lithiation/delithiation.

References

1. Chen, C.; Li, Q.; Li, Y.; Cui, Z.; Guo, X.; Li, H., Sustainable interfaces between Si anodes and garnet electrolytes for room-temperature solid-state batteries. *ACS Appl. Mater. Interfaces* **2018,** *10* (2), 2185-2190.
2. Sakabe, J.; Ohta, N.; Ohnishi, T.; Mitsuishi, K.; Takada, K., Porous amorphous silicon film anodes for high-capacity and stable all-solid-state lithium batteries. *Commun. Chem.* **2018,** *1* (1), 24.
3. Porz, L.; Swamy, T.; Sheldon, B. W.; Rettenwander, D.; Frömling, T.; Thaman, H. L.; Berendts, S.; Uecker, R.; Carter, W. C.; Chiang, Y.-M., Mechanism of Lithium Metal Penetration through Inorganic Solid Electrolytes. *Adv. Energy Mater.* **2017,** *7* (20), 1701003.
4. LePage, W. S.; Chen, Y.; Kazyak, E.; Chen, K.-H.; Sanchez, A. J.; Poli, A.; Arruda, E. M.; Thouless, M. D.; Dasgupta, N. P., Lithium Mechanics: Roles of Strain Rate and Temperature and Implications for Lithium Metal Batteries. *J. Electrochem. Soc.* **2019,** *166* (2), A89-A97.
5. Yamamoto, M.; Terauchi, Y.; Sakuda, A.; Kato, A.; Takahashi, M., Effects of volume variations under different compressive pressures on the performance and microstructure of all-solid-state batteries. *J. Power Sources* **2020,** *473*, 228595.
6. Ohta, N.; Kimura, S.; Sakabe, J.; Mitsuishi, K.; Ohnishi, T.; Takada, K., Anode properties of Si nanoparticles in all-solid-state Li batteries. *ACS Appl. Energy Mater.* **2019,** *2* (10), 7005-7008.
7. Dejong, B.; Ellerbroek, D.; Spek, A. L., Low-temperature structure of lithium nesosilicate, Li_4SiO_4, and its Li 1s and O 1s X-ray photoelectron spectrum. *Acta Crystallogr. Sect. B-Struct. Commun.* **1994,** *50*, 511-518.
8. Kanamura, K.; Takezawa, H.; Shiraishi, S.; Takehara, Z., Chemical reaction of lithium surface during immersion in $LiClO_4$ or $LiPF_6$/DEC electrolyte. *J. Electrochem. Soc.* **1997,** *144* (6), 1900-1906.
9. Shen, C.; Fu, R.; Xia, Y.; Liu, Z., New perspective to understand the effect of electrochemical prelithiation behaviors on silicon monoxide. *RSC Adv.* **2018,** *8* (26), 14473-14478.
10. Sharafi, A.; Yu, S.; Naguib, M.; Lee, M.; Ma, C.; Meyer, H. M.; Nanda, J.; Chi, M.; Siegel, D. J.; Sakamoto, J., Impact of air exposure and surface chemistry on Li–$Li_7La_3Zr_2O_{12}$ interfacial resistance. *J. Mater. Chem. A* **2017,** *5* (26), 13475-13487.
11. Liu, X. H.; Wang, J. W.; Huang, S.; Fan, F.; Huang, X.; Liu, Y.; Krylyuk, S.; Yoo, J.; Dayeh, S. A.; Davydov, A. V.; Mao, S. X.; Picraux, S. T.; Zhang, S.; Li, J.; Zhu, T.; Huang, J. Y., In situ atomic-scale imaging of electrochemical lithiation in silicon. *Nat. Nanotechnol.* **2012,** *7*, 749.
12. Philippe, B.; Dedryvère, R.; Allouche, J.; Lindgren, F.; Gorgoi, M.; Rensmo, H.; Gonbeau, D.; Edström, K., Nanosilicon Electrodes for Lithium-Ion Batteries: Interfacial Mechanisms Studied by Hard and Soft X-ray Photoelectron Spectroscopy. *Chem. Mater.* **2012,** *24* (6), 1107-1115.
13. Grunthaner, P. J.; Hecht, M. H.; Grunthaner, F. J.; Johnson, N. M., The localization and

crystallographic dependence of Si suboxide species at the SiO_2/Si interface. *J. Appl. Phys.* **1987,** *61* (2), 629-638.

14. Yu, B. C.; Hwa, Y.; Park, C. M.; Sohn, H. J., Reaction mechanism and enhancement of cyclability of SiO anodes by surface etching with NaOH for Li-ion batteries. *J. Mater. Chem. A* **2013,** *1* (15), 4820-4825.
15. Radvanyi, E.; De Vito, E.; Porcher, W.; Larbi, S. J. S., An XPS/AES comparative study of the surface behaviour of nano-silicon anodes for Li-ion batteries. *J. Anal. At. Spectrom.* **2014,** *29* (6), 1120-1131.
16. Guo, B.; Shu, J.; Wang, Z.; Yang, H.; Shi, L.; Liu, Y.; Chen, L., Electrochemical reduction of nano-SiO_2 in hard carbon as anode material for lithium ion batteries. *Electrochem. Commun.* **2008,** *10* (12), 1876-1878.
17. Cao, C.; Abate, I. I.; Sivonxay, E.; Shyam, B.; Jia, C.; Moritz, B.; Devereaux, T. P.; Persson, K. A.; Steinrück, H.-G.; Toney, M. F., Solid Electrolyte Interphase on Native Oxide-Terminated Silicon Anodes for Li-Ion Batteries. *Joule* **2019,** *3* (3), 762-781.
18. Miyachi, M.; Yamamoto, H.; Kawai, H.; Ohta, T.; Shirakata, M., Analysis of SiO Anodes for Lithium-Ion Batteries. *J. Electrochem. Soc.* **2005,** *152* (10), A2089-A2091.
19. Tanaka, S.; Taniguchi, M.; Tanigawa, H., XPS and UPS studies on electronic structure of Li2O. *J. Nucl. Mater.* **2000,** *283-287*, 1405-1408.
20. Strohmeier, B. R., An ESCA method for determining the oxide thickness on aluminum alloys. *Surf. Interface Anal.* **1990,** *15* (1), 51-56.
21. Tanuma, S.; Powell, C. J.; Penn, D. R., Calculation of electron inelastic mean free paths (IMFPs) VII. Reliability of the TPP-2M IMFP predictive equation. *Surf. Interface Anal.* **2003,** *35* (3), 268-275.
22. Himpsel, F. J.; McFeely, F. R.; Talebibrahimi, A.; Yarmoff, J. A.; Hollinger, G., Microscopic structure of the SiO_2/Si interface. *Phys. Rev. B* **1988,** *38* (9), 6084-6096.
23. Scofield, J. H., Hartree-Slater subshell photoionization cross-sections at 1254 and 1487 eV. *J. Electron. Spectrosc. Relat. Phenom.* **1976,** *8* (2), 129-137.
24. Yao, K. P. C.; Kwabi, D. G.; Quinlan, R. A.; Mansour, A. N.; Grimaud, A.; Lee, Y.-L.; Lu, Y.-C.; Shao-Horn, Y., Thermal Stability of Li_2O_2 and Li_2O for Li-Air Batteries: In Situ XRD and XPS Studies. *J. Electrochem. Soc.* **2013,** *160* (6), A824-A831.
25. Nečas, D.; Klapetek, P., Gwyddion: an open-source software for SPM data analysis. *Open Physics* **2012,** *10* (1), 181.
26. Gunter, P. L. J.; Niemantsverdriet, J. W., Thickness determination of uniform overlayers on rough substrates by angle-dependent XPS. *Appl. Surf. Sci.* **1995,** *89* (1), 69-76.
27. Gunter, P. L. J.; Gijzeman, O. L. J.; Niemantsverdriet, J. W., Surface roughness effects in quantitative XPS: magic angle for determining overlayer thickness. *Appl. Surf. Sci.* **1997,** *115* (4), 342-346.

28. Werner, W. S. M., Magic angle for surface roughness for intensity ratios in AES/XPS. *Surf. Interface Anal.* **1995,** *23* (10), 696-704.
29. Steinrück, H.-G.; Cao, C.; Veith, G. M.; Toney, M. F., Toward quantifying capacity losses due to solid electrolyte interphase evolution in silicon thin film batteries. *J. Chem. Phys.* **2020,** *152* (8), 084702.
30. Yoshimura, K.; Suzuki, J.; Sekine, K.; Takamura, T., Evaluation of the Li insertion/extraction reaction rate at a vacuum-deposited silicon film anode. *J. Power Sources* **2005,** *146* (1), 445-447.
31. Ding, N.; Xu, J.; Yao, Y. X.; Wegner, G.; Fang, X.; Chen, C. H.; Lieberwirth, I., Determination of the diffusion coefficient of lithium ions in nano-Si. *Solid State Ionics* **2009,** *180* (2), 222-225.
32. Li, J.; Dahn, J. R., An In Situ X-Ray Diffraction Study of the Reaction of Li with Crystalline Si. *J. Electrochem. Soc.* **2007,** *154* (3), A156.
33. Gauthier, M.; Danet, J.; Lestriez, B.; Roué, L.; Guyomard, D.; Moreau, P., Nanoscale compositional changes during first delithiation of Si negative electrodes. *J. Power Sources* **2013,** *227*, 237-242.
34. Obrovac, M. N.; Krause, L. J., Reversible Cycling of Crystalline Silicon Powder. *J. Electrochem. Soc.* **2007,** *154* (2), A103-A108.
35. Chevrier, V. L.; Liu, L.; Le, D. B.; Lund, J.; Molla, B.; Reimer, K.; Krause, L. J.; Jensen, L. D.; Figgemeier, E.; Eberman, K. W., Evaluating Si-Based Materials for Li-Ion Batteries in Commercially Relevant Negative Electrodes. *J. Electrochem. Soc.* **2014,** *161* (5), A783-A791.
36. Hatchard, T. D.; Dahn, J. R., In Situ XRD and Electrochemical Study of the Reaction of Lithium with Amorphous Silicon. *J. Electrochem. Soc.* **2004,** *151* (6), A838.
37. O'Connell, K.; Regalbuto, J. R., High Sensitivity Silicon Slit Detectors for 1 nm Powder XRD Size Detection Limit. *Catal. Lett.* **2015,** *145* (3), 777-783.
38. Inada, R.; Okada, T.; Bando, A.; Tojo, T.; Sakurai, Y., Properties of garnet-type $Li_6La_3ZrTaO_{12}$ solid electrolyte films fabricated by aerosol deposition method. *Prog. Nat. Sci.* **2017,** *27* (3), 350-355.
39. Zinn, A. H.; Borhani-Haghighi, S.; Ventosa, E.; Pfetzing-Micklich, J.; Wieczorek, N.; Schuhmann, W.; Ludwig, A., Mechanical properties of $SiLi_x$ thin films at different stages of electrochemical Li insertion. *Phys. Status Solidi A* **2014,** *211* (11), 2650-2656.

Chapter 5. Long-term cycle performance and capacity fading of Si-thin-film electrodes

5.1 Introduction

In Chapter 4, the initial stages of lithiation/delithiation were explored for amorphous-Si thin-film electrodes. The reversible change in the composition of lithium silicide (Li_xSi), the formation of irreversible species including lithium silicates (Li silicates), lithium oxide (Li_2O), and lithium carbonate (Li_2CO_3), and the related phase transitions were quantitatively analyzed based on the surface composition and state of charge (SOC) estimated by XPS and the electrochemical response, respectively.

In the present Chapter, those reactions were correlated to the long-term cycle performance. The lithiation/delithiation of a Si-thin-film electrode was tracked using *in-situ* XPS in long-term cycling. The causes of the capacity fading in the amorphous-Si thin-film cell were discussed based on the surface composition and differential capacity (dQ/dV) curves.

5.2 Results and Discussion

5.2.1 Long-term cycle performance

As described in Chapter 4, the crystalline $Li_{15}Si_4$ formed at the end of lithiation leads to the phase transition from crystalline $Li_{15}Si_4$ to amorphous $Li_{2.0–1.6}Si$ during biphasic delithiation. Previously reported first-principles calculations have shown that the phase transition from crystalline $Li_{15}Si_4$ to amorphous $Li_{2.0}Si$ causes a large volumetric change

of −37%, resulting fracturing due to high internal stress.[1] Fracturing of Si particles due to the phase transition was also found by an acoustic emission.[2]

Differential capacity (dQ/dV) curves and XPS results show that crystalline $Li_{15}Si_4$ is formed during lithiation up to a cutoff potential of 0.01 V *vs*. Li^+/Li and $Li_{15}Si_4$ transforms to amorphous $Li_{2.0–1.6}Si$ at approximately 0.42 V *vs*. Li^+/Li in the subsequent delithiation (Figures 4 - 14 and 16). However, crystalline $Li_{15}Si_4$ was not formed when lithiation stopped at 0.09 V *vs*. Li^+/Li. To begin with, the effect of the phase transition on the cycle performance was evaluated.

Figure 5 - 1 shows the performance of Si thin-film cells cycled up to 100 times at cutoff potentials of 0.01 (blue) and 0.09 V *vs*. Li^+/Li (pink). At the cutoff potential of 0.01 V *vs*. Li^+/Li (blue), the reversible capacity decayed relatively quickly. The capacity retention at the 100th lithiation was only 65.6% of that at the 10th lithiation. On the other hand, the thin-film cell cycled at the cutoff potential of 0.09 V *vs*. Li^+/Li (pink) exhibited a better cycle performance. The capacity retention at the 100th lithiation was 77.5% of that at the 10th lithiation.

Thus, the relatively rapid capacity fading at the cutoff potential of 0.01 V *vs*. Li^+/Li (blue) can be attributed to the formation of crystalline $Li_{15}Si_4$ in lithiation and the phase transition from $Li_{15}Si_4$ to amorphous $Li_{2.0–1.6}Si$ in delithiation.

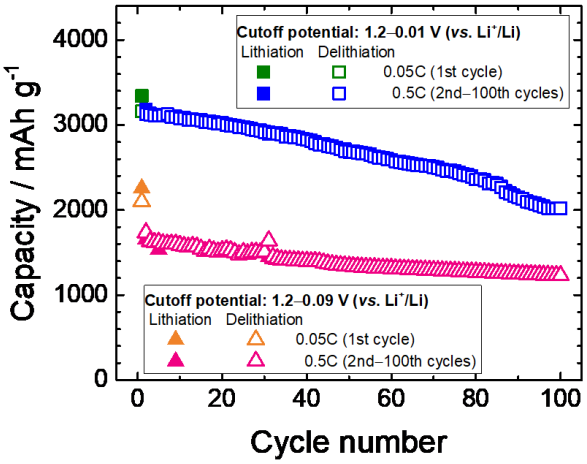

Figure 5 - 1. Comparison of long-term cycle performances at cutoff potential of 0.01 (green and blue) and 0.09 V *vs.* Li^+/Li (orange and pink). C-rate was set to 0.05 C in the first cycle and 0.5 C in other cycles.

5.2.2 Dynamic observation of long-term cycling

Figures 5 - 2 (a) and (b) show the galvanostatic lithiation/delithiation potential profiles generated at 0.5 C and cutoff potentials in the range 1.2–0.01 V *vs*. Li^+/Li and the *in-situ* XPS sequence, respectively. The sequence is composed of generating Si 2*p*, C 1*s*, O 1*s*, and Li 1*s* spectra, and the total time required to acquire one complete series of measurements was approximately 0.28 h (16.8 min). Therefore, the spectra were acquired approximately 8 and 7 times during the 2nd lithiation and delithiation, respectively. Because of capacity fading, the number of the acquisitions decreased to 6 and 5 times at the 100th lithiation and delithiation, respectively.

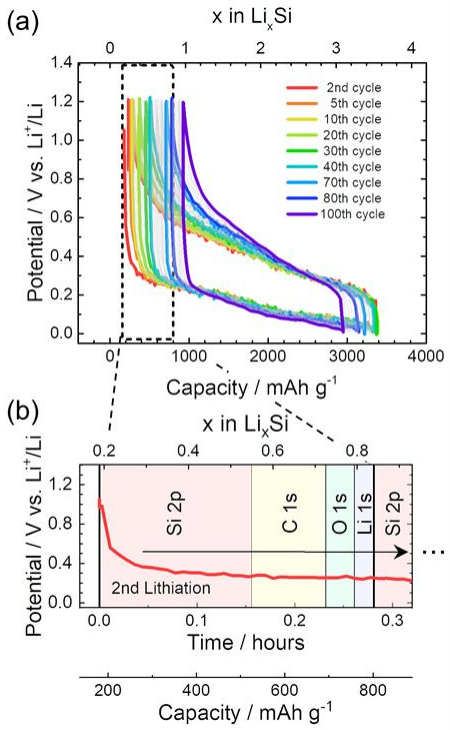

Figure 5 - 2. (a) Galvanostatic lithiation/delithiation potential profiles generated from 2nd to 100th cycle at 0.5 C and cutoff potentials of 1.2–0.01 V *vs.* Li^+/Li. (b) Magnified graph of dashed area shown in (a). Vertical lines indicate time required to acquire XPS spectra.

Figures 5 - 3 (a) and (b) show representative Si 2*p* spectra generated after lithiation/delithiation up to 100 cycles. Peaks corresponding to the reversible Li_xSi and irreversible Li silicates were observed, as described in Chapter 4. The reversible shift of Si 2*p* peak corresponding to Li_xSi becomes smaller with increasing the number of cycles, especially in the initial 30 cycles (Figure 5 - 3 (c)), indicating that the amount of inserted Li decreases. In addition, the peak intensities corresponding to the Li_xSi species in the Si 2*p* (Figures 5 - 3 (a) and (b)) and Li 1*s* (Figure 5 - 3 (d)) regions decreased with increasing the number of cycles.

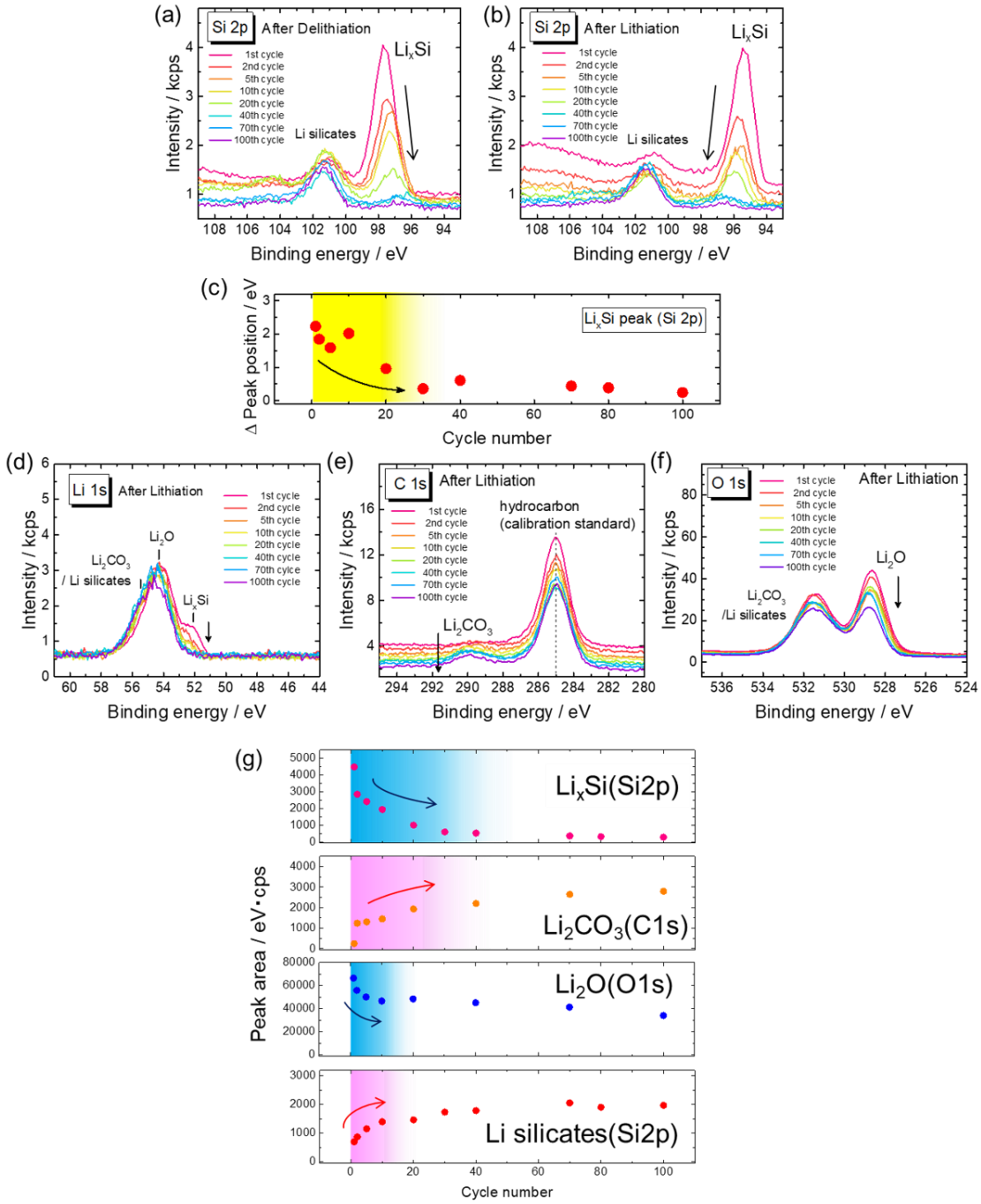

Figure 5 - 3. Representative Si 2*p* spectra generated after (a) delithiation and (b) lithiation up to 100 cycles. (c) Variation in Si-2*p* peak shift corresponding to Li_xSi in each cycle. (d) Li, (e) C, and (f) O 1*s* spectra generated after representative lithiation up to 100 cycles. (g) Variation in photoelectron intensity of Li_xSi (Si 2*p*), Li_2CO_3 (C 1*s*), Li_2O (O 1*s*), and Li-silicates (Si 2*p*) spectra.

Figures 5 - 3 (d)–(f) show representative Li, C, and O 1*s* spectra after lithiation up to 100 cycles. The peak intensities corresponding to Li_xSi, Li_2CO_3, Li_2O, and Li silicates in the Si 2*p*, C 1*s* (at 290 eV), O 1*s* (at 528.5 eV), and Si 2*p* (at 101.0 eV) energy regions during long-term cycling are shown in Figure 5 - 3 (g). The peak intensity of the Li_xSi gradually decreased while that of the Li_2CO_3 increased in approximately the initial 30 cycles. In the initial 10 cycles, the intensity of the Li_2O peak decreased while that of the Li-silicate peak considerably increased. The formation of insulating species such as Li silicates and Li_2CO_3 (the latter by a side reaction between Li_2O and residual CO_2) increases the internal resistance of the Si electrode, resulting in the decrease in the amount of Li insertion. The LLZT, residual gas in an ultrahigh vacuum (UHV) chamber, and hydrocarbon contaminants elsewhere can be oxygen sources. One may consider that such side reactions are irrelevant to the practical ASSBs. In realistic ASSBs, however, residual gas and other impurities are more likely mixed in the system during manufacturing process than those under UHV conditions.

The effect of the phase transition on the long-term cycling performance was discussed by the peak position of the Li_xSi during lithiation/delithiation. In the first 10 lithiation cycles, the peak shifted monotonically (Figure 5 - 4 (a)). In contrast, a drastic change due to the phase transition from crystalline $Li_{15}Si_4$ to amorphous Li_xSi occurred in the region of $x = 2.0–1.6$ up to 10 cycles of delithiation (Figure 5 - 4 (b)).

Figure 5 - 5 shows the variation in the FWHM of the Si $2p_{3/2}$ peaks corresponding to Li_xSi and Li silicates in representative cycles. The FWHM of the Li_xSi peak increased in delithiation (blue and shaded area), suggesting the coexistence of multiple phases in this stage.

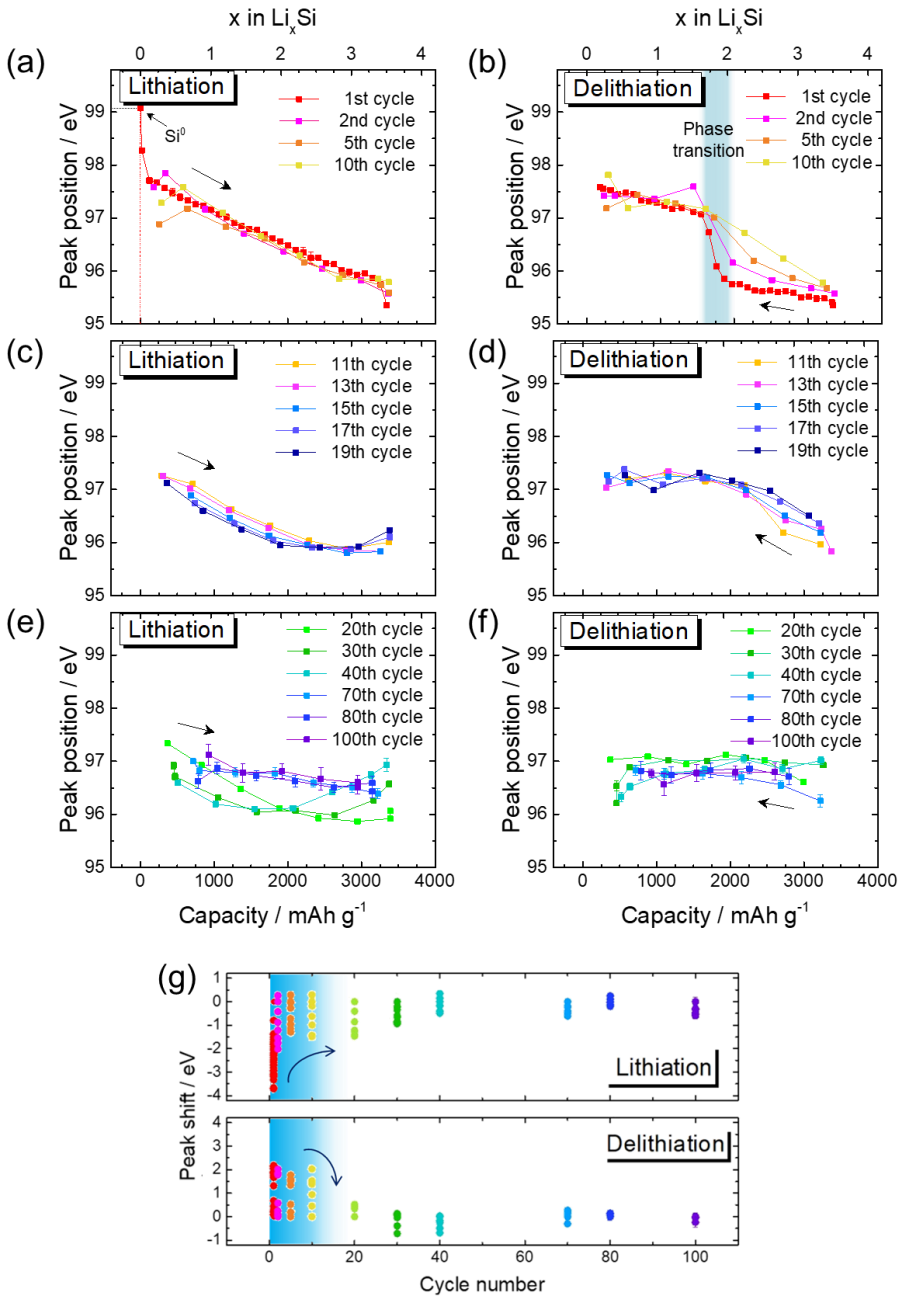

Figure 5 - 4. Variation in position of Si 2*p* peak corresponding to Li_xSi during lithiation/delithiation up to 100 cycles. Lithiation and delithiation from (a, b) 1st to 10th, (c, d) 11th to 19th, and (e, f) 20th to 100th cycle. Blue shaded area in (b) represents composition (Li_xSi; x = 2.0–1.6) where phase transition occurred in the first delithiation. (g) Peak shift during each lithiation/delithiation cycle. Vertical axis represents difference between binding energies obtained from initial peak in each cycle. Error bars representing uncertainty in peak positions were set to ±2σ (where σ are standard deviations extracted from curve fitting.)

After 10 cycles, the peak shift became gradually smaller (Figure 5 - 4 (c) and (d)) and, after 20 cycles, almost no change was observed (Figures 5 – 4 (e) and (f)). In addition, the phase-transition-related FWHM started to decrease, suggesting that the phase transition no longer occurred. Owing to the formation of inactive species such as Li silicates, Li_2O, and Li_2CO_3, overpotential increased significantly, and thus lithium was not inserted until the phase transition from crystalline $Li_{15}Si_4$ in lithiation occurs. In contrast to the FWHM of the Li_xSi peak, that of the Li-silicate one was almost identical in each cycle, confirming that Li silicate is an electrochemically inactive species.

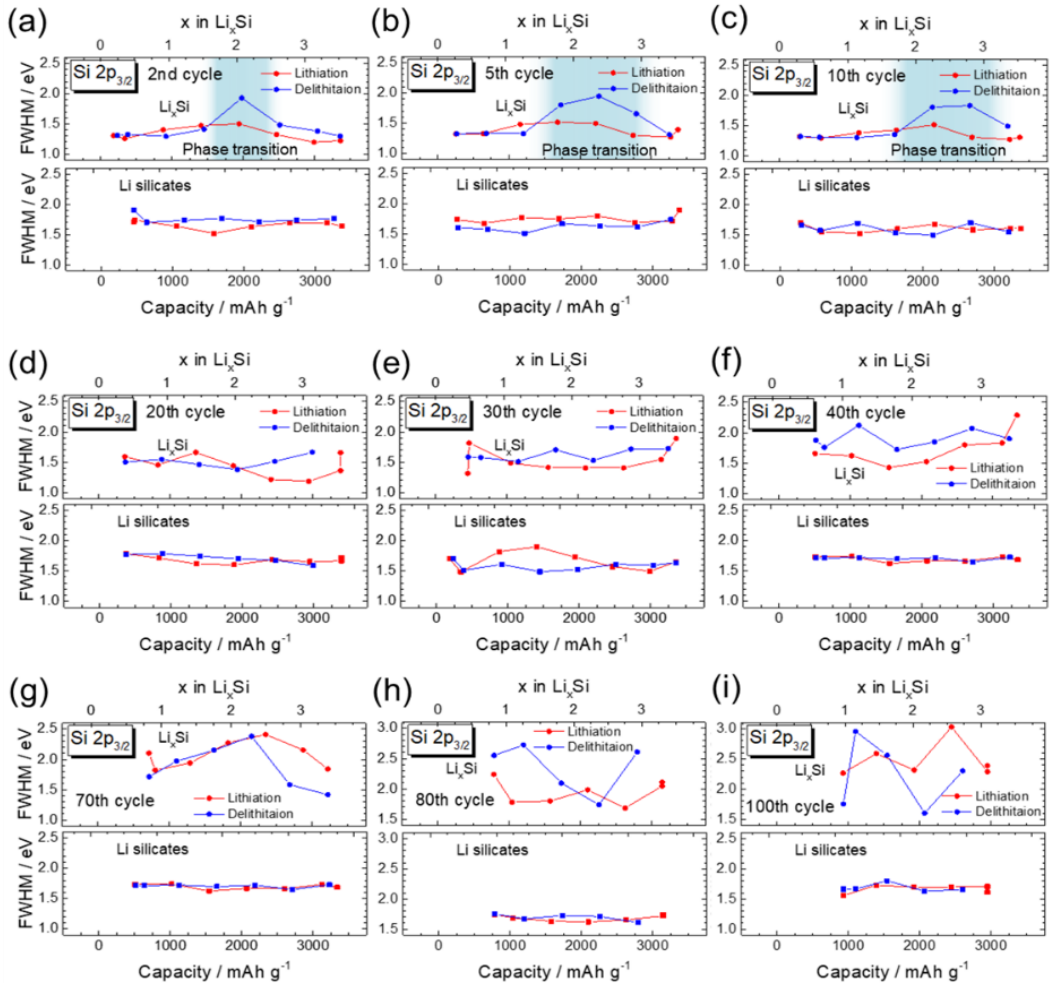

Figure 5 - 5. Evolution of full width at half maximum (FWHM) of Si $2p_{3/2}$ peak corresponding to L_xSi (top column of each graph) and Li silicates (bottom column of each graph) in representative cycles.

5.2.3 Differential capacity curves

The phase transitions and corresponding overpotentials were analyzed using dQ/dV curves. Figures 5 - 6 (a)–(c) show the dQ/dV curves of 1–100 cycles at a cutoff potential of 0.01 V *vs*. Li^+/Li.

The first lithiation dQ/dV curve showed peaks at 0.24 and 0.10 V, both corresponding to the lithiation of amorphous Li_xSi (red curve in Figure 5 - 6 (a) and (c)). The delithiation dQ/dV curve showed broad peaks at 0.29 and 0.49 V corresponding to the delithiation of Li-rich and -poor amorphous Li_xSi,[3, 4] and 0.41 V corresponding to the phase transition of crystalline $Li_{15}Si_4$ to amorphous Li_xSi,[5] respectively (red curve in Figure 5 - 6 (b)).

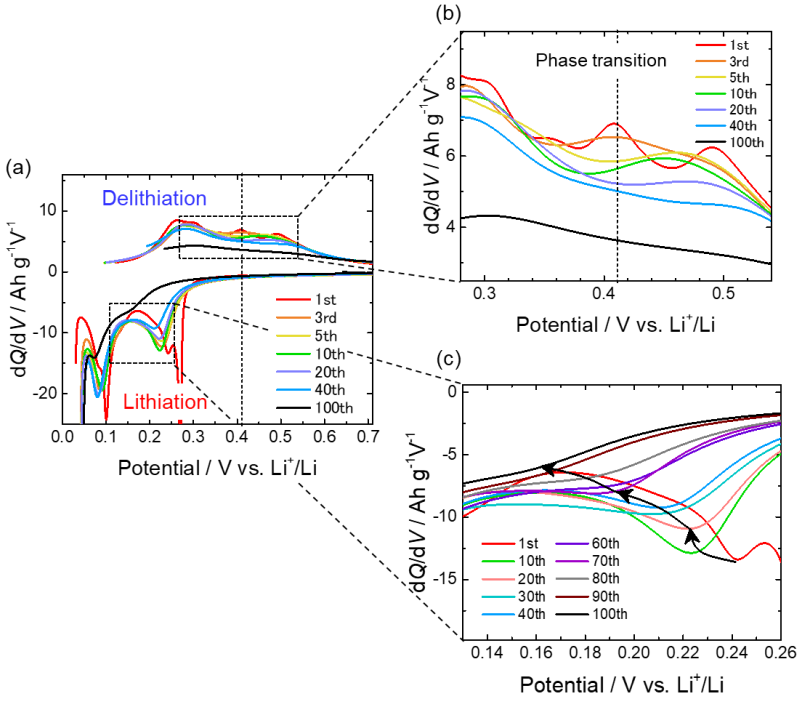

Figure 5 - 6. (a) Differential capacity (dQ/dV) curves generated up to 100th cycle at cutoff potentials of 1.2–0.01 V *vs*. Li^+/Li for Si/LLZT/Li thin-film cells. Magnified graph of dashed box shown in (b) delithiation and (c) lithiation curves. Vertical dashed line represents plateau region corresponding to phase transition from crystalline $Li_{15}Si_4$ to amorphous Li_xSi.

After 10 cycles, the lithiation and delithiation dQ/dV peaks shifted to a more negative and positive potential, which is considered to be due to the increased overpotential.[4, 6-7] In addition, the peak at 0.41 V attributed to the phase transition gradually decreased, and eventually disappeared at approximately 20 cycles (Figure 5 - 6 (b)).

5.2.4 Structural models for deterioration of Si-thin-film electrodes during long-term cycling

Based on the model in Figure 5 - 7, the thickness of the irreversible-species such as Li silicates, Li_2O, and Li_2CO_3 was estimated using the peak-intensity ratio and known physical parameters, following the procedure similar to Chapter 4. The bulk Si was covered with a native suboxide (SiO_y) at the surface of pristine Si electrode. The Li_xSi and Li silicates were formed by the lithiation of the bulk Si and the SiO_y, respectively, and the Li_2O was formed at the outermost layer of the Si electrode. Here, the Li_2CO_3 layer was also incorporated into the model because the small C 1*s* peak corresponding to Li_2CO_3 appeared after the first lithiation, and its intensity gradually increased with repeated cycling (Figure 5 - 8 (a)).

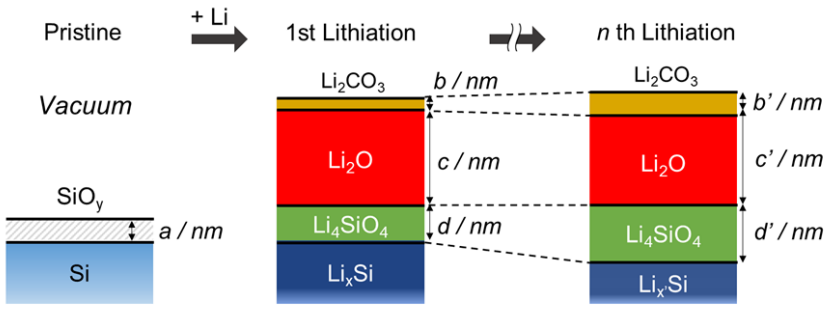

Figure 5 - 7. Structural models of Si electrode lithiated in long-term cycling.

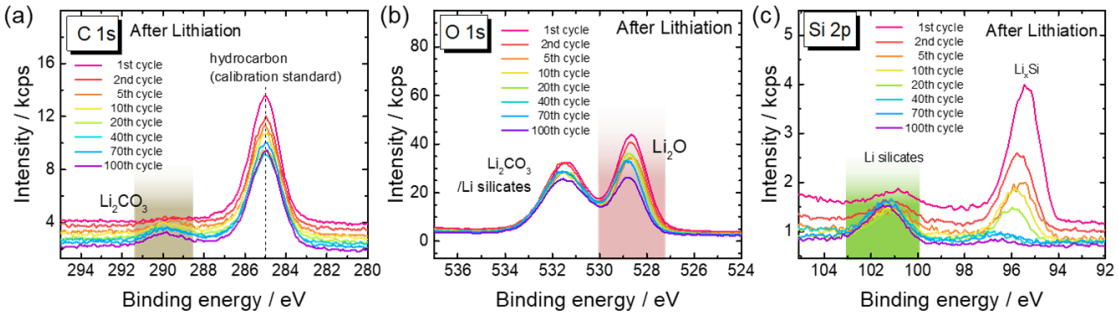

Figure 5 - 8. C 1*s*, O 1*s*, and Si 2*p* spectra generated after representative lithiations up to 100th cycle. Peaks used to estimate thickness of irreversible-species layer as described in text are shaded.

The thickness of the SiO_y layer on the pristine Si electrode, those of the Li_2CO_3, Li_2O, and Li_4SiO_4 layers formed after the first lithiation are denoted as *a*, *b*, *c*, and *d*, respectively (Figure 5 - 7). First, the thicknesses of the (*a*) SiO_y and (*d*) Li_4SiO_4 layers after the first lithiation were estimated using the following equations. (The detailed calculation procedures are described in Chapter 4.)

$$a = \lambda_{SiO_2} \ln\left(\frac{n_{Si}}{n_{SiO_2}}\frac{\lambda_{Si}}{\lambda_{SiO_2}}\frac{I_{SiO_2}}{I_{Si}} + 1\right), \quad (5 - 1)$$

$$d = 1.88a. \quad (5 - 2)$$

The intensities of the C 1*s* peak attributed to Li_2CO_3 $\left(I_{Li_2CO_3,\,C1s}\right)$, the O 1*s* peak attributed to Li_2O $\left(I_{Li_2O,\,O1s}\right)$, and the Si 2*p* peak attributed to Li_4SiO_4 $\left(I_{Li_4SiO_4,\,Si2p}\right)$, and the corresponding peak ratios are represented by the following equations.[8] The corresponding spectra are shown in Figure 5 - 8.

$$I_{Li_2CO_3,\,C1s} = KI_X\sigma_{C1s}n_{Li_2CO_3,\,C}\int_0^d \exp\left(-x/\lambda_{Li_2CO_3,\,C1s}\right)dx$$

$$= KI_X\sigma_{C1s}n_{Li_2CO_3,\,C}\lambda_{Li_2CO_3,\,C1s}\left[1 - \exp\left(-d/\lambda_{Li_2CO_3,C1s}\right)\right]$$

$$I_{Li_2O,\,O1s} = KI_X\sigma_{O1s}n_{Li_2O,\,O}\exp\left(-d/\lambda_{Li_2CO_3,O1s}\right)\int_0^e \exp\left(-x/\lambda_{Li_2O,O1s}\right)dx$$

$$= KI_X\sigma_{O1s}n_{Li_2O,\,O}\lambda_{Li_2O,O1s}\exp\left(-d/\lambda_{Li_2CO_3,O1s}\right)\left[1 - \exp\left(-e/\lambda_{Li_2O,O1s}\right)\right]$$

$$I_{Li_4SiO_4,\,Si2p} = KI_X\sigma_{Si2p}n_{Li_4SiO_4,Si}\exp\left(-e/\lambda_{Li_2O,Si2p}\right)\exp\left(-d/\lambda_{Li_2CO_3,Si2p}\right)$$
$$\int_0^f \exp\left(-x/\lambda_{Li_4SiO_4,Si2p}\right)dx$$
$$= KI_X\sigma_{Si2p}n_{Li_4SiO_4,Si}\lambda_{Li_4SiO_4,Si2p}\exp\left(-e/\lambda_{Li_2O,Si2p}\right)\exp\left(-d/\lambda_{Li_2CO_3,Si2p}\right)$$
$$\left[1-\exp\left(-f/\lambda_{Li_4SiO_4,Si2p}\right)\right]$$

$$\therefore \frac{I_{Li_2CO_3,\,C1s}}{I_{Li_2O,\,O1s}} = \frac{\sigma_{C1s}}{\sigma_{O1s}}\frac{n_{Li_2CO_3,\,C}}{n_{Li_2O,\,O}}\frac{\lambda_{Li_2CO_3,\,C1s}}{\lambda_{Li_2O,O1s}}\frac{\left[1-\exp\left(-d/\lambda_{Li_2CO_3,C1s}\right)\right]}{\exp\left(-d/\lambda_{Li_2CO_3,O1s}\right)\left[1-\exp\left(-e/\lambda_{Li_2O,O1s}\right)\right]}, \quad (5\text{ - }3)$$

$$\therefore \frac{I_{Li_2O,\,O1s}}{I_{Li_4SiO_4,\,Si2p}} = \frac{\sigma_{O1s}}{\sigma_{Si2p}}\frac{n_{Li_2O,\,O}}{n_{Li_4SiO_4,Si}}\frac{\lambda_{Li_2O,O1s}}{\lambda_{Li_4SiO_4,Si2p}}$$
$$\frac{\exp\left(-d/\lambda_{Li_2CO_3,O1s}\right)\left[1-\exp\left(-e/\lambda_{Li_2O,O1s}\right)\right]}{\exp\left(-e/\lambda_{Li_2O,Si2p}\right)\exp\left(-d/\lambda_{Li_2CO_3,Si2p}\right)\left[1-\exp\left(-f/\lambda_{Li_4SiO_4,Si2p}\right)\right]}, \quad (5\text{ - }4)$$

$$\therefore \frac{I_{Li_2CO_3,\,C1s}}{I_{Li_4SiO_4,\,Si2p}} = \frac{\sigma_{C1s}}{\sigma_{Si2p}}\frac{n_{Li_2CO_3,\,C}}{n_{Li_4SiO_4,Si}}\frac{\lambda_{Li_2CO_3,\,C1s}}{\lambda_{Li_4SiO_4,Si2p}}$$
$$\frac{\left[1-\exp\left(-d/\lambda_{Li_2CO_3,C1s}\right)\right]}{\exp\left(-e/\lambda_{Li_2O,Si2p}\right)\exp\left(-d/\lambda_{Li_2CO_3,Si2p}\right)\left[1-\exp\left(-f/\lambda_{Li_4SiO_4,Si2p}\right)\right]}. \quad (5\text{ - }5)$$

From Equations (5 - 1)–(5 - 5), the thicknesses of the SiO_y, Li_2CO_3, Li_2O, and Li_4SiO_4 layers (i.e., *a*, *b*, *c*, and *d*) were estimated to be 0.12, 0.04, 1.77, and 0.23 nm, respectively.

The thickness was also estimated from the 2nd to the 100th cycle. The thickness of the Li_2CO_3, Li_2O, and Li_4SiO_4 layers after the *n*th lithiation was denoted as *b′*, *c′*, and *d′*, respectively. Furthermore, the peak-intensity ratio after the *n*th lithiation can be represented by replacing *b′*, *c′*, and *d′* with *b*, *c*, and *d* in equations (5 - 3)–(5 - 5). As mentioned in Chapter 4, Li_2CO_3 probably forms by the reaction between Li_2O and residual gas molecules (such as CO_2) in the UHV chamber. Thus, the thickness of the Li_2O layer (*c′*) can be obtained using the volumetric ratio of their unit cells, as shown in the following equation.

$$c' = c - \frac{b' - b}{V_{Li_2CO_3}/V_{Li_2O}} = c - \frac{b' - b}{n_{L_2O}/n_{Li_2CO_3}} = c - \frac{b' - b}{2.65}. \quad (5 - 6)$$

Finally, the thickness of the layers formed in each cycle can be determined using Equations (5 - 3)–(5 - 6).

Figure 5 - 9 summarizes the evolution of the estimated thickness when the Li_2O/Li_4SiO_4 interface is defined as zero.

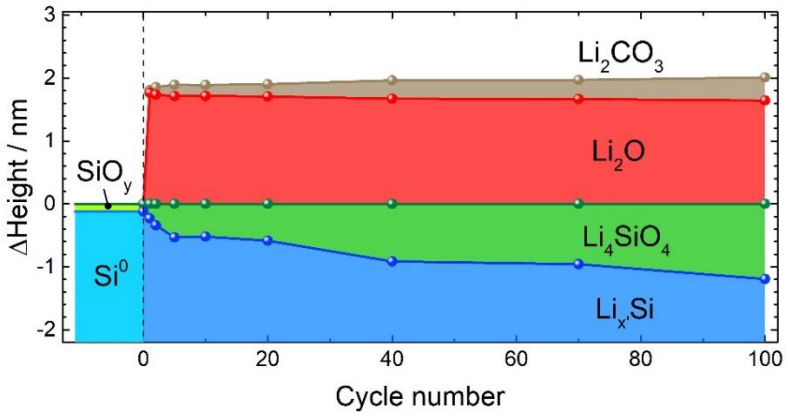

Figure 5 - 9. Evolution of thickness of each layer formed on Si electrode. Height of each layer is expressed as distance from top edge of SiO_y or Li_4SiO_4 layer.

The Li silicates is the measure reason of increased throughout the long-term cycling, implying that the formation of these insulating species increased the cell resistance and overpotential.

It should be noted that this estimation is based on an assumption that a uniform multilayered structure is preserved in long-term cycling. However, the surfaces and interfaces of the layered structure should be roughened owing to the repeated volumetric expansion/contraction and lattice mismatch. Indeed, roughing of the surface and formation of cracks were observed at the Si electrode after 10 cycles by AFM measurements, as discussed in Chapter 4. After the crack formation, Li silicates can form at the freshly exposed Si surfaces, as shown in Figure 5 - 10. Moreover, the

formation of highly resistive species including Li silicates increases the internal cell resistance, resulting in capacity fading in long-term cycling.

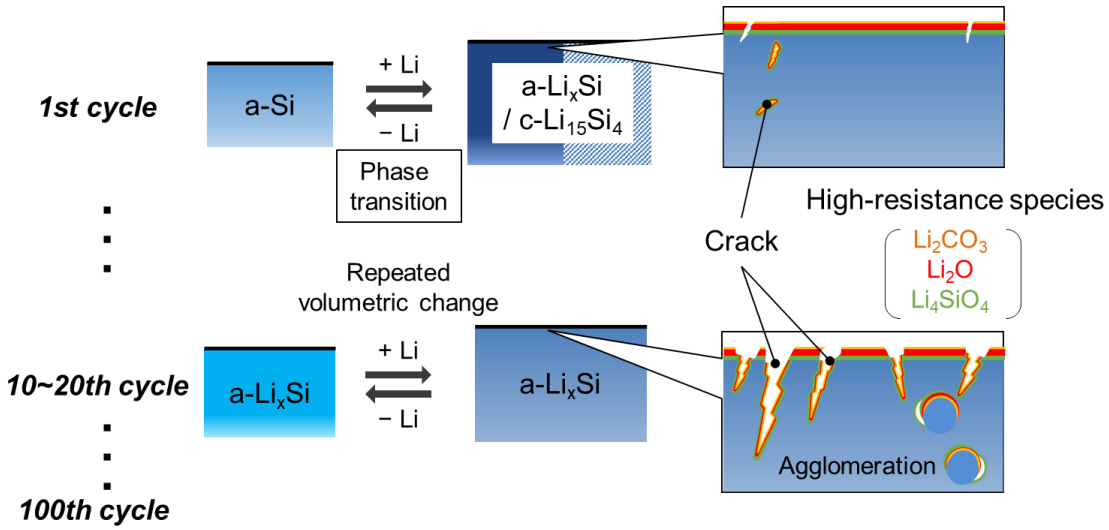

Figure 5 - 10. Proposed model of Si-thin-film anode degradation in long-term cycling.

5.3 Conclusion

As compared to the cutoff potential of 0.09 V *vs*. Li^+/Li, the performance of the Si-thin-film cell showed relatively rapid capacity fading up to the 100th cycle at a cutoff potential of 0.01 V *vs*. Li^+/Li for lithiation, where crystalline $Li_{15}Si_4$ can form, probably due to the occurrence of phase transition.

The phase transition causes a large volumetric change. After the crack formation due to the repetitive volumetric changes, Li silicates were formed at the freshly exposed Si surfaces. The highly resistive Li silicates increased the internal cell resistance, resulting in rapid capacity fading.

Chapter 5

References

1. Rohrer, J.; Albe, K., Insights into Degradation of Si Anodes from First-Principle Calculations. *J. Phys. Chem. C* **2013,** *117* (37), 18796-18803.
2. Rhodes, K.; Dudney, N.; Lara-Curzio, E.; Daniel, C., Understanding the Degradation of Silicon Electrodes for Lithium-Ion Batteries Using Acoustic Emission. *J. Electrochem. Soc.* **2010,** *157* (12), A1354.
3. Obrovac, M. N.; Krause, L. J., Reversible Cycling of Crystalline Silicon Powder. *J. Electrochem. Soc.* **2007,** *154* (2), A103-A108.
4. Chevrier, V. L.; Liu, L.; Le, D. B.; Lund, J.; Molla, B.; Reimer, K.; Krause, L. J.; Jensen, L. D.; Figgemeier, E.; Eberman, K. W., Evaluating Si-Based Materials for Li-Ion Batteries in Commercially Relevant Negative Electrodes. *J. Electrochem. Soc.* **2014,** *161* (5), A783-A791.
5. Hatchard, T. D.; Dahn, J. R., In Situ XRD and Electrochemical Study of the Reaction of Lithium with Amorphous Silicon. *J. Electrochem. Soc.* **2004,** *151* (6), A838.
6. Sakabe, J.; Ohta, N.; Ohnishi, T.; Mitsuishi, K.; Takada, K., Porous amorphous silicon film anodes for high-capacity and stable all-solid-state lithium batteries. *Commun. Chem.* **2018,** *1* (1), 24.
7. Iaboni, D. S. M.; Obrovac, M. N., $Li_{15}Si_4$ Formation in Silicon Thin Film Negative Electrodes. *J. Electrochem. Soc.* **2016,** *163* (2), A255-A261.
8. Strohmeier, B. R., An ESCA method for determining the oxide thickness on aluminum alloys. *Surf. Interface Anal.* **1990,** *15* (1), 51-56.

Chapter 6. Static analysis of lithiation/delithiation of amorphous-SiO_x thin-film electrodes

6.1 Introduction

Silicon monoxide (SiO) has a unique structure, which consists of Si and SiO_2 domains and complex interfacial suboxides.[1] The amorphous SiO-based anode (SiO_x) has been of interest because of the potential for a better cycle performance than pure Si anodes.[2-4] The reason for the high cycle performance of the SiO_x anodes is considered to be due to the damping effect of byproducts such as lithium oxide (Li_2O) and lithium silicates (Li silicates), which can accommodate the notorious volumetric changes of lithium silicide (Li-Si) during lithiation/delithiation.[5-7]

However, the fundamental electrochemical properties of SiO_x anodes have remained unclear. In particular, the formation mechanism of the Li_2O and Li silicates during the lithiation, and the composition and electrochemical reactivity of Li silicates ($Li_2Si_2O_5$, Li_2SiO_3, and Li_4SiO_4) are still under debate although it has been partially investigated by *ex-situ* XPS and TEM analysis.[8-10]

In the present Chapter, the successive lithiation/delithiation reactions of a sputter-deposited SiO_x thin-film electrode on a $Li_{6.6}La_3Zr_{1.6}Ta_{0.4}O_{12}$ (LLZT) solid electrolyte were investigated using *in-situ* electrochemical XPS system. The mechanism of the lithiation/delithiation including side reactions in SiO_x electrodes was discussed from the photoelectron spectra acquired in a stepwise manner as shown in Chapter 4, comparing with the electrochemical features of Si electrodes.

6.2 Results and Discussion

6.2.1 Composition of SiO_x thin-film electrodes

The O content in SiO_x deposited by radio-frequency magnetron sputtering using Ar/O_2 gas mixtures on a Cu plate was confirmed to be 0.8 by electron dispersive x-ray spectroscopy (EDX). This value is the average composition of bulk SiO_x because the probing depth of EDX with several micrometers is sufficiently larger than the thickness of the $SiO_{0.8}$ thin-film electrode (ca.150 nm).

The oxidation states of the $SiO_{0.8}$ surface were characterized by using XPS. As shown in Figure 6 - 1 (a), a broad Si 2*p* peak was observed around 98–105 eV from the $SiO_{0.8}$ electrode, suggesting that Si atoms in $SiO_{0.8}$ have a wide variety of oxidation states, unlike the amorphous Si electrode used in the Chapters 4 and 5 (Figure 6 - 1 (c)). The curve fitting analysis was performed based on an assumption that the Si 2*p* peak is composed of five components with the oxidation number of 0 (Si^0), +1 (Si^{+1}), +2 (Si^{+2}), +3 (Si^{+3}), and +4 (Si^{+4}) with each energy difference of 1 eV.[2, 6, 11] The full widths at half maximum (FWHMs) of the Si $2p_{3/2}$ peak in their components were set to the same value to reduce the number of refinement parameters. On the other hand, the binding energy and the FWHMs of the Si $2p_{3/2}$ peak in the Si^0 component were set as a variable parameter. According to the fitting analysis, ratio of the peak integrations of each component with the oxidation number of 0, +1, +2, +3, and +4 were 0.24, 0.08, 0.13, 0.30, and 0.25, respectively (Figure 6 - 1 (b)).

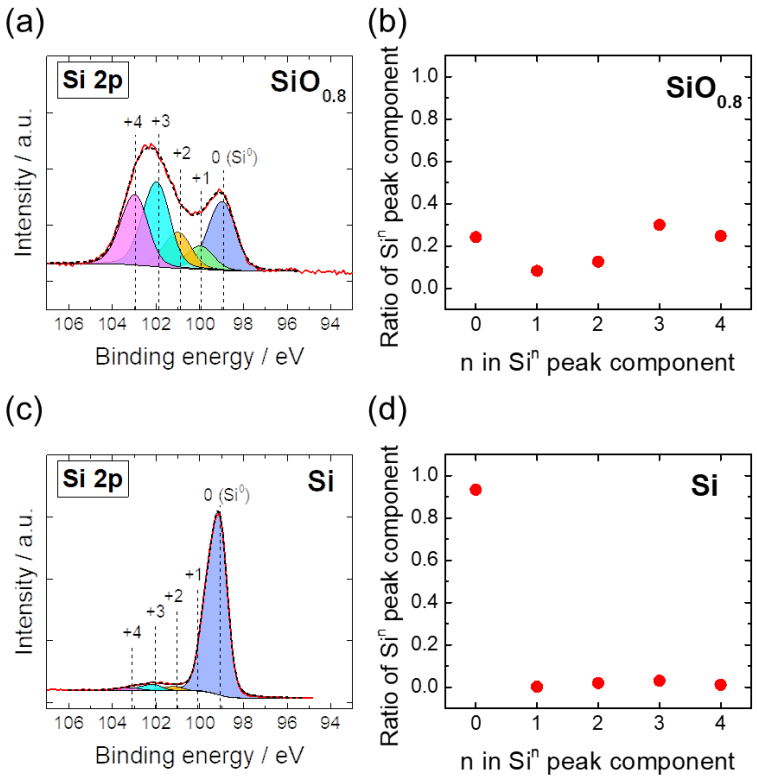

Figure 6 - 1. Si 2*p* spectra of the (a) $SiO_{0.8}$ and (c) Si electrodes. Si 2*p* peaks are deconvoluted into five components with the oxidation number of 0, +1, +2, +3, and +4. The ratio of each peak component in the (b) $SiO_{0.8}$ and (d) Si electrodes.

6.2.2 Galvanostatic potential profiles

The electrochemical lithiation/delithiation of the $SiO_{0.8}$/LLZT/Li thin-film cell were performed in the analysis chamber of the XPS apparatus under UHV conditions (2×10^{-9} Torr). Figure 6 - 2 (a) shows the first and second galvanostatic lithiation/delithiation potential profiles obtained at current density per unit area of 4.65 μA/cm^2, which was identical to that value for Si electrodes in Chapter 4 for a comparison. The charge integrations for the first lithiation (from A to B) and delithiation (from B to C) processes were 1,421 and 841 mAh g^{-1}, respectively. Therefore, a large capacity loss, 580 mAh g^{-1}, and low coulombic efficiency, 59.2%, were observed in the first cycle for the $SiO_{0.8}$ electrode. Comparing with of the pure Si thin-film electrode (~3,340 mAh g^{-1}, See

Chapter 4), the specific capacity of the $SiO_{0.8}$ thin-film electrode was less than half. Such relatively low initial coulombic efficiency and specific capacity for $SiO_{0.8}$ are consistent with the previous reports on SiO_x electrodes in both all-solid-state and liquid-type cells.[2-3]

In the second cycle, the coulombic efficiency was improved to 95% while the specific capacity remained identical, possibly owing to the increased conductivity by Li insertion in the first lithiation (Figure 6 - 2 (b)).

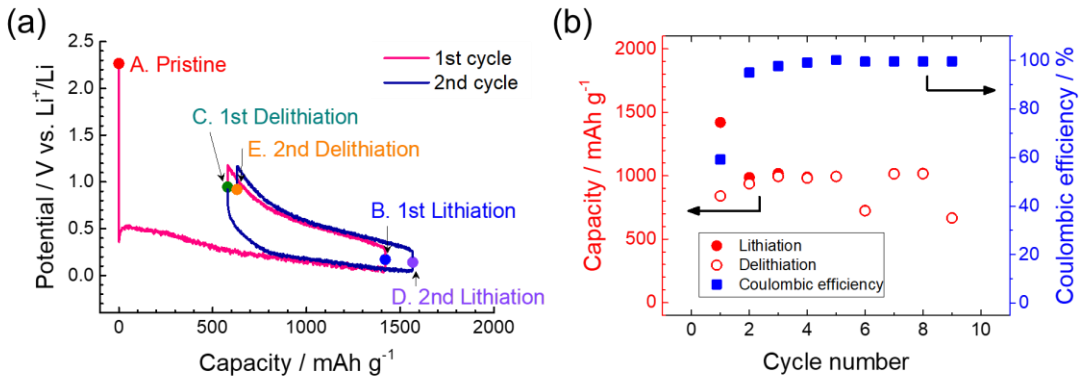

Figure 6 - 2. (a) Galvanostatic lithiation/delithiation potential profiles and (b) cycle performance obtained for $SiO_{0.8}$/LLZT/Li cell cycled at the current of 4.65 μA/cm² and cutoff potential in range 0.01–1.2 V *vs.* Li^+/Li. Specific capacity was normalized by mass of deposited Si atoms under the sputtering condition using Ar gas. XPS measurements were performed at each state denoted by A–E.

6.2.3 Static observation of electrochemical lithiation of SiO_x anode at various states of charge

6.2.3.1 XPS analysis using Al Kα incident x-rays

Figure 6 - 3 (a) shows the Li 1*s*, Si 2*p*, and O 1*s* spectra at each state of A–E in Figure 6 - 2 (a). A small Li 1*s* peak corresponding to lithium carbonates (Li_2CO_3) was observed at 55.4 eV from the pristine $SiO_{0.8}$ electrode (Figure 6 - 3 (a) A), possibly due to the intrusion of Li during the thermal deposition process for the Li metal layer. In addition,

broad Si 2*p* and O 1*s* peaks corresponding to Si suboxides (SiO_y) were obtained around 98–105 eV and 530–534 eV, respectively.

In the Si 2*p* region, a Si 2*p* peak corresponding to Li-Si appeared at 96.4 eV after the first lithiation (Figure 6 - 3 (a) B). It highly shifted to the binding energy to 97.1 eV after the subsequent delithiation (Figure 6 - 3 (a) C). This indicates that reversible lithiation/delithiation reactions of the Li-Si phase take place in SiO_x electrodes, as is the case of Si electrode shown in Chapter 4.

In the Li 1*s* energy region, peaks corresponding to Li_2O (at 54.0 eV) and Li_2CO_3/Li silicates (at 55.4 eV) were increased after the first lithiation. The Li_2O and Li_2CO_3 were formed possibly as a result of the reaction of inserted Li with SiO_y as well as residual gas in UHV chamber.

Figure 6 - 3 (a) D–E show the spectra after the second lithiation/delithiation processes. In contrast to the first cycle, the broad Si 2*p* peak around 98–105 eV corresponding to SiO_x, except for Li-orthosilicate (Li_4SiO_4) peak at 101.0 eV,[5, 12] was significantly decreased, while the Li-Si (at 96.4 eV) and Li_2O peaks (at 54.0 and 528.8 eV) were increased in the second cycle. This change implies that SiO_y was reduced by inserted Li to form Li_2O and Li-Si because of very high reactivity of Li.

On the basis of the XPS results, the second lithiation/delithiation cycle can be described as follows. At state C after the first delithiation, the SiO_y and Li silicates are present. The SiO_y are reduced to Si species to form active Li-Si, while a part of inserted Li (Li-Si) is oxidized to form Li_2O as inactive species. As Li permeates the $SiO_{0.8}$ electrode, Li_2O are formed throughout the electrode. It is expected that Li_2O and Li_4SiO_4 act as dampers to suppress the stress induced by Li-Si volumetric changes, leading to improve the cycle performance.[3, 5, 7, 13] In particular, the lithiated Si electrode

containing Li_2O- and Li_4SiO_4-surface layers has more ductile at least than Si, as confirmed by nanomechanical measurement using *in-situ* AFM in Chapter 4 (Figure 4 – 20 (d)), implying the applicability of Li_2O and Li_4SiO_4 as dampers.

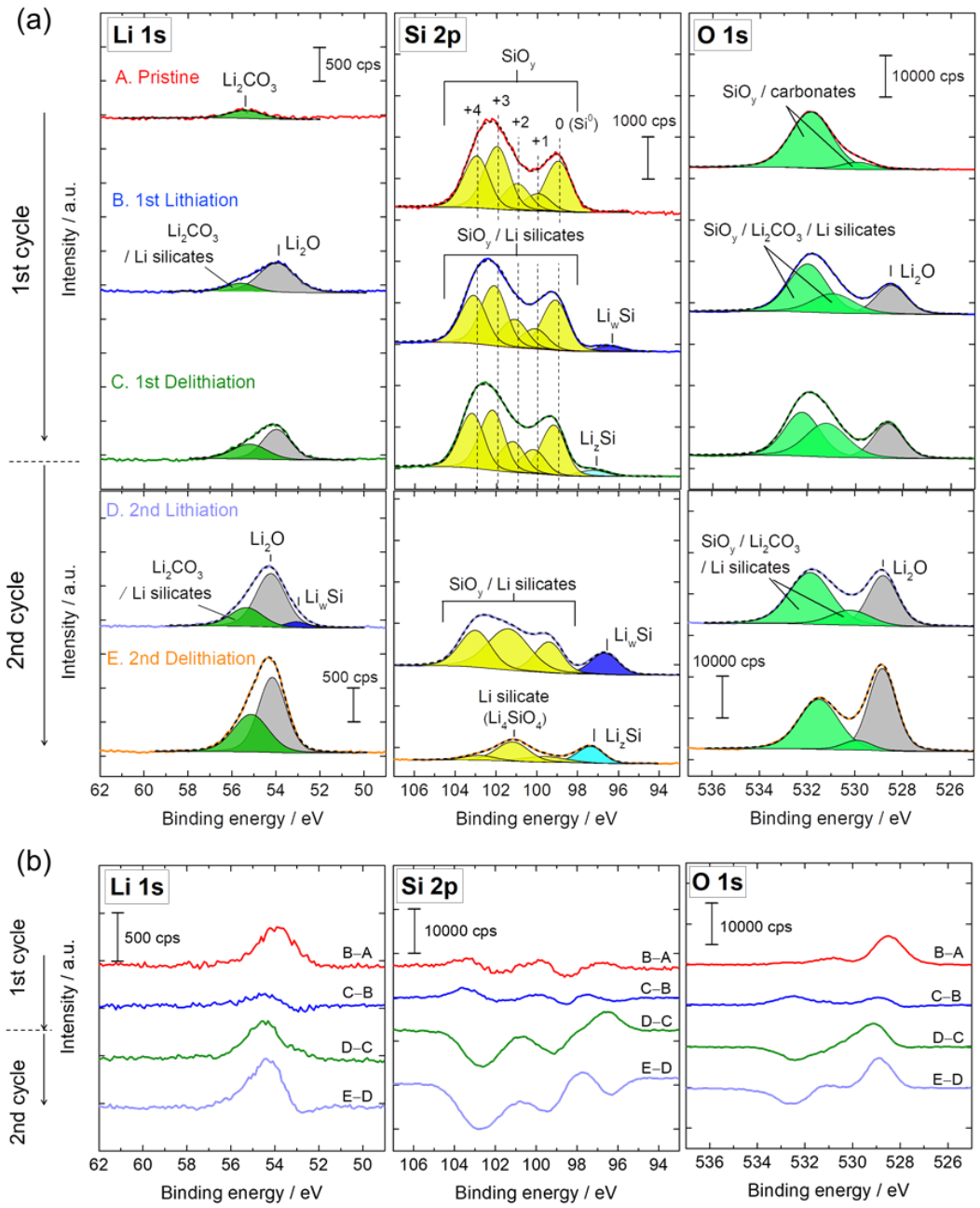

Figure 6 - 3. (a) Li 1*s*, Si 2*p*, and O 1*s* spectra of the $SiO_{0.8}$ electrode at the states A–E in Figure 6 - 2: (A) pristine electrode, after the first (B) lithiation and (C) delithiation, second (D) lithiation and (E) delithiation. All spectra were obtained by using Al Kα incident x-rays. (b) Difference spectra at each state.

6.2.3.2 Depth-resolved analysis using Ag Lα incident x-rays

A depth-resolved analysis was carried out by using a Ag Lα x-ray source whose photon energy ($h\nu$=2,984 eV) is higher than that of Al Kα x-rays ($h\nu$=1,487 eV). Figures 6 - 4 (a) and (b) show the O 1*s* and Si 2*p* spectra acquired by using Ag Lα x-rays after the second lithiation/delithiation reactions of the $SiO_{0.8}$ electrode, respectively. In both cases using Al Kα and Ag Lα x-rays, the peak area of O 1*s* corresponding to Li_2O at 528.8 eV increased, and that of Si 2*p* corresponding to SiO_y/Li silicates at 98–105 eV significantly decreased after the second delithiation. This indicates that the Li_2O formation and SiO_y reduction occur not only at the surface but also in the bulk (Figures 6 - 4 (a) and (b)).

As shown in Chapter 4, the ratio of the SiO_y/Li silicates peak of the Si electrode was significantly decreased by using Ag Lα source because the SiO_y and Li silicates were localized on the Si-electrode surface (grey points in Figure 6 - 4 (c)). In contrast, that of the $SiO_{0.8}$ electrode was almost identical to each other (red and blue plots in Figure 6 - 4 (c)). Such well-distributed oxygen species in SiO_x electrodes are considered to relieve the stress induced by the Li-Si volumetric changes and to improve the cycle performance.

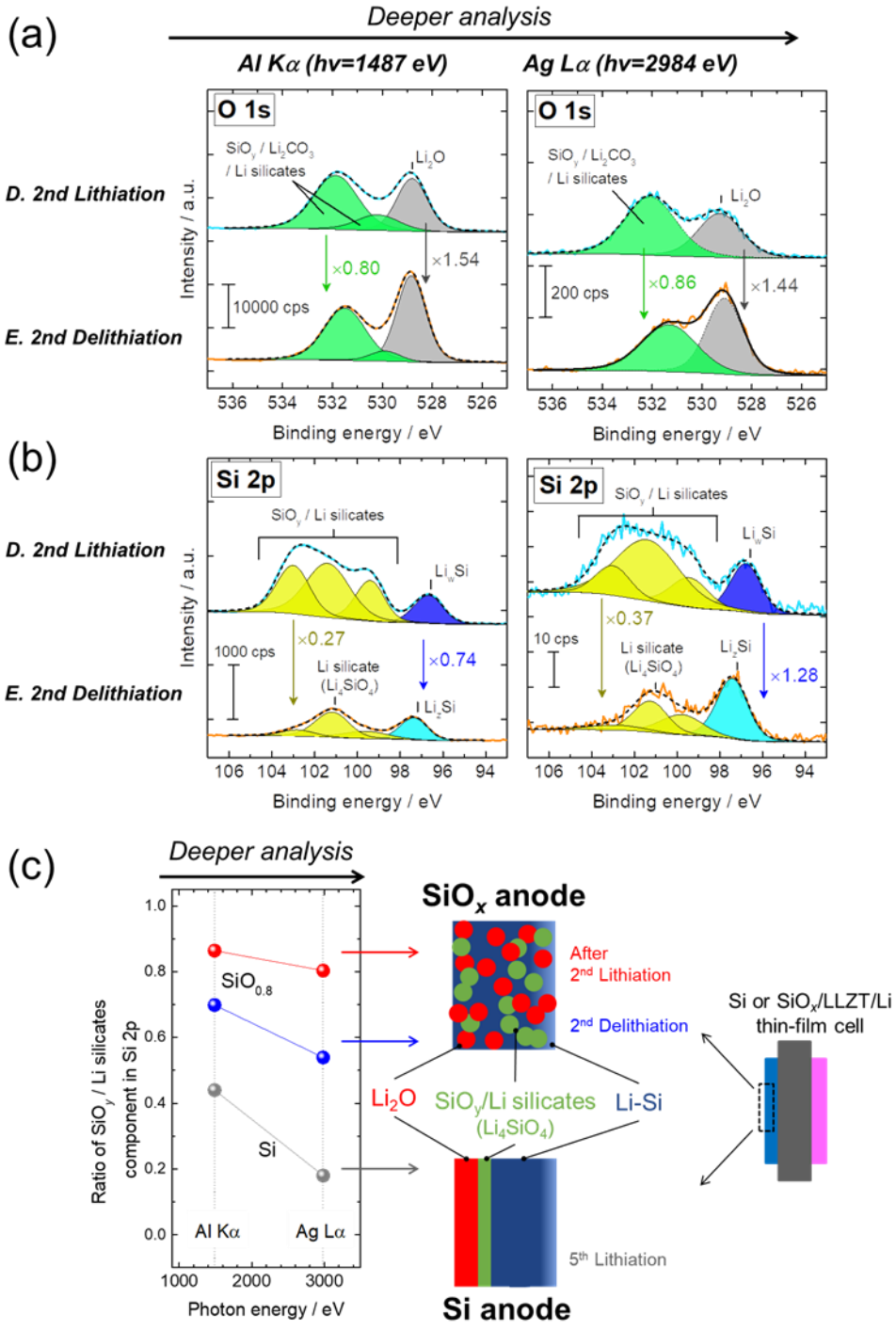

Figure 6 - 4. (a) O 1*s* and (b) Si 2*p* spectra of the $SiO_{0.8}$ electrode after the second lithiation and delithiation when using Al Kα (*hν*=1,487 eV) and Ag Lα (*hν*=2,984 eV) incident x-rays. (c) The ratio of SiO_y/Li silicates component in Si 2*p* spectra of the $SiO_{0.8}$ electrode, and that of reference Si electrode used in Chapters 4 and 5. Schematic illustration shows a distribution of Li_2O, SiO_y/Li silicates, and Li-Si in Si and SiO_x thin-film electrodes.

6.3 Conclusions

The lithiation/delithiation reactions of the $SiO_{0.8}$ thin-film electrode were stepwisely investigated using *in-situ* XPS system. The quasi-reversible shift of the Si 2*p* peak corresponding to lithium silicide (Li-Si) was observed, as similar to Si electrodes. In addition, the large capacity loss occurred in the first lithiation/delithiation cycle due to the formation of irreversible species such as Li_2O, Li silicates, and Li_2CO_3. The Li-Si and Li_2O were formed by the reduction of Si suboxides and oxidation of inserted Li, respectively. The Li_2O and Li silicates in SiO_x thin-film electrodes are considered to act as dampers accommodating Li-Si volumetric changes and improve the cycle performance.

References

1. Hirata, A.; Kohara, S.; Asada, T.; Arao, M.; Yogi, C.; Imai, H.; Tan, Y.; Fujita, T.; Chen, M., Atomic-scale disproportionation in amorphous silicon monoxide. *Nat. Commun.* **2016,** *7* (1), 11591.
2. Miyazaki, R.; Ohta, N.; Ohnishi, T.; Takada, K., Anode properties of silicon-rich amorphous silicon suboxide films in all-solid-state lithium batteries. *J. Power Sources* **2016,** *329*, 41-49.
3. Haruta, M.; Doi, T.; Inaba, M., Oxygen-Content Dependence of Cycle Performance and Morphology Changes in Amorphous-SiO_x Thin-Film Negative Electrodes for Lithium-Ion Batteries. *J. Electrochem. Soc.* **2019,** *166* (2), A258-A263.
4. Pan, K.; Zou, F.; Canova, M.; Zhu, Y.; Kim, J.-H., Systematic electrochemical characterizations of Si and SiO anodes for high-capacity Li-Ion batteries. *J. Power Sources* **2019,** *413*, 20-28.
5. Miyachi, M.; Yamamoto, H.; Kawai, H.; Ohta, T.; Shirakata, M., Analysis of SiO Anodes for Lithium-Ion Batteries. *J. Electrochem. Soc.* **2005,** *152* (10), A2089-A2091.
6. Nguyen, C. C.; Choi, H.; Song, S. W., Roles of Oxygen and Interfacial Stabilization in Enhancing the Cycling Ability of Silicon Oxide Anodes for Rechargeable Lithium Batteries. *J. Electrochem. Soc.* **2013,** *160* (6), A906-A914.
7. Wang, J.; Zhao, H.; He, J.; Wang, C.; Wang, J., Nano-sized SiO_x/C composite anode for lithium ion batteries. *J. Power Sources* **2011,** *196* (10), 4811-4815.
8. Guo, B.; Shu, J.; Wang, Z.; Yang, H.; Shi, L.; Liu, Y.; Chen, L., Electrochemical reduction of

nano-SiO_2 in hard carbon as anode material for lithium ion batteries. *Electrochem. Commun.* **2008,** *10* (12), 1876-1878.

9. Sun, Q.; Zhang, B.; Fu, Z.-W., Lithium electrochemistry of SiO_2 thin film electrode for lithium-ion batteries. *Appl. Surf. Sci.* **2008,** *254* (13), 3774-3779.
10. Yu, B. C.; Hwa, Y.; Park, C. M.; Sohn, H. J., Reaction mechanism and enhancement of cyclability of SiO anodes by surface etching with NaOH for Li-ion batteries. *J. Mater. Chem. A* **2013,** *1* (15), 4820-4825.
11. Bell, F. G.; Ley, L., Photoemission study of SiO_x ($0 \leq x \leq 2$) alloys. *Physical Review B* **1988,** *37* (14), 8383-8393.
12. Philippe, B.; Dedryvère, R.; Allouche, J.; Lindgren, F.; Gorgoi, M.; Rensmo, H.; Gonbeau, D.; Edström, K., Nanosilicon Electrodes for Lithium-Ion Batteries: Interfacial Mechanisms Studied by Hard and Soft X-ray Photoelectron Spectroscopy. *Chem. Mater.* **2012,** *24* (6), 1107-1115.
13. Veluchamy, A.; Doh, C.-H.; Kim, D.-H.; Lee, J.-H.; Lee, D.-J.; Ha, K.-H.; Shin, H.-M.; Jin, B.-S.; Kim, H.-S.; Moon, S.-I.; Park, C.-W., Improvement of cycle behaviour of SiO/C anode composite by thermochemically generated Li_4SiO_4 inert phase for lithium batteries. *J. Power Sources* **2009,** *188* (2), 574-577.

Chapter 7. General conclusion and future research prospects

7.1 General conclusion

In this study, the lithiation/delithiation of amorphous Si and SiO_x thin-film anodes deposited on solid electrolytes were investigated mainly using *in-situ* XPS and electrochemical analysis for application to high-performance ASSB anode materials.

In Chapter 2, the method of preparing the thin-film cells and the analytical approaches were described, and the principles and setup of the characterization techniques were presented.

In Chapter 3, quantitative and depth analyses were described wherein XPS was used to observe liquid samples encapsulated in an environmental cell fabricated using a thin film as a separator between the vacuum and the cell interior.

In Chapter 4, the initial stage of lithiation/delithiation of the Si-thin-film anode was investigated using static analysis to elucidate the reaction mechanism including the side reactions, phase transitions, and volumetric changes depending on the Li content (i.e., state of charge). After the first lithiation, irreversible species such as L_2O, Li_2CO_3, and lithium silicates (Li silicates) formed in addition to irreversible lithium silicide (Li_xSi). According to the quantitative analysis conducted using charge densities and XPS, 25% of the Li was consumed in the formation of such irreversible species. The quasi-reversible lithiation/delithiation of Li_xSi was evidenced by analyzing the binding energy of the Si 2*p* peak. Although the Li_xSi peak monotonically shifted to a higher binding energy with increasing Li content, the Li_xSi peak shifted drastically at the apparent composition of

$Li_{2.0–1.6}Si$ in delithiation. The peak shift was attributed to the amorphization of the crystalline $Li_{15}Si_4$ formed in the immediately preceding lithiation. Crystalline $Li_{15}Si_4$ transformed into amorphous Li_xSi (x = 2.0–1.6) in delithiation, and the transformation was accompanied by a considerable change in chemical state.

In Chapter 5, the electrochemical lithiation/delithiation of the amorphous-Si thin-film electrode was tracked using *in-situ* XPS and differential capacity (dQ/dV) analysis for up to 100 cycles to elucidate the cause of the capacity fading. During the initial ten cycles, the Li-silicate formation increased and then the phase transition from crystalline $Li_{15}Si_4$ to amorphous Li_xSi no longer occurred in delithiation. After 20 cycles, the cell resistance had increased owing to the increased formation of insulating species such as Li silicates and Li_2CO_3, and the amount of Li insertion into Li_xSi gradually decreased.

In Chapter 6, the lithiation/delithiation of the amorphous-SiO_x thin-film anode were investigated using *in-situ* XPS. After the first lithiation, reversible Li_xSi formed as it had with the Si anode. In addition, Li_2O and Li_2CO_3 formed owing to side reactions between SiO_x, Li, Li silicates, and residual CO_2. The Li_2O (which formed by SiO_x reduction and Li oxidation) and Li silicates both are considered to improve the cycle performance owing to their damping effect for accommodating Li_xSi volumetric changes.

The mechanism of the lithiation/delithiation-related reactions was proposed toward the practical application of Si-based anodes to ASSBs.

7.2 Future research prospects

Toward improving performance of Si-based anodes

Based on the foregoing conclusions, the following guidelines are proposed for overcoming the two major challenges of Si-based anodes, i.e., the low initial coulombic

efficiency and rapid capacity fading in long-term cycling.

(1) *To improve initial coulombic efficiency*

The Si suboxides at the Si-anode surface lead to irreversible capacity loss due to the formation of Li silicates in the first lithiation. One approach to improve the initial coulombic efficiency is to inhibit the formation of Si suboxides by applying surface modifications such as hydrogenation termination,[1-2] methyl termination,[3] and hydrosilation.[4]

The surfaces of hydrogen-terminated Si are reasonably oxidation resistant in air.[5] However, the Si–H bonds in the hydrogen-terminated Si reportedly react with conventional liquid electrolytes containing ethylene carbonate and ethyl methyl carbonate,[6-7] resulting in a high lithiation overpotential due to the formation of inhomogeneous and unstable SEIs. Such side reactions are supposed to occur less frequently in ASSBs owing to the high chemical stability of solid electrolytes.

(2) *To suppress rapid capacity fading*

Well-dispersed oxygen, as in SiO_x thin-film anodes, can improve the cycle performance owing to the damping effects of side-reaction products including Li_2O for accommodating the notorious Si volumetric changes during lithiation/delithiation. Therefore, controlling the number and distribution of oxygen species is quite important for improving the cycle performance of Si-based anodes. The proposed reaction mechanism to form Li_2O and Li_xSi from SiO_x, as described in Chapter 6, provides physical parameters for estimating the volumetric change ratio and the associated stress in SiO_x anodes. On the basis of model calculations using the parameters, new Si-based anodes should be designed with oxygen and irreversible phases to improve the cycle performance.

Furthermore, it was demonstrated that the cycle performance of Si anodes could be

improved by lithiation/delithiation at compositions below the threshold for required for forming crystalline $Li_{15}Si_4$ (see Chapter 5).

In-situ electrochemical XPS

The developed *in-situ* electrochemical XPS system is suitable for highly reactive battery materials because it enables us to perform chemical analysis under operating conditions without disassembling batteries. In addition to the analysis of anode materials in thin-film cells, *in-situ* XPS should promote the analysis of chemical reactions[8] and nanoionics phenomena[9-10] at electrode/solid-electrolyte interfaces, which are the major bottleneck impeding the development of ASSBs.[11]

However, knowledge of characterizing batteries under vacuum remains insufficient, probably because most battery materials have been conventionally characterized in an Ar-filled glove box. This lack of knowledge has hampered the integration of battery characterization with powerful measurement techniques performed under vacuum.

For example, although we confirmed that the AC impedance measurements in a vacuum chamber have a higher noise level than in an Ar atmosphere, the cause of the noise remains unclear. In addition, the thin-film cell fabricated with a Si/LLZT/Li structure shows more reversible lithiation/delithiation potential profiles under vacuum than under Ar (see Chapter 4). It is inferred that the adhesion at the Si/LLZT and/or Li/LLZT interfaces greatly impacts the cycle performance. Clarification of this mechanism will lead to improved stability of Si-based anodes for application to ASSBs.

Furthermore, it is expected that the elucidation of battery performance under vacuum will accelerate research on *in-situ* observation techniques that promote the development of various battery materials in addition to the fundamental research on Si-based anodes.

Chapter 7

References

1. Chabal, Y. J.; Higashi, G. S.; Raghavachari, K.; Burrows, V. A., Infrared spectroscopy of Si(111) and Si(100) surfaces after HF treatment: Hydrogen termination and surface morphology. *J. Vac. Sci. Technol. A* **1989,** *7* (3), 2104-2109.
2. Higashi, G. S.; Chabal, Y. J.; Trucks, G. W.; Raghavachari, K., Ideal hydrogen termination of the Si (111) surface. *Appl. Phys. Lett.* **1990,** *56* (7), 656-658.
3. Fidélis, A.; Ozanam, F.; Chazalviel, J. N., Fully methylated, atomically flat (111) silicon surface. *Surf. Sci.* **2000,** *444* (1), L7-L10.
4. Zazzera, L. A.; Evans, J. F.; Deruelle, M.; Tirrell, M.; Kessel, C. R.; McKeown, P., Bonding Organic Molecules to Hydrogen‐Terminated Silicon Wafers. *J. Electrochem. Soc.* **1997,** *144* (6), 2184-2189.
5. Wayner, D. D. M.; Wolkow, R. A., Organic modification of hydrogen terminated silicon surfaces. *J. Chem. Soc., Perkin Trans. 2* **2002,** (1), 23-34.
6. Pekarek, R. T.; Affolter, A.; Baranowski, L. L.; Coyle, J.; Hou, T.; Sivonxay, E.; Smith, B. A.; McAuliffe, R. D.; Persson, K. A.; Key, B.; Apblett, C.; Veith, G. M.; Neale, N. R., Intrinsic chemical reactivity of solid-electrolyte interphase components in silicon–lithium alloy anode batteries probed by FTIR spectroscopy. *J. Mater. Chem. A* **2020,** *8* (16), 7897-7906.
7. Schnabel, M.; Arca, E.; Ha, Y.; Stetson, C.; Teeter, G.; Han, S.-D.; Stradins, P., Enhanced Interfacial Stability of Si Anodes for Li-Ion Batteries via Surface SiO_2 Coating. *ACS Appl. Energy Mater.* **2020,** *3* (9), 8842-8849.
8. Sakuda, A.; Hayashi, A.; Tatsumisago, M., Interfacial Observation between $LiCoO_2$ Electrode and Li_2S−P_2S_5 Solid Electrolytes of All-Solid-State Lithium Secondary Batteries Using Transmission Electron Microscopy. *Chem. Mater.* **2010,** *22* (3), 949-956.
9. Ohta, N.; Takada, K.; Zhang, L.; Ma, R.; Osada, M.; Sasaki, T., Enhancement of the High-Rate Capability of Solid-State Lithium Batteries by Nanoscale Interfacial Modification. *Adv. Mater.* **2006,** *18* (17), 2226-2229.
10. Takada, K.; Ohno, T.; Ohta, N.; Ohnishi, T.; Tanaka, Y., Positive and Negative Aspects of Interfaces in Solid-State Batteries. *ACS Energy Lett.* **2018,** *3* (1), 98-103.
11. Luntz, A. C.; Voss, J.; Reuter, K., Interfacial Challenges in Solid-State Li Ion Batteries. *J. Phys. Chem. Lett.* **2015,** *6* (22), 4599-4604.

Acknowledgements

本論文は、北海道大学大学院総合化学院 博士後期課程在籍中、増田卓也教授のもとで行った研究内容により構成されています。増田卓也教授には本論文作成の御指導はもとより、実験や研究の指針、データの解釈、進捗報告会や学会でのプレゼンテーション、投稿論文の執筆に至るまで、常に的確な御指導を賜りました。また、研究以外の私生活においても多大なる御支援および御配慮頂きましたことを、心より御礼申し上げます。

御多用の中、主査として本論文を審査して頂き、貴重なご助言を賜りました村越敬教授に心より御礼申し上げます。同じく副査として審査して頂きました幅崎浩樹教授、白幡直人教授、吉尾正史教授には、論文作成にあたり詳しくご検討いただき、貴重なご意見を賜りましたこと、心より御礼申し上げます。

シリコン（Si）薄膜電池試料の特性評価を行うにあたって共同研究を快く引き受けてくださり、試料作製・評価および投稿論文について貴重な御指導・御助言を賜りました、物質・材料研究機構 エネルギー・環境材料研究拠点の大西剛博士、高田和典博士に深く感謝申し上げます。

シリコン酸化物（SiO_x）薄膜電池試料の特性評価を行うにあたり、試料をご提供頂き、貴重な御意見を賜りました、同志社大学 理工学部の土井貴之教授、近畿大学 産業理工学部の春田正和准教授に深く感謝申し上げます。

電池試料の分析評価のため、NIMS 蓄電池基盤プラットフォームの機器を使用させて頂くにあたり、丁寧な技術的な御指導を賜りました、支援スタッフの方々に御礼申し上げます。

最後に、今日に至るまでの長い間、円滑に研究を行うことができるよう支援してくださり、いつも温かく見守ってくださった両親に対して、心より深く謝意を表します。

２０２１年3月　遠藤 頼夢